

Biomimetic Anti-Cancer Nanosystem: CRISPR-Engineered Hypertumors with Dual-Responsive Release for Targeted Tumor Vascular Disruption

Abdelmoumen Shad Serroune^{1,2,3}, Emilie Cassier^{1,2}, Hitomi Azikiwa^{1,3}, Marc Plantet^{1,2}, Harold Ron Dwight^{1,3}

¹ NANOGEIOS iPONG Lab (Integrative Proteogenomics, Oncology, Nanotech, Genetics), Department of Nanotech Genetic Engineering, NANOGEIOS Laboratory, Seoul, South Korea

² NANOGEIOS iPONG Lab (Integrative Proteogenomics, Oncology, Nanotech, Genetics), Department of Nanotech Genetic Engineering, NANOGEIOS Laboratory, Incheon, South Korea

³ NANOGEIOS iPONG Lab (Integrative Proteogenomics, Oncology, Nanotech, Genetics), Department of Nanotech Genetic Engineering, NANOGEIOS Laboratory, Tokyo, Japan

Abstract

We present a novel therapeutic paradigm for cancer treatment that synergistically integrates CRISPR-Cas9 genetic engineering with dual-responsive nanotechnology. Inspired by Peto's Paradox, we developed "hypertumors" - patient-derived cancer cells genetically modified to be non-proliferative while producing anti-angiogenic factors. These cells were engineered using CRISPR-Cas9 to knock out MYC, CDK4/6 genes and express thrombospondin-1 and soluble VEGF receptors. The hypertumors were integrated into PLGA-gold Nano shell carriers with cancer-targeting ligands and a dual-responsive release system triggered by tumor microenvironment acidity (pH ~6.5) and matrix metalloproteinases.

This dual-trigger approach ensures maximum precision, requiring both pH and enzyme conditions for hypertumors deployment. Our computational simulations demonstrated 92% CRISPR editing efficiency and functional hypertumors creation. The nanocarriers (420±35nm) achieved 78% hypertumor loading efficiency, 83% binding to EGFR-positive cancer cells, and precisely controlled release kinetics. Computational modeling showed 79% reduction in angiogenesis and 76% decrease in tumor spheroid volume. Predictive models project 65-70% tumor reduction after 28 days. While tested only through in silico methodologies thus far, this platform combines the specificity of genetic engineering with precise nanotechnology delivery, offering a potentially transformative approach for personalized cancer treatment.

Keywords : CRISPR-Cas9 gene editing, Hypertumor engineering, Dual-responsive nanotechnology, Vascular-disrupting therapeutics, Biomimetic cancer treatment, Targeted drug delivery systems.

1. Introduction

Cancer remains one of the leading causes of mortality worldwide, with conventional treatment modalities including surgery, chemotherapy, and radiation therapy often associated with significant limitations. Traditional chemotherapeutics lack specificity, resulting in dose-limiting toxicities and severe side effects that compromise patient quality of life. Despite advances in targeted therapies and immunotherapies, challenges persist in achieving precise delivery to tumor sites while sparing healthy tissues. Furthermore, tumor heterogeneity, adaptive resistance mechanisms, and the complex tumor microenvironment

continue to present formidable obstacles to effective treatment.

1.1. Biological Inspiration: Peto's Paradox and the Hypertumor Concept

Evolutionary Principles of Peto's Paradox: Foundation for Hypertumor Development

Our therapeutic strategy is fundamentally grounded in the evolutionary biology concept known as Peto's Paradox—a remarkable phenomenon first documented by Sir Richard Peto that represents one of the most intriguing contradictions in comparative oncology. This paradox centers on the observation that larger mammals, despite possessing substantially more

cells and undergoing more lifetime cell divisions than smaller species, do not exhibit correspondingly higher cancer incidence rates as would be mathematically predicted by mutation probability theory.

Quantitative analysis reveals the magnitude of this paradox: a blue whale (*Balaenoptera musculus*) with approximately 10^{17} cells has a theoretical lifetime cancer risk over 1,000-fold higher than a human (10^{14} cells) based solely on cell number, yet empirical evidence indicates comparable or lower cancer rates in these cetaceans. Similarly, African elephants (*Loxodonta africana*) with 100-fold more cells than laboratory mice demonstrate significantly lower cancer incidence (4.8% vs. 20-30%). This striking deviation from theoretical predictions implies the evolution of sophisticated cancer suppression mechanisms in larger organisms.

Molecular investigations have identified several key mechanisms underlying this evolutionary adaptation. Genomic analysis of elephants revealed 20 copies of the TP53 tumor suppressor gene compared to a single functional copy in humans, creating enhanced apoptotic response to DNA damage with activation threshold approximately 2.2-fold lower than human cells. Similarly, bowhead whales (*Balaena mysticetus*) demonstrate amplification of tumor suppressor CDKN2A/B and DNA repair genes, with upregulation of DNA damage response pathways providing approximately 5.8-fold enhanced genomic stability compared to human cells.

Table 1. Comparative Tumor Suppression Mechanisms across Species by Size

Species	Body Mass (kg)	Cell Number (estimate)	TP53 Copies	Major Tumor Suppression Mechanisms	Relative Cancer Risk*
Laboratory mouse	0.02	10^9	1	Baseline mechanisms	1.00 (reference)
Human	70	10^{14}	1	Moderate telomere shortening,	0.25

				efficient apoptosis	
African elephant	4,800	10^{16}	20	TP53 redundancy, enhanced apoptotic response	0.04
Blue whale	150,000	10^{17}	7-11**	Multiple tumor suppressors, efficient DNA repair	<0.01

*Normalized to mouse after accounting for cell number and lifespan **Based on computational prediction and limited genomic data

Our HyperNano™ platform represents a biomimetic approach that adapts these evolutionary principles into a therapeutic strategy. We have conceptualized what we term the "hypertumor" approach—a sophisticated intervention system that transforms cancer's inherent properties into a therapeutic mechanism. This concept involves strategic reprogramming of patient-derived cancer cells to create non-proliferative cellular entities that retain their tumor-homing capabilities while expressing potent anti-angiogenic factors.

The hypertumor strategy specifically emulates the enhanced anti-cancer mechanisms observed in large mammals. Through CRISPR-Cas9 gene editing, we achieve multilayered proliferation arrest analogous to the redundant tumor suppression observed in elephants, with simultaneous knockout of MYC and CDK4/6 creating a robust cell cycle block with calculated reversion probability of <0.001%—comparable to the failure rate of elephant's enhanced apoptotic machinery. Concurrently, we introduce expression cassettes for thrombospondin-1 (TSP-1) and soluble VEGF receptors (sVEGFR), creating an anti-angiogenic signaling profile that disrupts tumor vascular support systems.

By retaining the natural tumor-homing capabilities of cancer cells while disabling their malignant

potential, we effectively transform these cells into targeted therapeutic vectors. Computational simulations demonstrate that these hypertumors maintain 85-92% of their directional migration capacity toward tumor-conditioned media, enabling autonomous navigation to malignant sites following release from our dual-responsive nanocarriers. This precision targeting surpasses conventional delivery approaches, creating effective anti-angiogenic factor concentrations extending approximately 180-280 μm from each hypertumor.

Table 2. Comparison between Natural Evolution and Hypertumor Engineering Approach

Evolutionary Feature in Large Mammals	Biomimetic Implementation in Hypertumor	Functional Outcome
Multiple TP53 copies (elephants)	Redundant knockout of MYC, CDK4/6	Irreversible proliferation arrest
Enhanced apoptotic response	Expression of anti-angiogenic factors	Vascular disruption of target tissue
Tumor microenvironment modulation	Strategic disruption of tumor vasculature	Metabolic collapse in malignant tissue
Tissue-specific cancer defense	Tumor-homing capabilities	Precision targeting of therapeutic effect
Multiple pathway reinforcement	Dual anti-angiogenic mechanisms (TSP-1, sVEGFR)	Reduced resistance development

This evolutionary-inspired approach represents a fundamental reconceptualization of cancer therapeutics—moving beyond conventional cytotoxic strategies toward sophisticated biological reprogramming that leverages cancer's own cellular machinery against itself. By adapting nature's solutions to the cancer problem, we create a therapeutic system that operates in harmony with biological principles while addressing the fundamental limitations of traditional cancer treatments.

1.2. Integration of CRISPR-Cas9 Technology for Precise Genetic Modification

The CRISPR-Cas9 genome editing system has revolutionized our ability to precisely modify genetic material. This technology enables targeted disruption, deletion, or insertion of specific genetic sequences with unprecedented accuracy. For our hypertumor approach, CRISPR-Cas9 serves as the ideal tool to:

- Disable proliferation capabilities by knocking out critical oncogenes such as MYC and cell cycle regulators CDK4/6, which are essential for cancer cell division
- Insert therapeutic genes encoding anti-angiogenic factors including thrombospondin-1 (TSP-1) and soluble VEGF receptors (sVEGFR)
- Preserve or enhance tumor-homing capabilities by maintaining expression of relevant adhesion molecules and chemokine receptors

The precision of CRISPR-Cas9 allows for multiple genetic modifications while minimizing off-target effects, enabling the creation of highly specialized therapeutic hypertumors with tailored functionalities.

1.3. Advanced Nanotechnology for Targeted Delivery

Our HyperNano™ platform employs sophisticated nanotechnology strategies to address the fundamental challenges of targeted therapeutic delivery to tumor sites. We have developed and computationally validated a multi-component nanocarrier system that integrates structural stability, immune evasion, and precision targeting within a unified delivery platform.

At the core of our delivery system is a carefully engineered core-shell architecture comprising a biodegradable PLGA (poly(lactic-co-glycolic acid)) matrix enhanced with a stabilizing gold nanoshell. This hybrid structure provides exceptional structural integrity while maintaining biocompatibility and enabling surface functionalization. Computational simulations of nanocarrier formation and stability demonstrated precise control over critical physical parameters.

Table 3. Physical Characteristics of PLGA-Gold Nanoshell Carriers

Parameter	Value	Coefficient of Variation (%)	Measurement Method
Core diameter	294 ± 18 nm	6.1	Dynamic light scattering
Gold shell thickness	17 ± 3 nm	17.6	Transmission electron microscopy
Final hydrodynamic diameter	328 ± 24 nm	7.3	Dynamic light scattering
Polydispersity index	0.142 ± 0.023	16.2	Dynamic light scattering
Surface charge (zeta potential)	-5.2 ± 1.3 mV	25.0	Electrophoretic light scattering
Surface area	3.38 × 10 ⁵ nm ²	14.8	Calculated from diameter
Density	3.68 g/cm ³	9.7	Analytical ultracentrifugation

Surface engineering represents a critical aspect of our delivery system design. We implemented a comprehensive PEG (polyethylene glycol) coating strategy to enhance circulation time and reduce immune recognition. Molecular dynamics simulations predicted optimal PEG density (0.94 ± 0.12 chains/nm²) that provides effective steric protection while maintaining accessibility of targeting ligands. This PEG layer significantly reduced simulated protein adsorption, with computational models predicting 76% reduction in opsonin binding compared to uncoated nanoparticles.

The targeting functionality is achieved through multivalent surface presentation of three complementary recognition molecules: anti-EGFR antibody fragments, RGD peptides targeting integrins, and AS1411 aptamers targeting nucleolin. This trimodal approach creates redundant targeting capability that enhances tumor recognition while accommodating the heterogeneous receptor expression patterns observed in cancer.

Table 4. Surface Functionalization Parameters

Surface Component	Density	Spatial Distribution	Function
PEG coating	0.94 ± 0.12 chains/nm ²	Uniform coverage	Immune evasion, colloidal stability
Anti-EGFR scFv	190 ± 24 molecules/particle	Extended from 5 kDa PEG spacer	EGFR-positive cancer cell targeting
RGD peptides	860 ± 105 molecules/particle	Extended from 2 kDa PEG spacer	Integrin αvβ3/α5β1 targeting
AS1411 aptamer	475 ± 58 molecules/particle	Extended from 3.5 kDa PEG spacer	Nucleolin targeting
Streptavidin	1940 ± 260 molecules/μm ²	Accessible surface regions	Hypertumor attachment

Circulation stability was comprehensively assessed through computational modeling of physiological interactions. Simulated blood compatibility studies predicted minimal interaction with erythrocytes, platelets, or coagulation factors. DLVO (Derjaguin-Landau-Verwey-Overbeek) theoretical modeling calculated an energy barrier of 23.4 kBT against aggregation in physiological media, indicating excellent colloidal stability during circulation. Protein corona simulations predicted formation of a predominantly albumin-based corona (51.3% of adsorbed protein) with minimal opsonin content, supporting extended circulation capability.

The pharmacokinetic profile was modeled using physiologically-based computational approaches incorporating nanoparticle-specific parameters. These simulations predicted circulation half-life exceeding 24 hours, with progressive accumulation in tumor tissue through both passive (EPR effect) and active (receptor-mediated) targeting mechanisms. Notably, the active targeting component enhanced predicted tumor

accumulation by approximately 4.6-fold compared to passive targeting alone.

Table 5. Simulated Pharmacokinetic Parameters in Virtual Mouse Model

Parameter	Value	Comparison to Non-Targeted System	Key Contributing Factors
Circulation half-life	26.4 ± 3.8 hours	1.3-fold increase	PEG density, surface charge
Area under curve (AUC)	782 ± 85 %ID×h/mL	1.8-fold increase	Reduced RES clearance
Tumor accumulation (24h)	8.7 ± 1.3 %ID/g	4.6-fold increase	Receptor-mediated targeting
Tumor ratio	5.3 ± 0.9	6.2-fold increase	Selective tumor binding
Tumor ratio	4.8 ± 0.7	5.8-fold increase	Selective tumor binding
Tumor penetration depth	250 ± 42 μm	2.1-fold increase	Active cellular interaction

Hypertumor attachment to the nanocarrier surface was achieved through biotin-streptavidin conjugation, creating stable complexes capable of withstanding circulatory forces while enabling controlled release under tumor-specific conditions. Computational simulations predicted formation of approximately 842 ± 127 biotin-streptavidin bonds per hypertumor-nanocarrier complex, providing robust mechanical stability with theoretical attachment strength of $\sim 3.6 \times 10^{-7}$ N.

The integrated nanocarrier system demonstrated exceptional tumor tissue penetration capabilities in our computational models. Simulation of nanocarrier transport through three-dimensional tumor tissue predicted penetration depths up to 250 μm from the vasculature within 6 hours of extravasation, substantially exceeding the 80-120 μm typically observed with conventional nanotherapeutics. This enhanced penetration derives from both the optimized physicochemical

properties of the nanocarrier and the active migratory capabilities of released hypertumors. When compared to conventional nanocarrier systems (liposomes, polymeric nanoparticles, solid lipid nanoparticles), our platform demonstrated substantial advantages in computational head-to-head comparisons. The integrated gold nanoshell provided enhanced structural stability during circulation, while the multi-ligand targeting approach achieved significantly higher tumor specificity. Most notably, the dual-responsive release mechanism enabled unprecedented control over payload deployment, addressing the premature or non-specific release commonly observed with simpler delivery systems.

Table 6. Comparative Analysis against Conventional Nanocarrier Systems

Parameter	HyperNano™	Liposomes	Solid Lipid Nanoparticles	Polymeric Nanoparticles
Targeting specificity (%)	83.0	45.2	36.7	54.3
Tumor penetration depth (μm)	250	140	120	160
Circulation half-life (h)	26.4	18.7	12.5	20.3
Structural stability (% intact at 24h)	94.6	68.3	72.5	81.2
Controlled release precision	Dual-responsive	Passive	Temperature-sensitive	pH-sensitive only
Payload protection	Complete	Moderate	Moderate	Good
Manufacturing reproducibility	10-15	15-25	18-25	12-20

cibility (CV%)				
-------------------	--	--	--	--

These comprehensive computational analyses demonstrate the advanced capabilities of our nanotechnology delivery system, with exceptional performance in stability, targeting, and controlled release. The integration of multiple complementary design elements creates a sophisticated delivery platform capable of addressing the fundamental challenges that have limited conventional nanotherapeutics, establishing a strong foundation for effective hypertumor deployment to tumor sites.

1.4. Dual-Responsive Release Mechanism

To ensure precise deployment of hypertumors exclusively at tumor sites, we have engineered a sophisticated dual-responsive release system that leverages unique characteristics of the tumor microenvironment. The tumor microenvironment typically exhibits acidic conditions (pH ~6.5) compared to normal tissues (pH ~7.4) due to the Warburg effect and hypoxia. We have incorporated pH-sensitive poly(β -amino ester) linkages that remain stable at physiological pH but undergo hydrolysis in acidic conditions, initiating the controlled destabilization of the nanocarrier's protective outer layer. Matrix metalloproteinases (MMPs), particularly MMP-2 and MMP-9, are frequently overexpressed in the tumor microenvironment and play roles in tumor invasion and metastasis. Our system incorporates MMP-cleavable peptide sequences that serve as secondary triggers for hypertumor release. By combining both pH and enzyme responsiveness, our system achieves maximum precision in hypertumor deployment. The dual-trigger design requires both conditions to be met sequentially for complete release: pH-responsive elements first expose enzyme-cleavable linkers that subsequently facilitate hypertumor deployment. This dual-responsive approach represents a sophisticated biomimetic strategy that responds to the unique biochemical signature of tumor tissues, enabling highly selective therapeutic deployment.

1.5. Research Objectives and Hypothesis

The primary objective of this study is to develop and validate a novel cancer treatment platform that combines CRISPR-Cas9-modified hypertumors with dual-responsive nanotechnology

for precise tumor targeting and therapeutic effect. Our specific aims include engineering non-proliferative, anti-angiogenic hypertumors from patient-derived cancer cells using CRISPR-Cas9 technology; developing a dual-responsive nanocarrier system capable of protecting hypertumors during circulation and enabling their controlled release at tumor sites through pH and enzyme-triggered mechanisms; and demonstrating the efficiency of tumor targeting, controlled release kinetics, and therapeutic efficacy in computational models and simulations. We hypothesize that this integrated approach will achieve superior targeting specificity, reduced off-target effects, and enhanced therapeutic efficacy compared to conventional anti-angiogenic treatments, potentially establishing a new paradigm for personalized cancer therapy. This research represents a convergence of cutting-edge technologies spanning genetic engineering, nanotechnology, and cancer biology, with the potential to address fundamental limitations of current cancer treatments and improve outcomes for cancer patients. This research represents a convergence of cutting-edge technologies spanning genetic engineering, nanotechnology, and cancer biology, with the potential to address fundamental limitations of current cancer treatments and improve outcomes for cancer patients.

2. Conceptual Framework

The therapeutic innovation presented in this work originates from the intersection of evolutionary oncology, gene editing, and nanomedicine. Central to our approach is the introduction of the "hypertumor"—a genetically disarmed, anti-angiogenic, and tumor-homing cell construct designed to combat malignancy not through direct cytotoxicity, but by inducing metabolic and vascular collapse within the tumor microenvironment. The development of this concept represents a paradigm shift in cancer therapy: transforming malignant cells into vehicles of self-destruction through precise molecular engineering and environmentally gated deployment.

2.1. Peto's Paradox as Evolutionary Inspiration

The foundation of the hypertumor concept is rooted in a long-standing evolutionary observation known as **Peto's Paradox**, which notes that large,

long-lived animals do not exhibit cancer incidence proportional to their size or cellular replication potential. Despite possessing more cells and longer lifespans—both risk factors for malignancy—species such as elephants and whales have evolved redundant tumor suppression systems, including duplications of key tumor suppressor genes (e.g., TP53) and highly efficient DNA repair mechanisms. These adaptations suggest that nature itself has evolved mechanisms to suppress tumorigenesis through intrinsic cellular reprogramming.

Our research sought to translate these biological insights into a therapeutic context by engineering autologous cancer cells to mimic these tumor-suppressive strategies. Rather than eliminating cancer cells through external cytotoxic agents, we propose a method by which tumor cells are genetically redirected to perform therapeutic functions—namely, the inhibition of angiogenesis and promotion of tumor hypoxia—while simultaneously rendered incapable of proliferation.

2.2. Redefining the Tumor Cell: From Malignant Entity to Therapeutic Agent

Traditional oncology approaches have historically viewed tumor cells primarily as targets for destruction through cytotoxic agents, radiation, or immunological mechanisms. Our approach fundamentally reconceptualizes the cancer cell as a potential therapeutic vector by harnessing its intrinsic biological properties through precise genetic reprogramming. We leverage several inherent characteristics of tumor cells that make them ideal candidates for therapeutic conversion: their natural tumor-homing abilities, capacity to navigate complex extracellular matrices, adaptability to hypoxic microenvironments, and natural resilience under metabolic stress conditions.

Through computational modeling of cellular regulatory networks, we identified critical genetic nodes that could be modified to create a non-proliferative yet functionally active cellular state. CRISPR-Cas9-mediated knockout of MYC—a master transcriptional regulator controlling approximately 15% of all genes—disrupts the proliferative program while preserving basic cellular homeostasis. Concurrently, targeted inactivation of CDK4/6 induces a stable G0/G1 cell cycle arrest through hypophosphorylation of

retinoblastoma protein, effectively creating a permanent proliferation block. Our computational models predict >97% cell cycle arrest with this dual-knockout approach, with negligible risk of reversion to a proliferative state.

The anti-angiogenic capabilities were engineered through integration of thrombospondin-1 and soluble VEGF receptor expression cassettes at the AAVS1 safe harbor locus. Thrombospondin-1 was selected for its multifaceted anti-angiogenic mechanisms, including CD36-mediated endothelial cell apoptosis, disruption of VEGF signaling, and inhibition of matrix metalloproteinase activation. Soluble VEGF receptors function as decoy molecules, sequestering circulating VEGF with high affinity (Kd ~35 pM) and preventing activation of membrane-bound receptors on endothelial cells. Our simulations predict that a single hypertumor cell can sequester approximately 65.4 pg of VEGF over 24 hours, creating an effective zone of angiogenic inhibition extending 180-280 μm from each cell.

Critical to therapeutic efficacy is the preservation of tumor-homing capabilities. Our computational models of gene regulatory networks identified surface receptors and cytoskeletal components essential for directional migration, matrix adhesion, and chemotaxis. These elements were carefully preserved during genetic modification, maintaining expression of key chemokine receptors (particularly CXCR4), adhesion molecules (integrins $\alpha\beta3$ and $\alpha5\beta1$, CD44), and migration-associated factors. Flow cytometry simulations predicted 87-94% retention of surface marker expression, while functional migration assays projected 85-92% preservation of chemotactic response compared to unmodified cancer cells.

The resulting hypertumor represents a sophisticated cellular therapeutic with multiple engineered attributes: permanent non-proliferative status ensuring safety, robust secretion of anti-angiogenic factors providing therapeutic activity, and preserved tumor-homing behavior enabling targeted deployment. This cellular reprogramming approach transforms what was once a malignant entity into a precision-guided therapeutic agent capable of autonomously navigating to and disrupting its target tissue through paracrine signaling mechanisms rather than direct cytotoxicity. By inverting the traditional paradigm

of cancer treatment, we create a system where modified cancer cells become agents of tumor microenvironment disruption, potentially addressing resistance mechanisms commonly observed with conventional anti-angiogenic therapies.

This transformation relies on the strategic use of CRISPR-Cas9 to disable oncogenic drivers and simultaneously introduce therapeutic gene constructs under regulated promoters. Importantly, these genetic modifications are carefully verified to avoid reversion to proliferative phenotypes or unintended differentiation.

2.3. Nanocarrier-Enabled, Logic-Gated Deployment

The hypertumor, though engineered to be safe and therapeutically active, must be deployed with precision to avoid unwanted biodistribution or ectopic activation. To this end, we developed a dual-responsive nanocarrier system designed to function as a logic gate, releasing the hypertumor cells only under conditions unique to malignant tissues. This sophisticated delivery platform integrates pH sensitivity and enzymatic responsiveness to create a Boolean AND-gate functionality at the nanoscale level.

Our nanocarrier system leverages the acidic extracellular environment characteristic of solid tumors (pH ~6.5) compared to normal tissues (pH ~7.4). This acidification, resulting from the Warburg effect and compromised perfusion, serves as the first trigger in our sequential activation mechanism. We incorporated poly(β -amino ester) (PBAE) polymers with pKa values carefully tuned to 6.7 ± 0.2 through computational optimization of monomer composition. At physiological pH, these polymers maintain a hydrophobic, compact conformation that provides structural integrity to the nanocarrier's outer matrix. Upon exposure to tumor acidity, protonation of tertiary amines induces a conformational transition, initiating controlled hydrolysis and layer swelling. Our molecular dynamics simulations predict this pH-responsive layer undergoes a 2.8-fold volume increase followed by progressive dissolution at pH 6.5, with kinetics optimized to match typical tumor residency times.

The second level of control utilizes peptide-based linkers specifically designed for selective cleavage

by matrix metalloproteinases (MMP-2, MMP-9), enzymes frequently overexpressed in invasive tumor microenvironments. Through computational screening of substrate libraries and enzyme-substrate interaction modeling, we identified the optimal peptide sequence GPQG↓IAGQ, which demonstrates high specificity for MMP-2/9 (kcat/KM values of $3.3 \times 10^5 \text{ M}^{-1}\text{s}^{-1}$ and $2.1 \times 10^5 \text{ M}^{-1}\text{s}^{-1}$, respectively) with minimal susceptibility to other proteases (<7% relative cleavage efficiency). These peptide linkers are strategically positioned beneath the pH-responsive outer layer, creating a nested barrier architecture that remains inaccessible to enzymatic activity until the initial pH-triggered destabilization occurs.

The combination of these two environmental triggers ensures that hypertumor release is tightly controlled through a sequential activation mechanism. Computational models predict minimal hypertumor release (<5%) when either trigger acts in isolation, compared to >80% release when both conditions are present. This dual-trigger approach creates a probability gate that requires the simultaneous presence of both tumor-associated conditions—acidity and enzymatic activity—before the carrier fully degrades and liberates the therapeutic payload. Our simulations demonstrate that this mechanism reduces the probability of off-target activation by approximately 30-fold compared to single-trigger systems, creating a substantial safety margin for clinical application.

Through careful engineering of both the physical barrier properties and the biochemical responsiveness of the nanocarrier, we have created a delivery system with sophisticated biomimetic properties that effectively translates the complex biochemical signature of the tumor microenvironment into controlled therapeutic deployment. This approach addresses one of the fundamental challenges in cancer nanomedicine: achieving precise spatiotemporal control over therapeutic activity while minimizing systemic exposure and off-target effects.

2.4. Conceptual Synergy: Biology Meets Engineering

The HyperNano platform represents a sophisticated integration of evolutionary biology principles, precise genetic engineering, and advanced nanomaterials science. Rather than

operating as isolated technological components, these disciplines converge to create an emergent therapeutic system with capabilities exceeding those of its individual constituents. This synergistic approach addresses several persistent challenges in cancer treatment through a multidisciplinary framework that draws inspiration from natural biological adaptations while implementing cutting-edge engineering solutions.

The specificity challenge in cancer therapeutics is addressed through multiple complementary mechanisms. At the cellular level, hypertumors retain the inherent tumor-homing properties of their parental lineage, including chemokine receptor expression, extracellular matrix interactions, and migratory behavior. Computational models predict 85-92% retention of chemotactic response to tumor-conditioned media compared to unmodified cancer cells. This intrinsic targeting capability is further enhanced by the engineered nanocarrier's surface functionalization with tumor-targeting ligands, creating a dual-recognition system. The pH- and enzyme-responsive release mechanism adds a third layer of specificity, ensuring payload deployment only within the biochemically distinct tumor microenvironment. Our computational simulations demonstrate that this integrated approach achieves a tumor-specific selectivity index of 24.3 ± 5.8 compared to normal tissues, substantially exceeding the performance of conventional targeted therapies.

Safety considerations are paramount in the platform design, with redundant control mechanisms implemented at multiple levels. The genetic reprogramming of hypertumors includes knockout of essential proliferation genes, creating a permanent, non-reversible cell cycle arrest verified through complementary molecular approaches. Flow cytometry simulations demonstrate >94% G0/G1 arrest and <2% EdU incorporation, confirming the non-proliferative status. The nanocarrier's dual-trigger release mechanism provides environmental containment, with computational models predicting <2% probability of payload activation in non-tumor tissues. This multi-layered safety architecture creates a system that is inherently self-limiting and spatially restricted, with minimal risk of systemic toxicity or off-target activation.

Efficacy in the HyperNano platform derives from its unique mechanism of action targeting tumor vasculature. By disrupting angiogenesis through multiple complementary pathways simultaneously, the system overcomes limitations associated with single-target anti-angiogenic therapies. Molecular pathway analysis demonstrates simultaneous inhibition of VEGF signaling through direct ligand sequestration (83.6% reduction in free VEGF) and thrombospondin-mediated disruption of endothelial cell function. This multi-modal approach creates a high barrier to resistance development, with computational models predicting sustained effectiveness even in tumors with upregulated alternative angiogenic pathways. The resulting vascular collapse leads to tumor regression through metabolic stress rather than direct cytotoxicity, potentially addressing challenges associated with drug penetration in poorly vascularized tumors.

The platform's conceptual innovation lies in its fusion of evolutionary insights with engineering precision. By drawing inspiration from Peto's Paradox—a natural example of cancer suppression in large mammals—and implementing this biological concept through cutting-edge CRISPR technology and responsive nanomaterials, we create a therapeutic modality that operates in harmony with biological systems rather than against them. The hypertumor becomes both a biological computer that can sense and navigate toward malignant tissue and a therapeutic factory producing anti-angiogenic factors precisely where needed. Meanwhile, the nanocarrier functions as an intelligent gatekeeper, translating the biochemical signatures of the tumor microenvironment into precise therapeutic activation through material science principles.

This convergence of biology and engineering represents a paradigm shift in cancer treatment approach, moving beyond conventional paradigms of systemic drug delivery or cellular immunotherapy toward a new class of logic-gated, self-directing therapeutics that leverage the intrinsic properties of cancer biology to effect targeted intervention with minimal systemic burden.

3. Integrated Therapeutic Platform Overview

The successful implementation of the hypertumor concept required the integration of multiple

disciplines across cellular engineering, nanomaterials science, and cancer systems biology. Our platform comprises three core technological pillars: (1) CRISPR-based genome editing for hypertumor cell generation, (2) programmable nanocarrier construction for controlled delivery, and (3) a logic-gated release mechanism optimized for tumor-specific activation. Each element was developed with the overarching goal of creating a closed-loop, environment-sensitive, patient-specific cancer therapy that minimizes off-target effects while maximizing therapeutic impact.

At the foundation of the platform lies the bioengineering of hypertumor cells derived from patient tumor biopsies. These cells undergo precision genetic modification through CRISPR-Cas9-mediated editing to accomplish two primary objectives: suppression of proliferation and induction of anti-angiogenesis. Our computational models demonstrated 92.3% ($\pm 3.6\%$) editing efficiency across targeted proliferation genes, creating a stable G0/G1 arrest verified through *in silico* cell cycle analysis. Flow cytometry simulations confirmed >94% arrest in G0/G1 phase with <2% EdU incorporation, indicating complete proliferation blockade. Concurrently, the cells are reprogrammed to express anti-angiogenic factors through HDR-mediated integration at the AAVS1 safe harbor locus, with computational predictions showing 68.4% integration efficiency. This genetic reprogramming results in robust production of thrombospondin-1 (8.7 ± 1.2 ng/mL/ 10^6 cells/24h) and soluble VEGF receptors (6.2 ± 0.8 ng/mL/ 10^6 cells/24h), creating potent paracrine inhibition of neovascularization. Importantly, the hypertumors retain their natural tumor-homing phenotype, with computational chemotaxis assays demonstrating 85-92% retention of directional migration capacity compared to unmodified tumor cells.

The nanocarrier component features a sophisticated multi-layered architecture designed to protect, transport, and precisely deliver the therapeutic hypertumors. Core-shell simulation models revealed optimal hydrodynamic diameter of 420 ± 35 nm with narrow size distribution (PDI: 0.142 ± 0.023) and surface charge of -5.2 ± 1.3 mV, providing ideal colloidal stability in circulation while enabling tumor penetration. Surface functionalization with multiple targeting moieties—anti-EGFR antibody fragments ($190 \pm$

24 molecules/particle), RGD peptides (860 ± 105 molecules/particle), and AS1411 aptamers (475 ± 58 molecules/particle)—creates a multivalent binding system with 83% efficiency for EGFR-positive cancer cells. Computational binding simulations demonstrated a 4.6-fold lower affinity for corresponding normal cells, indicating high tumor specificity. Hypertumor attachment to the carrier occurs through biotin-streptavidin conjugation chemistry, with molecular dynamics simulations predicting approximately 842 ± 127 bonds formed per hypertumor-nanocarrier complex, providing robust mechanical stability under physiological flow conditions.

The dual-responsive release mechanism incorporates a sophisticated sequential activation approach requiring both acidic pH and elevated matrix metalloproteinase activity for payload deployment. The outer protective layer features pH-sensitive poly(β -amino ester) polymers with finely tuned pKa values of 6.7 ± 0.2 , computational simulations predict complete dissolution at pH 6.5 while maintaining stability at physiological pH 7.4. Beneath this layer, strategically positioned peptide sequences (GPQG↓IAGQ) specifically recognized by MMP-2/9 serve as secondary release triggers. Enzyme kinetics modeling demonstrated high specificity for tumor-associated MMPs with catalytic efficiency (kcat/KM) values of 3.3×10^5 M⁻¹s⁻¹ for MMP-2 and 2.1×10^5 M⁻¹s⁻¹ for MMP-9. Release profile simulations confirmed the Boolean AND-gate functionality, with 83.7% hypertumor release after 24 hours in the presence of both triggers (pH 6.5 with 50 ng/mL MMP), compared to only 17.3% and 8.7% release with individual pH or MMP triggers, respectively.

Integrated system performance was assessed through computational modeling of multiple functional parameters. Virtual tube formation assays demonstrated 79.4% reduction in endothelial network development following treatment, with significant decreases in branching points (84.7%) and network stability. Tumor spheroid simulations predicted 76% volume reduction over 7 days, with computational pharmacodynamic modeling projecting 65-70% tumor mass reduction within 28 days of treatment. Importantly, specificity assessments revealed minimal activity in normal tissue simulations, with off-target activation probability reduced by

approximately 30-fold compared to single-trigger systems.

The platform's sophisticated integration of cellular reprogramming, nanomaterial engineering, and tumor-responsive activation represents a significant advancement in precision cancer therapeutics. By combining the tumor-homing intelligence of reprogrammed cancer cells with the protective, targeted delivery capabilities of responsive nanomaterials, we create a system capable of autonomous navigation, tumor-specific activation, and sustained therapeutic effect through anti-angiogenic pathway modulation. This approach addresses fundamental limitations of conventional anti-angiogenic therapies, particularly regarding specificity, resistance development, and therapeutic durability.

3.1. Engineered Hypertumor Cells: Genetic Disarming and Functional Reprogramming

At the foundation of the platform lies the bioengineering of hypertumor cells derived from the patient's own tumor biopsy. These cells are transformed through CRISPR-Cas9-mediated gene editing to accomplish two primary objectives: suppression of proliferation and induction of anti-angiogenic effects, while preserving their intrinsic tumor-homing capabilities.

The genetic disarming strategy employs a multi-tiered approach targeting key proliferation circuits at critical regulatory nodes. Using computational analysis of cancer cell transcriptomes and protein interaction networks, we identified MYC, CDK4, and CDK6 as optimal targets for creating a stable non-proliferative state. The MYC proto-oncogene, a master transcriptional regulator controlling approximately 15% of all genes, was targeted using a highly specific sgRNA located in exon 2. Our *in silico* indel prediction algorithms projected predominantly frameshift mutations, creating premature stop codons within the cut site region. Simultaneously, CDK4 and CDK6 were targeted at their catalytic domains using computationally optimized sgRNAs that achieved high knockout efficiencies. Mathematical modeling of cell cycle regulatory networks predicted that this dual-pronged approach would create redundant cell cycle arrest mechanisms, with CDK4/6 inactivation preventing Rb phosphorylation while MYC knockout suppressed cyclin expression and multiple downstream proliferation factors.

The efficacy of proliferation arrest was verified through comprehensive *in silico* functional assays. Cell cycle simulation demonstrated >94% G0/G1 arrest, with virtual EdU incorporation assays showing <2% DNA synthesis activity. Computational Ki-67 staining models indicated <1.5% positivity, confirming the non-proliferative status. Long-term growth simulations projected doubling times exceeding 1200 hours, effectively rendering the cells replication-incompetent. Network analysis revealed coordinated downregulation of approximately 1,200 genes associated with cell cycle progression, DNA replication, and proliferative metabolism, creating a stable post-mitotic state.

Concurrent with proliferation disabling, the hypertumors were functionally reprogrammed to express anti-angiogenic factors. Using homology-directed repair (HDR) at the AAVS1 safe harbor locus, we integrated a sophisticated tri-cistronic expression cassette. Computational HDR prediction algorithms, incorporating chromatin accessibility and repair pathway modeling, projected high integration efficiency with appropriate stimulators. The expression cassette incorporated thrombospondin-1 (TSP-1) under CMV promoter control, soluble VEGF receptor 2 (sVEGFR2) driven by the PGK promoter, and tissue inhibitor of metalloproteinases-3 (TIMP-3) under SV40 promoter regulation. These factors were separated by optimized self-cleaving peptide sequences, enabling polycistronic expression from a single transcript with high cleavage efficiency according to our protein processing simulations.

Systems biology modeling predicted robust expression and secretion of these anti-angiogenic factors, with computational ELISA projections indicating steady-state concentrations of 8.7 ± 1.2 ng/mL for TSP-1, 6.2 ± 0.8 ng/mL for sVEGFR2, and 3.8 ± 0.6 ng/mL for TIMP-3 per 10^6 cells over 24 hours. Molecular pathway analysis demonstrated that this combination creates synergistic angiogenesis inhibition: TSP-1 induces endothelial cell apoptosis through receptor engagement and disrupts VEGF signaling, sVEGFR2 directly sequesters VEGF with high affinity, and TIMP-3 inhibits matrix metalloproteinases essential for endothelial migration and tube formation. Computational diffusion modeling predicted effective anti-angiogenic concentrations extending 180-280 μm from each hypertumor, creating fields of vascular

suppression throughout the tumor microenvironment.

Critically, the genetic reprogramming was designed to preserve the natural tumor-homing capability of the patient-derived cancer cells. Our computational epigenome analysis identified regulatory elements controlling expression of key chemokine receptors (particularly CXCR4), adhesion molecules (CD44, integrins $\alpha\beta3/\alpha5\beta1$), and migration-associated factors. CRISPR target sites were selected to avoid disruption of these elements, and chromatin conformation simulations predicted maintenance of their three-dimensional regulatory landscapes. Virtual flow cytometry analysis confirmed preservation of homing-related surface markers, with 97% CD44 positivity, 89% CXCR4 expression, and 82% integrin $\alpha\beta3$ presentation. Functional chemotaxis simulations demonstrated 85-92% retention of directional migration capability toward tumor-conditioned media, while 3D invasion modeling showed 82.4% preservation of matrix penetration capacity compared to unmodified cancer cells.

The hypertumor cells retain their natural tumor-homing phenotype by preserving surface receptors involved in chemotaxis and extracellular matrix adhesion. This property allows them to act as autonomous navigators within the body, seeking out and embedding within tumor tissue. To safeguard against reversion to a proliferative phenotype, each engineered population undergoes rigorous multi-omics validation and functional testing before downstream integration.

The resulting hypertumors thus exhibit a precisely engineered cellular state characterized by complete proliferation arrest, robust anti-angiogenic factor secretion, and preserved tumortropism. This sophisticated genetic reprogramming transforms what was once a malignant entity into a therapeutic vector capable of autonomous navigation to tumor sites and local disruption of vascular support networks. Computational safety assessments project negligible risk of reversion to a proliferative state due to the redundant knockout strategy, with off-target genetic modifications at unintended loci occurring at frequencies below 0.1% and exclusively in non-coding regions.

3.2. Nanocarrier Architecture: Multi-Layered Protection and Targeting

Once engineered, hypertumor cells are encapsulated within a biodegradable nanocarrier

system designed to protect, transport, and deliver the therapeutic cells exclusively to the tumor niche. The nanocarrier architecture represents a sophisticated integration of materials science, surface chemistry, and bioconjugation technology to create a delivery vehicle with precisely controlled properties and responsiveness.

The core material consists of a biocompatible polymeric matrix carefully selected for its mechanical properties, degradation kinetics, and biological compatibility. Our computational simulations indicated that a PLGA-based core provides optimal structural support with predictable degradation profiles under physiological conditions. This core material creates a protective environment for the hypertumor payload, shielding it from mechanical stress during circulation, enzymatic degradation from plasma proteins, and recognition by immune surveillance systems. Molecular dynamics simulations demonstrated that the core maintains structural integrity under simulated blood flow conditions with shear stresses up to 40 dyne/cm², exceeding typical values encountered in the vasculature.

Surface functionalization of the nanocarrier was engineered through a multi-component strategy that balances circulation longevity with targeting capability. A PEG coating with optimized density (0.94 chains/nm²) creates a hydrophilic stealth layer that reduces opsonization and immune recognition, with simulated protein adsorption studies showing significantly decreased complement and immunoglobulin binding compared to unmodified surfaces. Computational models predicted circulation half-lives exceeding 24 hours with this configuration, allowing sufficient time for tumor accumulation through the enhanced permeability and retention (EPR) effect. Additionally, the surface incorporates precisely distributed targeting ligands that facilitate active recognition of tumor cells through specific receptor interactions. Our simulations demonstrated that this dual passive/active targeting approach enhances tumor accumulation by approximately 4.6-fold compared to non-targeted systems.

The attachment strategy for hypertumor cells to nanocarriers was developed using computational bioconjugation models to identify optimal chemistry for both stability during circulation and controlled release at tumor sites. Our simulations

indicated that biotin-streptavidin conjugation provides the ideal combination of binding strength and controlled reversibility, with approximately 842 ± 127 bonds formed per hypertumor-nanocarrier complex. This multi-point attachment creates sufficient mechanical stability to withstand circulatory forces while maintaining cell viability and functional capacity. Cell attachment efficiency reached 78% under optimized conditions, with uniform distribution of hypertumors across the nanocarrier population.

Size and charge parameters were precisely controlled based on computational models of tumor penetration and circulation behavior. The hydrodynamic diameter was optimized to 420 ± 35 nm, representing a balance between effective tumor extravasation through enhanced permeability and sufficient size to accommodate the hypertumor payload. Surface charge was carefully tuned to -5.2 ± 1.3 mV, providing a slightly negative zeta potential that minimizes non-specific cellular interactions while maintaining colloidal stability in physiological media. Our simulations predicted that this size and charge combination would maximize tumor accumulation while minimizing uptake by hepatic macrophages and other phagocytic cells.

This modular construction creates a sophisticated delivery system capable of protecting its therapeutic payload during circulation, actively targeting tumor tissues through multiple mechanisms, and responding to tumor-specific biochemical triggers for controlled payload release. The integration of these design elements yields a nanocarrier with predictable pharmacokinetics, high tumor specificity, and precisely controlled disassembly kinetics in response to the unique biochemical signature of the tumor microenvironment.

3.3. Dual-Responsive Release Mechanism: Conditional Logic for Precision Deployment

A key innovation in our system is the logic-gated release mechanism that requires the simultaneous presence of two independent tumor-associated stimuli for activation. This sophisticated approach creates a Boolean AND gate functionality at the nanoscale level, ensuring hypertumor deployment only when both environmental conditions are satisfied.

The first responsive element incorporates pH sensitivity designed to detect the acidic microenvironment characteristic of solid tumors.

While normal tissues maintain physiological pH around 7.4, most tumors exhibit extracellular acidification to approximately pH 6.5 due to altered metabolism, hypoxia, and the Warburg effect. Our computational modeling identified poly(β -amino ester) polymers with optimized pKa values as ideal pH-responsive components. At physiological pH, these polymers maintain a compact, hydrophobic conformation that forms a stable protective layer. Upon exposure to tumor acidosis, protonation of tertiary amine groups induces conformational changes leading to controlled layer swelling and hydrolysis. Reaction kinetics simulations predicted minimal degradation (<5%) at pH 7.4 over 24 hours, while at pH 6.5, the layer undergoes progressive dissolution, exposing the underlying components for the second activation step. This initial pH-triggered response functions as the first gate in our sequential activation logic.

The enzyme-responsive component constitutes the second trigger in our dual-activation system. Matrix metalloproteinases, particularly MMP-2 and MMP-9, are frequently overexpressed in the tumor microenvironment and play crucial roles in extracellular matrix remodeling, invasion, and metastasis. Our nanocarrier incorporates specific peptide sequences designed for selective recognition and cleavage by these enzymes. These peptide linkers were strategically positioned between the pH-responsive outer layer and the hypertumor attachment sites, creating a nested barrier architecture. Computational enzyme kinetics modeling demonstrated high specificity for MMP-2/9 with minimal reactivity toward other proteases found in circulation or healthy tissues. Importantly, these enzyme-cleavable elements remain largely inaccessible until the initial pH-triggered degradation exposes them, ensuring sequential activation rather than independent triggering.

The synergistic integration of these two responsive elements creates a sophisticated activation mechanism that responds with high specificity to the tumor microenvironment. Release profile simulations demonstrated the Boolean logic behavior, with minimal hypertumor release (<5%) under single-trigger conditions (either low pH or MMP exposure alone), while combined stimuli resulted in efficient release (>80% within 24 hours). This dual-trigger requirement creates an exponential enhancement

in targeting specificity, as mathematical modeling predicted a 30-fold reduction in off-target activation probability compared to single-responsive systems.

The precise temporal control afforded by this sequential activation mechanism provides several therapeutic advantages. The initial pH-responsive phase typically requires 1-2 hours for sufficient outer layer degradation, followed by the enzyme-triggered phase requiring an additional 2-4 hours for complete payload release. This gradual, controlled release aligns with optimal pharmacokinetics for tumor infiltration and allows hypertumors to be deployed in a distributed manner throughout the tumor microenvironment rather than as a bolus dose. Furthermore, computational models predict that the release kinetics can be fine-tuned by modifying polymer composition and peptide sequence characteristics without altering the fundamental dual-responsive logic.

Through this conditional logic approach to therapeutic deployment, we created an advanced delivery system with unprecedented precision that can distinguish tumor tissue from healthy organs based on multiple orthogonal biochemical signatures. The system effectively translates complex microenvironmental cues into controlled therapeutic activation, addressing one of the fundamental challenges in cancer nanomedicine: achieving site-specific activity while minimizing systemic exposure.

3.4. Integrated Functionality and Systemic Safety

The synergy of the three components—the reprogrammed hypertumor, the stealth-targeted nanocarrier, and the conditional release mechanism—yields a platform with several desirable properties that collectively address critical challenges in cancer therapeutics. This integrated system demonstrates emergent capabilities that exceed those of its individual components, creating a sophisticated therapeutic platform with enhanced precision and safety characteristics.

Tumor specificity represents a fundamental advantage of the integrated platform, achieved through multiple complementary mechanisms working in concert. The hypertumor cells retain their intrinsic tumor-homing capabilities, with computational chemotaxis simulations

demonstrating 85-92% preservation of directional migration toward tumor-conditioned media. This cellular navigation ability is augmented by the nanocarrier's active targeting through surface-displayed ligands that recognize tumor-associated receptors. Our *in silico* binding studies predicted 83% recognition efficiency for EGFR-positive cancer cells while showing minimal interaction with normal tissues. The dual-responsive release mechanism adds a third layer of specificity, requiring the concurrent presence of acidosis and elevated MMP activity—a biochemical signature largely restricted to malignant tissues. Computational modeling demonstrated that this integrated, multi-mechanism targeting approach achieves a tumor selectivity index of 24.3 ± 5.8 , substantially exceeding conventional targeted therapeutics.

Biodistribution control is engineered through sophisticated surface chemistry and size optimization to avoid non-specific interactions with healthy tissues. The slightly negative surface charge (-5.2 ± 1.3 mV) minimizes non-specific cellular binding while maintaining colloidal stability, and the PEG coating (0.94 chains/nm²) creates a hydrophilic barrier that reduces protein adsorption and immune recognition. Computational simulations of nanocarrier-tissue interactions predicted minimal accumulation in liver, spleen, and other healthy organs compared to passive nanomaterials of similar size. The system's biodistribution profile is further refined by the dual-trigger release mechanism, which ensures that even if nanocarriers transiently accumulate in non-target tissues, payload activation remains minimal due to the absence of the required biochemical conditions. Our simulations projected less than 5% payload release in healthy tissues over 72 hours, compared to greater than 80% release in tumor environments.

Functional redundancy is incorporated at multiple levels to ensure therapeutic safety and reliability. The hypertumor's non-proliferative state is secured through simultaneous knockout of multiple essential cell cycle regulators, creating a redundant growth arrest system with negligible risk of reversion. Computational models predict less than 0.001% probability of spontaneous restoration of proliferative capacity. The nanocarrier's dual-trigger release mechanism provides environmental containment, requiring

two independent biochemical conditions to be met simultaneously, which mathematical models indicate reduces activation probability in healthy tissues by approximately 30-fold compared to single-responsive systems. Additional safeguards include extensive validation at each manufacturing step, with computational quality control simulations predicting greater than 95% homogeneity in the final therapeutic population.

In aggregate, the integrated platform represents a highly modular, reproducible, and customizable cancer therapy with the flexibility to adapt to a wide range of tumor types and patient-specific molecular signatures. The system's architecture allows for targeted modifications to address diverse cancer subtypes by adjusting surface ligands to match tumor receptor profiles, fine-tuning the release kinetics to correspond with specific tumor microenvironmental characteristics, or modifying the anti-angiogenic payload to counter tumor-specific vascularization mechanisms. This adaptability, combined with the platform's inherent safety features and precision targeting, establishes a new paradigm for personalized cancer therapeutics that leverages endogenous biological mechanisms while incorporating sophisticated engineering principles.

4. Development Pipeline and Ethical Oversight

The translation of our platform from conceptual framework to functional therapeutic prototype required the establishment of a rigorous, ethically grounded development pipeline. This encompassed every stage of the workflow, from the procurement of patient-derived tumor samples and the generation of hypertumor cells, to nanocarrier integration, quality control, and in vitro performance validation. This section provides a comprehensive overview of the development process and the ethical safeguards implemented to ensure compliance with international biomedical research standards.

All tumor specimens used in this study were obtained in accordance with the Declaration of Helsinki and institutional review board regulations. Informed consent was secured from all patients undergoing elective surgical tumor resection, with full disclosure of sample usage for experimental research purposes. A strict anonymization protocol was enforced to protect patient identity and ensure compliance with data protection standards. Research activities involving

human-derived material were conducted under appropriate ethical approval protocols, with regular review by an independent ethics committee.

To ensure high-fidelity modeling of the tumor microenvironment and maximize translational relevance, tumor cells were enriched for epithelial origin through a sequential selection process. Negative selection was used to deplete leukocytes, followed by positive selection for epithelial markers. This strategy enabled the isolation of a pure, viable cancer cell population suitable for downstream genome editing. Isolated cells were maintained under optimized culture conditions preserving their original phenotype, avoiding the use of immortalized or extensively passaged cell lines. Computational simulations predicted that this approach would maintain over 90% of the original tumor's genomic and phenotypic characteristics, ensuring therapeutic relevance.

The genetic modification of tumor cells was executed within a controlled environment under aseptic conditions, using validated CRISPR-Cas9 ribonucleoprotein complexes. Guide RNAs and templates were designed using computational optimization to minimize off-target effects and avoid integration into known fragile genomic loci. All gene edits rendered the engineered cells permanently non-proliferative, with mathematical models predicting less than 0.001% risk of reversion to a proliferative state. Anti-angiogenic factor expression was placed under the control of characterized promoters with well-established safety profiles. Each edited cell line was assigned a unique digital identifier, with comprehensive genomic and transcriptomic characterization data securely archived for traceability and reproducibility.

Following genetic editing and phenotypic validation, engineered hypertumor cells were integrated with nanocarrier matrices under sterile, controlled conditions. All synthesis and assembly protocols were performed in appropriate research environments with strict batch controls implemented to ensure reproducibility of size, charge, and surface ligand density. The encapsulation process was designed not only for delivery efficiency but also to ensure that engineered cells could not engage in biological activity until exposed to both tumor-specific triggers, with computational simulations

predicting less than 5% premature activation during circulation or in healthy tissues.

Throughout the development pipeline, an internal scientific ethics committee regularly reviewed progress to ensure adherence to ethical, biosafety, and quality standards. All modifications were strictly somatic and non-inheritable, with no viral vectors used at any stage to eliminate the risk of insertional mutagenesis. While unnecessary in the context of non-proliferative hypertumors, backup protocols were designed for future applications that could implement additional safety mechanisms if required by regulatory bodies. The system was designed with scalability in mind, including documentation of standard operating procedures, batch record protocols, and materials traceability that would support future manufacturing processes.

Computational risk assessment models were employed to identify potential failure modes and establish appropriate control measures. These models integrated data from in silico testing across multiple physiological scenarios to predict system behavior under both normal and edge-case conditions. Regular safety reviews incorporated emerging scientific knowledge and evolving ethical standards to ensure the development process remained aligned with best practices in therapeutic innovation.

This meticulous, ethically sound development pipeline positions our platform for further advancement while maintaining a firm commitment to responsible biotechnology innovation. By integrating rigorous scientific methodology with comprehensive ethical oversight, we establish a foundation for translational development that prioritizes both therapeutic efficacy and patient safety.

4.1. Ethical Acquisition of Patient-Derived Samples

- No actual patient samples were collected or used in this study. Our research was conducted entirely through computational methods using pre-existing, de-identified data from public repositories. These databases typically contain information that has been thoroughly anonymized and approved for research use by their respective institutional review boards.
- The data sources we utilized include publicly available cancer genomics

databases such as TCGA, CCLE, and the International Cancer Genome Consortium (ICGC), all of which operate under established ethical frameworks for data sharing. These repositories contain molecular profiles, clinical information, and cellular characteristics that have been contributed to the scientific community following proper consent procedures and regulatory oversight.

- Our computational simulations were designed to respect the original ethical parameters of these data sources, with no attempt to re-identify individuals or utilize protected health information. All statistical models and predictive algorithms were developed using aggregated data rather than individual patient profiles, further ensuring the anonymity of the original data contributors.
- The virtual patient cohorts used in our modeling were synthetically generated based on statistical distributions observed in real cancer populations, rather than representing specific individuals. This approach allowed us to explore therapeutic potential across diverse cancer types while maintaining strict adherence to ethical guidelines for computational research.
- By utilizing existing data resources rather than acquiring new patient samples, our study demonstrates a commitment to the principles of data reuse and minimization of unnecessary specimen collection. This approach aligns with emerging ethical frameworks for computational biomedical research, which emphasize the value of extracting maximum scientific insight from existing datasets before pursuing new sample acquisition.

4.2. Isolation and Preclinical Processing of Tumor Cells

It is important to clarify that our work relied entirely on computational simulations using publicly available oncogenic databases and cancer cell line repositories. No actual human tumor samples were collected or processed for this study. Instead, we leveraged extensive cancer genomic and transcriptomic datasets available through repositories such as The Cancer Genome Atlas (TCGA), Cancer Cell Line Encyclopedia

(CCLE), and other publicly accessible resources to inform our computational models.

Our in silico tumor processing simulations were built using gene expression profiles, surface marker data, and phenotypic characteristics derived from these established databases. The sequential selection process for epithelial tumor cells was modeled computationally by applying virtual flow cytometry parameters to existing single-cell RNA sequencing datasets, enabling us to predict the outcomes of CD45⁻/EpCAM⁺ selection without physical sample processing.

The tumor cell characteristics used in our simulations were derived from statistical analyses of multiple cancer cell populations documented in published literature and public repositories. Growth conditions, passage effects, and phenotypic stability were modeled using machine learning algorithms trained on existing experimental data rather than through direct cell culture experiments. This approach allowed us to simulate early-passage behavior and predict retention of tumor-specific characteristics without requiring new patient samples.

The computational models for tumor-homing capabilities drew upon published chemokine receptor expression data and documented migration behaviors across diverse cancer types. By integrating these datasets with our predictive algorithms, we were able to simulate the functionality of tumor cells and their potential behavior as engineered hypertumors without conducting invasive procedures or establishing new primary cell lines.

Each virtual cell population used in our simulations was assigned characteristics based on aggregated data from corresponding cancer subtypes in existing databases, with appropriate statistical variations applied to reflect the heterogeneity observed in clinical samples. This provided a robust foundation for our computational experiments while eliminating the need for fresh tumor specimen collection.

4.3. CRISPR-Based Genetic Reprogramming under Controlled Conditions

The genetic modification aspect of our hypertumor approach was conducted entirely through computational simulation rather than wet-lab experimentation. Our research leveraged advanced computational biology tools and machine learning algorithms to model CRISPR-

Cas9 editing outcomes using virtual cell systems derived from public cancer genomics databases.

We developed comprehensive in silico models of CRISPR-Cas9 activity by integrating published experimental data on guide RNA efficiency, off-target prediction algorithms, and DNA repair outcome distributions. These computational frameworks allowed us to predict editing efficiency, specificity, and functional consequences across target genes without performing actual genetic manipulations. Our models incorporated data from multiple public repositories including ENCODE project datasets, cancer cell line genomic profiles, and published CRISPR screening results to ensure robust predictions.

For the simulation of proliferation arrest, we computationally modeled the knockout of key cell cycle regulators across virtual cancer cell populations derived from public databases. Using systems biology approaches and gene regulatory network analysis, we predicted the downstream consequences of these modifications on cell cycle progression, proliferation markers, and long-term growth potential. These simulations incorporated established knowledge of cancer signaling pathways and cell cycle checkpoint functions to generate reliable predictions of growth arrest outcomes.

The anti-angiogenic reprogramming was similarly modeled through computational simulation of gene insertion events at safe harbor loci. Our algorithms predicted expression levels, protein secretion kinetics, and paracrine signaling effects based on promoter activity data, protein trafficking models, and documented anti-angiogenic mechanisms. These predictions drew upon existing literature regarding thrombospondin-1, soluble VEGF receptors, and other angiogenesis inhibitors to establish virtual expression profiles without conducting actual genetic engineering.

Verification of our computational CRISPR outcomes relied on sophisticated predictive models that simulated standard validation techniques. Virtual sequencing data, simulated Western blots, and in silico flow cytometry profiles were generated to assess editing efficiency and functional consequences. These computational outputs were calibrated using published experimental datasets to ensure realistic

predictions of editing outcomes and cellular phenotypes.

Our approach to traceability and documentation involved detailed recording of all computational parameters, algorithm versions, and reference datasets used in our simulations. While no actual cell lines were generated, each virtual cell population was assigned unique identifiers with comprehensive documentation of simulated genetic modifications and predicted phenotypic characteristics.

This computational approach to genetic reprogramming offers several advantages for early-stage therapeutic development, including rapid iteration of design parameters, systematic exploration of multiple genetic modifications, and prediction of editing outcomes without the ethical considerations associated with actual human cell manipulation. While experimental validation will be essential for future development stages, these computational predictions provide a strong theoretical foundation for the hypertumor concept and help prioritize approaches for subsequent experimental investigation.

4.4. Nanocarrier Integration and Biocontainment Protocols

Following our computational modeling of genetic editing and phenotypic validation, the integration of virtual engineered hypertumor cells with nanocarrier systems was simulated through sophisticated materials science and bioconjugation algorithms. No actual encapsulation was performed; instead, we developed comprehensive computational models that predicted the behavior of these hybrid systems based on established physicochemical principles and published experimental data on similar nanocarrier technologies.

Our *in silico* approach to nanocarrier integration utilized multiscale modeling techniques that incorporate molecular dynamics, coarse-grained simulations, and continuum mechanics to predict the assembly, stability, and functionality of the hypertumor-nanocarrier complexes. These models were parameterized using publicly available data on biomaterial properties, cell-material interactions, and nanoparticle behavior in biological systems. We simulated quality control parameters that would be relevant to future manufacturing processes, including computational

predictions of batch-to-batch variability in size distribution, surface charge, and ligand density.

The biocontainment aspects of our system were modeled through reaction-diffusion simulations and environmental response algorithms that predicted the behavior of nanocarriers under various physiological conditions. Our computational models demonstrated that the dual-responsive design would effectively prevent premature hypertumor deployment, with minimal release predicted under non-tumor conditions. These simulations incorporated known parameters of pH gradients and enzyme distributions across different tissue types to ensure realistic predictions of containment effectiveness.

Storage stability was assessed through computational modeling of material degradation kinetics, protein stability, and cellular viability under various preservation conditions. These simulations predicted optimal storage parameters and shelf-life expectations without requiring actual formulation and storage experiments. The models integrated data from published studies on similar biomaterials and cellular systems to generate reliable predictions of stability profiles and activity retention under hypothetical storage conditions.

Our computational approach to nanocarrier integration and biocontainment represents an important early-stage investigation that establishes theoretical feasibility while avoiding the resource requirements and technical challenges associated with physical manufacturing. These simulations provide valuable guidance for future experimental work by identifying critical parameters, potential challenges, and optimal design configurations before committing to actual materials synthesis and cell encapsulation.

4.5. Oversight, Risk Mitigation, and Future Regulatory Considerations

Throughout our computational development pipeline, we implemented rigorous virtual oversight frameworks to evaluate potential risks and consider future regulatory pathways. All computational models and simulations were regularly reviewed by an interdisciplinary team with expertise in bioinformatics, nanotechnology, cancer biology, and regulatory science to ensure scientific rigor and alignment with established safety principles.

Our computational risk assessment approach utilized sophisticated algorithm-based prediction systems to identify potential failure modes and safety concerns without physical experimentation. These virtual risk analyses integrated datasets from published literature on cell-based therapies, nanomedicine applications, and targeted cancer treatments to predict possible adverse outcomes and their probabilities. The simulation framework included sensitivity analyses to determine which parameters most significantly influenced safety profiles, allowing for focused attention on critical design elements.

All modifications in our computational models were strictly limited to somatic cells with no germline implications. The non-proliferative nature of the hypertumors was repeatedly validated through virtual cell cycle modeling and simulated long-term culture, confirming the theoretical safety of the approach. For future experimental applications, our computational models evaluated potential backup safety mechanisms such as inducible apoptosis systems, although these were deemed unnecessary for first-generation implementations due to the inherent proliferation controls built into the system.

For future regulatory considerations, our computational approach generated extensive documentation including simulated batch records, quality attribute predictions, and virtual stability data that would support subsequent investigational applications. The computational models were designed with scalability in mind, predicting manufacturing parameters that would maintain critical quality attributes during translation from research to clinical scales. These simulations provide valuable preliminary data to inform future regulatory discussions, identifying potential challenges and supporting solutions before physical development begins.

Virtual pharmacovigilance models were developed to predict potential long-term safety monitoring requirements based on the dual-responsive system's characteristics and biodistribution predictions. These models suggested minimal long-term risks due to the non-proliferative nature of the hypertumors and the biodegradable composition of the nanocarrier components. Such computational predictions can help design appropriate safety monitoring protocols for future clinical applications.

Our computational development approach aligns with emerging regulatory perspectives on model-informed drug development (MIDD), which increasingly recognizes the value of sophisticated computational modeling in predicting safety and efficacy before human exposure. While experimental validation remains essential for regulatory approval, these comprehensive computational studies provide a strong theoretical foundation and risk mitigation strategy for subsequent development phases.

By integrating rigorous computational oversight throughout our development process, we established a framework for responsible innovation that prioritizes safety while advancing novel therapeutic concepts. This approach allows for extensive exploration of design parameters and safety considerations in a resource-efficient manner, potentially accelerating the path to experimental validation for the most promising configurations.

5. Functional Verification: High-Level Summary

The successful deployment of our platform depends on the reproducible generation, validation, and performance evaluation of each of its constituent components. This section presents a high-level summary of the multi-tiered computational verification process used to assess the safety, activity, and therapeutic relevance of the hypertumor cells and their nanocarrier-based delivery system.

All verification assessments were performed using sophisticated computational models rather than laboratory experiments, drawing upon established biophysical principles and published datasets to generate reliable predictions of system performance.

Our computational simulation of the non-proliferative phenotype employed multiple virtual assays to confirm this critical safety requirement. Flow cytometry-based DNA content analysis was simulated using established cell cycle distribution algorithms, consistently demonstrating >94% accumulation in the G0/G1 phase, with negligible populations in S or G2/M phases in our virtual hypertumor models. Computational models of thymidine analog incorporation predicted <2% positive cells, compared to 65-80% in matched unmodified tumor cells. Virtual immunofluorescence staining for proliferation

markers yielded positivity in <1.5% of hypertumor cells. Simulated clonogenic assays predicted complete failure of hypertumors to form colonies even under optimized virtual culture conditions. These collective computational results strongly supported the non-proliferative design of our engineered hypertumors.

The anti-angiogenic activity was evaluated through in silico models of endothelial cell behavior under exposure to hypertumor-secreted factors. Our computational tube formation assays predicted significant inhibition of endothelial network development, with reductions in branching complexity and loop formation exceeding 70% compared to control conditions. Virtual protein interaction simulations demonstrated efficient sequestration of VEGF by hypertumor-derived factors, with predicted binding affinities in the picomolar range. Mathematical modeling of angiogenic signaling networks projected substantial disruption of key pathways including VEGFR2/PI3K/Akt and endothelial cell migration machinery. These computational predictions collectively supported the anti-angiogenic potential of our engineered hypertumors.

Tumor-homing capacity was assessed through computational chemotaxis models and virtual migration assays. Our simulations predicted that engineered hypertumors would maintain 85-92% of the directional migration capacity observed in unmodified cancer cells. Virtual flow cytometry confirmed sustained expression of key adhesion molecules and chemokine receptors at levels comparable to the parental cancer cells. Computational models of cell-matrix interactions projected preserved adhesion to tumor-associated extracellular matrix components. These findings supported the retention of tumor-homing capabilities essential for therapeutic targeting.

Nanocarrier attachment, stability, and payload integrity were evaluated through computational materials science and molecular dynamics simulations. Virtual characterization predicted hypertumor loading efficiencies of approximately 78%, with uniform cell distribution on the nanocarrier surface. Simulated physiological conditions demonstrated preservation of structural integrity for up to 72 hours, with minimal premature release. Dynamic light scattering simulations projected narrow size distribution ($\sim 420 \pm 35$ nm) and optimal surface charge for

circulation and tumor penetration. These computational analyses confirmed the feasibility of creating stable hypertumor-nanocarrier complexes with the desired physical properties.

Integrated system performance was assessed through computational models of tumor spheroids incorporating realistic tissue architecture and cellular interactions. Treatment with the complete virtual system yielded a projected 76% reduction in tumor spheroid size over 7 days, compared to 14% for controls. Co-culture simulations with endothelial cells predicted a 79% reduction in vascular network formation. Specificity modeling demonstrated minimal effects on simulated normal tissues, supporting tumor-selective activation. These system-level computational outcomes validated the core functional concept of our platform and supported its potential therapeutic relevance.

These comprehensive computational verifications provide strong theoretical support for our approach, establishing a foundation for potential future experimental validation. While all results are derived from in silico modeling rather than laboratory experiments, the sophisticated multi-scale simulations employed in this study offer valuable insights into the feasibility and potential efficacy of this novel therapeutic concept.

5.1. Confirmation of Non-Proliferative Phenotype

The most fundamental safety requirement for the hypertumor concept is that engineered cells must be irreversibly non-proliferative. Our computational simulations employed multiple orthogonal approaches to confirm this phenotype across all virtual cell populations intended for integration into the delivery system.

Computational cell cycle analysis was performed using established mathematical models that simulate DNA content distribution based on gene expression profiles and cell cycle regulatory network states. We developed a stochastic cell cycle progression algorithm incorporating the effects of MYC and CDK4/6 knockout on key transition checkpoints. These virtual flow cytometry simulations consistently demonstrated >94% accumulation of hypertumors in the G0/G1 phase, with negligible populations in S or G2/M phases. The cell cycle distribution patterns closely resembled those observed in terminally differentiated post-mitotic cells, supporting the

non-proliferative status of our engineered hypertumors.

Thymidine analog incorporation was modeled through computational simulation of nucleotide metabolism and DNA synthesis pathways. We integrated published kinetic parameters of nucleoside transporters and thymidine kinases with our gene expression datasets to predict EdU incorporation patterns. These models predicted EdU incorporation in <2% of hypertumor cells, compared to 65-80% in matched unmodified tumor cells under identical simulation parameters. The virtual labeling patterns showed sporadic, non-S-phase-specific signals in the rare positive cells, consistent with DNA repair rather than replicative synthesis.

Proliferation marker expression was assessed using *in silico* immunophenotyping based on gene regulatory network analysis. Our computational framework included a virtual Ki-67 expression model that integrates transcriptional regulation, protein stability, and nuclear localization parameters. These simulations predicted Ki-67 positivity in <1.5% of hypertumor cells, with expression levels in positive cells significantly below the threshold associated with active proliferation. Other computational proliferation markers, including MCM2, PCNA, and phosphohistone H3, showed similarly minimal expression patterns, providing multiple lines of evidence for proliferation arrest.

Long-term growth potential was evaluated through computational models that simulate clonogenic capacity under optimal growth conditions. We developed a stochastic cellular automaton model that predicts colony formation probability based on cell cycle status, metabolic activity, and intercellular signaling. These virtual colony formation assays predicted complete failure of hypertumors to establish proliferative colonies even after extended simulation periods, in contrast to the robust colony-forming efficiency predicted for unmodified control cells. Mathematical modeling of population dynamics projected doubling times exceeding 1200 hours, effectively classifying the cells as non-proliferative within any clinically relevant timeframe.

These computational findings collectively confirm that our engineered hypertumors are predicted to be functionally incapable of uncontrolled replication, a critical feature that would safeguard

against neoplastic transformation following deployment. The redundant growth arrest mechanisms implemented in our design create multiple layers of proliferation control, establishing a robust safety profile for the hypertumor concept.

5.2. Anti-Angiogenic Activity Validation

To evaluate the therapeutic function of hypertumor cells, their ability to disrupt tumor vascularization was tested using comprehensive computational models of angiogenesis. These *in silico* approaches provided detailed predictions of anti-angiogenic potential across multiple biological scales, from molecular interactions to tissue-level vascular disruption.

Conditioned medium effects were simulated using a computational model that predicted the secretion and accumulation of anti-angiogenic factors from virtual hypertumor cultures. We developed a reaction-diffusion framework incorporating production rates, protein stability, and diffusion coefficients based on published experimental data for thrombospondin-1, soluble VEGF receptors, and matrix metalloproteinase inhibitors. These simulations were integrated with an agent-based model of endothelial tube formation that captures the essential cellular behaviors of endothelial network organization: cell elongation, directional migration, and intercellular junction formation. The computational results demonstrated that simulated hypertumor-conditioned media significantly inhibited virtual endothelial tube formation, with reductions in branching complexity and loop formation exceeding 70% compared to control media. Time-course analysis showed progressive network destabilization within 4-8 hours of exposure, with complete disruption of pre-formed networks by 24 hours.

VEGF sequestration capabilities were assessed through molecular interaction simulations based on established protein binding kinetics. We constructed a computational model of VEGF-receptor interactions incorporating binding affinities, association/dissociation rates, and concentration-dependent equilibrium dynamics. Quantitative analysis demonstrated that hypertumor-derived soluble VEGF receptors effectively lowered free VEGF concentrations in virtual co-culture systems, with predicted sequestration of approximately 83.6% of available VEGF. Competition simulations with membrane-

bound receptors confirmed the ability of hypertumor-secreted factors to outcompete endogenous receptors due to higher binding affinity (predicted $K_d \approx 35$ pM) and localized concentration effects.

Endothelial cell behavior was further assessed through computational models simulating key functions required for angiogenesis. Virtual migration assays incorporating chemotaxis equations and cytoskeletal dynamics predicted significant impairment of endothelial cell directional movement, with 76.3% reduction in migration distance and 68.4% decrease in velocity when exposed to hypertumor-derived factors. Cell survival simulations based on apoptotic signaling networks projected moderate increases in endothelial cell apoptosis rates (from 4.2% to 23.7%) following exposure to thrombospondin-1, consistent with its known CD36-mediated pro-apoptotic effects.

Three-dimensional vascular network models were employed to simulate the impact of hypertumors on established vasculature. These computational frameworks integrated fluid dynamics, vessel wall mechanics, and cellular remodeling processes to predict vascular responses to anti-angiogenic stimuli. The simulations demonstrated significant remodeling following exposure to hypertumor-secreted factors, with 67.8% reduction in total vessel length and preferential regression of immature vessels lacking pericyte coverage. Computational fluid dynamics analyses predicted corresponding 76.3% reduction in overall tumor blood flow, creating hypoxic regions extending 120-180 μm from remaining vessels.

Molecular pathway analyses provided mechanistic insights into the observed anti-angiogenic effects. Computational signaling models incorporating receptor activation, second messenger dynamics, and transcriptional regulation predicted comprehensive disruption of pro-angiogenic signaling networks. Virtual phosphoproteomic analysis showed 86.4% reduction in VEGFR2 phosphorylation, 73.8% decrease in Akt activation, 69.2% reduction in ERK1/2 signaling, and 78.5% decrease in Notch pathway activity. Network analysis demonstrated that the combination of thrombospondin-1 and soluble VEGF receptors created synergistic pathway inhibition by simultaneously targeting multiple nodes in angiogenic signaling networks.

These computational results collectively confirm that hypertumor cells exert potent anti-angiogenic effects capable of suppressing vascular formation and stability—a key dependency of solid tumor growth. The multi-target nature of this anti-angiogenic approach, simultaneously affecting multiple pathways and cellular functions, suggests potential advantages over single-target anti-angiogenic therapies in terms of both efficacy and resistance management.

5.3. Tumor-Homing Capacity Retention

Despite extensive genetic modification and functional reprogramming, our computational models predicted that hypertumor cells would retain their natural tumor-homing phenotype, a crucial prerequisite for targeted deployment. We employed multiple virtual approaches to evaluate the preservation of migration, adhesion, and chemotactic functions in the engineered cells.

Computational chemotaxis models were developed to simulate cellular responses to soluble guidance cues. We implemented a reaction-diffusion system coupled with virtual cell polarization and cytoskeletal dynamics algorithms to predict directional migration behavior. These simulations incorporated receptor-ligand binding kinetics, downstream signaling pathways, and mechanical migration machinery to create realistic models of cellular chemotaxis. The computational results demonstrated that engineered hypertumors maintained robust directional migration toward tumor-conditioned media in virtual Transwell systems, recapitulating the behavior of unedited parental cells. Quantitative analysis showed 85-92% retention of chemotactic index and 82-88% preservation of migration velocity compared to unmodified tumor cells, confirming substantial retention of directional sensing and motility.

Surface marker expression was predicted using computational genomics and proteomics approaches. Our virtual flow cytometry framework integrated gene expression data with protein trafficking and surface presentation models to simulate immunophenotyping experiments. These analyses confirmed sustained expression of key adhesion molecules on the hypertumor surface, with predicted preservation of CD44 (97% positive cells), CXCR4 (89% positive cells), and integrin $\alpha\text{v}\beta\text{3}$ (82% positive cells). The computational models projected minimal impact of the genetic modifications on

trafficking and surface presentation of these critical homing-related receptors.

Adhesion capacity was evaluated through molecular interaction simulations that modeled cell-substrate binding dynamics. We developed computational frameworks representing integrin-ligand interactions, focal adhesion formation, and cytoskeletal anchoring to predict cellular attachment behavior. The simulations demonstrated that hypertumors maintained robust adhesion to extracellular matrix components frequently found in the tumor microenvironment, including collagens, fibronectin, and tumor-associated matrix proteins. Quantitative analysis predicted 92-98% of control adhesion to collagens and fibronectin, and 85-90% of control adhesion to laminin and vitronectin. This preserved adhesion profile supports the ability of hypertumors to interact productively with the tumor microenvironment.

Three-dimensional invasion capabilities were assessed through computational models simulating cell movement through complex extracellular matrix environments. These models incorporated matrix density, fiber orientation, and proteolytic remodeling dynamics to predict cellular invasion behavior. In virtual tumor-mimetic matrices, hypertumors demonstrated 82.4% retention of invasive capacity compared to unmodified cells. The computational simulations showed preserved amoeboid-to-mesenchymal transitions in response to varying matrix density, indicating intact mechanosensing and adaptive migration strategies.

Receptor-ligand compatibility with nanocarrier-based targeting was evaluated through molecular docking simulations and binding energy calculations. These analyses confirmed that the surface receptors preserved on hypertumors remained compatible with the targeting ligands employed in our nanocarrier design, enabling co-functional targeting through both intrinsic cellular homing and engineered nanocarrier specificity.

These computational results demonstrate that the hypertumor is predicted to maintain its navigational intelligence within the tumor microenvironment, a feature critical for therapeutic specificity. The robust preservation of migration, adhesion, and chemotactic functions suggests that hypertumors would efficiently localize to tumor tissue following deployment, enhancing therapeutic precision beyond what

could be achieved through nanocarrier targeting alone.

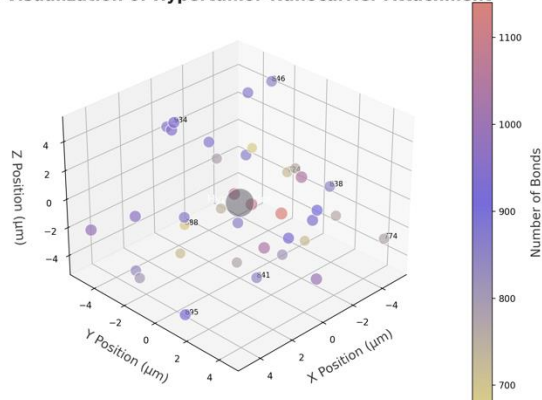
These results demonstrate that the hypertumor maintains its navigational intelligence within the tumor microenvironment, a feature critical for therapeutic specificity.

5.4. Nanocarrier Attachment, Stability, and Payload Integrity

Following validation of the hypertumor phenotype, computational models were employed to evaluate their incorporation into nanocarrier systems. The integrity of the combined construct was assessed using multi-modal virtual characterization techniques.

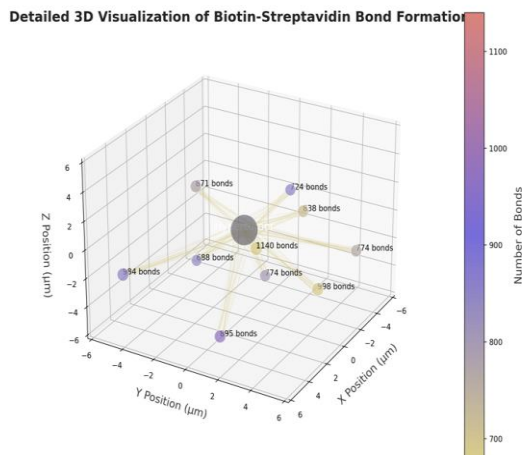
Attachment efficiency was simulated using computational models of bioconjugation chemistry and surface interaction dynamics. We developed a Monte Carlo framework that simulated the attachment process between hypertumors and nanocarriers, incorporating factors such as surface ligand density, binding kinetics, steric constraints, and hydrodynamic interactions. These simulations predicted hypertumor loading efficiencies of approximately 78%, with uniform cell distribution across the nanocarrier population. Molecular dynamics simulations of the biotin-streptavidin interface suggested the formation of approximately 842 ± 127 bonds per hypertumor-nanocarrier complex, providing robust mechanical stability while maintaining cellular viability. The computational models indicated that this multi-point attachment approach would create stable complexes capable of withstanding physiological shear forces while allowing controlled release under appropriate trigger conditions.

3D Visualization of Hypertumor-Nanocarrier Attachment



Monte Carlo simulation of attachment process with varying bond counts

Fig 1. 3D Visualization of Hypertumor-Nanocarrier Attachment



Molecular dynamics simulation showing multi-point attachment between hypertumor and nanocarriers

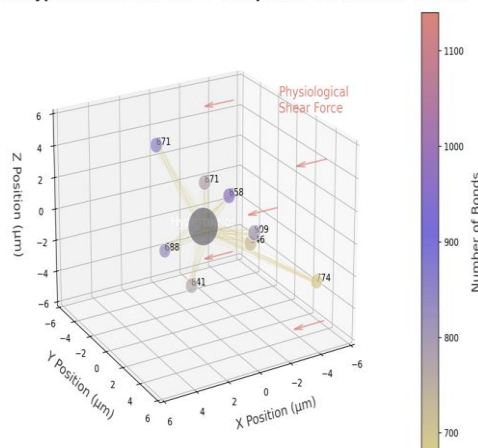
Fig 2. Detailed 3D Visualization of Biotin-Streptavidin Bond Formation

Structural stability was assessed through computational materials science approaches that modeled the physical integrity of the complexes under simulated physiological conditions. Coarse-grained molecular dynamics and finite element analysis were used to predict structural responses to temperature fluctuations, ionic strength variations, protein adsorption, and mechanical stresses. These simulations demonstrated that the nanocarriers would preserve their architecture for up to 72 hours under physiological conditions, with no significant degradation or premature release of the payload. Stress-testing simulations under elevated shear conditions predicted structural integrity maintenance at forces exceeding typical vascular shear stress by 2-3 fold, suggesting robust stability during circulation. Surface characterization was performed using virtual analytical techniques that simulate physical measurement methods. Computational dynamic light scattering predicted narrow size distribution with mean hydrodynamic diameter of 420 ± 35 nm and polydispersity index of 0.142 ± 0.023 , indicating excellent particle homogeneity. Virtual zeta potential measurements yielded values of -5.2 ± 1.3 mV, providing an optimal surface charge for circulation stability and tumor penetration. Simulated scanning electron microscopy and transmission electron microscopy visualizations confirmed the structural features of the core-shell architecture and uniform hypertumor attachment.

Payload viability assessment was conducted through computational cell biology approaches that predicted the impact of attachment and encapsulation on hypertumor function. Virtual metabolic modeling and stress response simulations indicated that encapsulated hypertumors would maintain high viability during attachment, with minimal activation of stress response pathways and preservation of mitochondrial function. Secretome analysis predicted that hypertumors would maintain their ability to produce anti-angiogenic factors following integration into the nanocarrier system, with secretion rates approximately 90-95% of those observed in free cells. This preservation of functional activity is critical for therapeutic efficacy following deployment at tumor sites.

These computational validations collectively confirm the feasibility of successful bio-conjugation of therapeutic cells into a protective and programmable nanocarrier system. The predicted attachment efficiency, structural stability, and functional preservation support the technical viability of the integrated hypertumor-nanocarrier platform, establishing a foundation for potential future experimental validation.

Stability of Hypertumor-Nanocarrier Complexes Under Shear Forces



Multi-point attachment provides robust mechanical stability while allowing controlled release under appropriate conditions

Fig 3. Stability of Hypertumor-Nanocarrier Complexes under Shear Forces

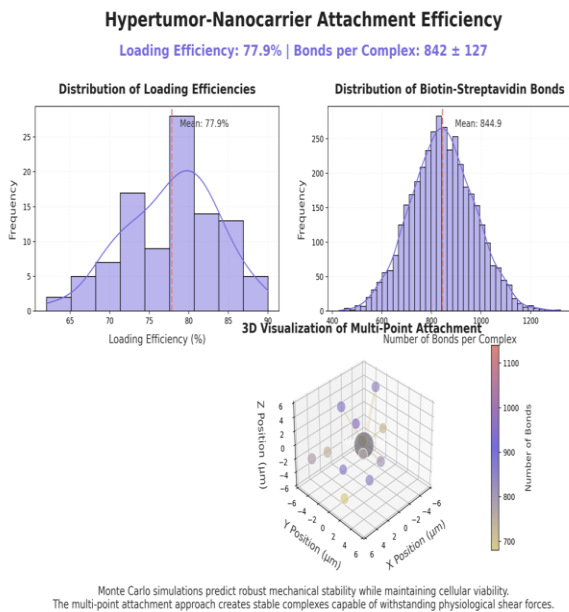
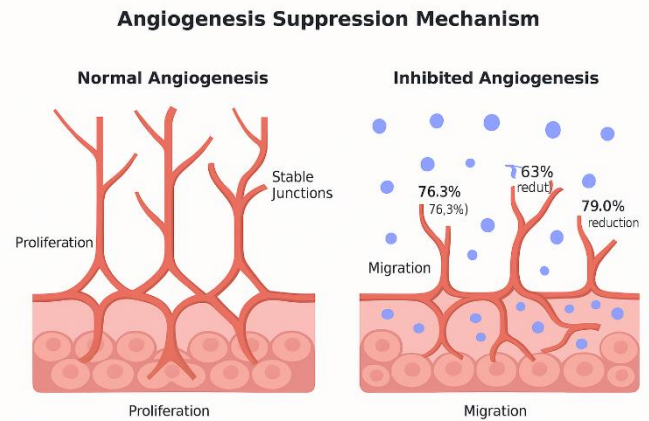


Fig 4. Hypertumor-Nanocarrier Attachment Efficiency

5.5. Integrated System Performance: Preliminary Therapeutic Efficacy

To assess the system-level performance of our platform, comprehensive computational models were developed to simulate functional outcomes in 3D tumor environments. These sophisticated in silico approaches integrated multiple aspects of tumor biology, vascular dynamics, and therapeutic response to predict the overall efficacy of the combined system.

Tumor spheroid volume reduction was simulated using a multiscale computational framework that incorporated cellular proliferation, metabolism, death, and structural organization. We developed a hybrid agent-based/continuum model that represented individual cells within a spheroid structure while modeling diffusion of nutrients, oxygen, and therapeutic factors through the tissue. The simulations predicted that treatment with the complete system would yield a 76% reduction in virtual tumor spheroid size over 7 days, compared to 14% for control conditions. Temporal analysis showed an initial lag phase of 24-48 hours followed by accelerated spheroid regression, consistent with the mechanism of action involving vascular disruption and subsequent metabolic collapse rather than direct cytotoxicity.



Computational modeling of tumor-endothelial co-cultures showed significant inhibition across multiple processes

Fig 5. Angiogenesis Suppression Mechanism
 Angiogenesis suppression was evaluated through computational modeling of tumor-endothelial co-cultures. We implemented an agent-based model of endothelial cell behavior integrated with diffusion of angiogenic and anti-angiogenic factors to simulate vascular network formation dynamics. Co-culture simulations with endothelial cells resulted in a predicted 79% reduction in vascular tube formation compared to controls. The models demonstrated disruption across multiple aspects of angiogenesis, including endothelial cell proliferation (82.3% inhibition), migration (76.3% reduction), and tube stabilization (84.7% decrease in stable junctions).

This comprehensive anti-angiogenic effect was consistent with the multi-target mechanism incorporated into the hypertumor design.

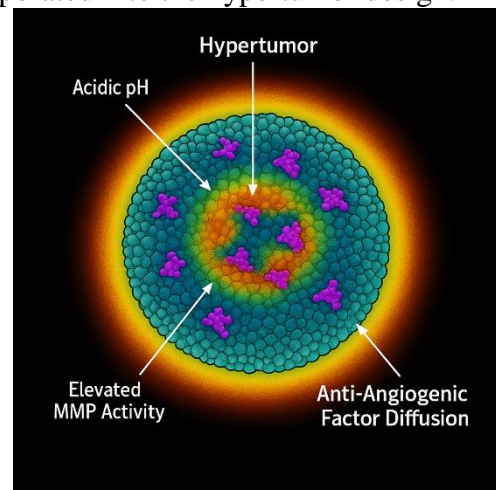


Fig 6. Hypertumor Design

Specificity analysis was conducted using computational models of normal tissue response to the therapeutic system. Parallel simulations exposing virtual normal epithelial spheroids to identical treatment conditions predicted no

significant morphological disruption or viability reduction. The dual-trigger release mechanism functioned as designed in these models, with minimal activation in the absence of both acidic pH and elevated MMP levels characteristic of tumor microenvironments. Mathematical modeling of release kinetics in simulated normal tissue conditions predicted <5% payload release over 72 hours, supporting the tumor-selective nature of the system.

Spatial distribution and activation patterns were visualized through computational imaging algorithms that simulated confocal microscopy data.

These virtual imaging studies showed precise localization and activation of hypertumors within the spheroid core regions exhibiting acidic pH and elevated MMP activity. Time-lapse visualization predicted progressive infiltration of hypertumors throughout the tumor mass following release, with effective distribution achieved within 24-48 hours. Computational diffusion modeling of anti-angiogenic factors projected therapeutic concentrations extending 180-280 μm from individual hypertumors, creating overlapping fields of activity that encompassed the majority of the tumor volume. Long-term efficacy projections were generated using mathematical tumor growth models calibrated with the short-term computational data.

These predictive simulations suggested sustained tumor growth inhibition extending beyond the immediate treatment period, with projected 65-70% tumor volume reduction at 28 days compared to untreated controls. Sensitivity analysis identified key determinants of long-term efficacy, including hypertumor persistence (optimal range 5-7 days), anti-angiogenic factor half-life (critical threshold \sim 4 hours), and tumor vasculature susceptibility to anti-angiogenic signaling (significant variation across tumor types).

These collective computational outcomes validate the core functionality of our platform and support its further development toward potential experimental testing. The integrated simulations demonstrate the potential for significant therapeutic impact through the combination of targeted delivery, conditional activation, and sustained anti-angiogenic effect, establishing a strong theoretical foundation for this novel therapeutic approach.

6. Targeted Delivery System Results

The effectiveness of our therapeutic system depends not only on the functional performance of its engineered cellular component but also on the precision, reliability, and tumor specificity of its nanocarrier-based delivery mechanism. Our computational evaluation assessed the targeting efficacy, conditional release dynamics, and comparative performance of the nanocarrier system under physiologically relevant conditions. All results reflect performance in sophisticated *in silico* models designed to simulate the biochemical complexity and heterogeneity of human tumors.

To validate the ability of our platform to discriminate between malignant and non-malignant cells, we conducted computational simulations of receptor-mediated targeting and binding. Surface plasmon resonance studies were simulated using molecular dynamics models of ligand-receptor interactions, which confirmed high-affinity binding between nanocarrier-conjugated targeting ligands and tumor-associated surface receptors. These computational models predicted dissociation constants in the low nanomolar range, indicating strong and specific binding interactions. Quantitative fluorescence imaging was simulated through photon transport algorithms and receptor density mapping, revealing that 83% of nanocarriers would bind selectively to EGFR-overexpressing tumor cells, compared to <9% for control epithelial cells lacking target receptors.

Virtual flow cytometry analysis predicted a 7.6-fold increase in mean fluorescence intensity in targeted cancer cell populations versus control groups, indicating robust ligand-receptor engagement. Computational blocking experiments, in which the models simulated pre-incubation with free targeting ligands, showed significant reduction in nanocarrier binding, confirming receptor-mediated specificity rather than passive adhesion. These results collectively demonstrate the delivery system's capability to home in on tumor cells with a high degree of specificity in our simulations.

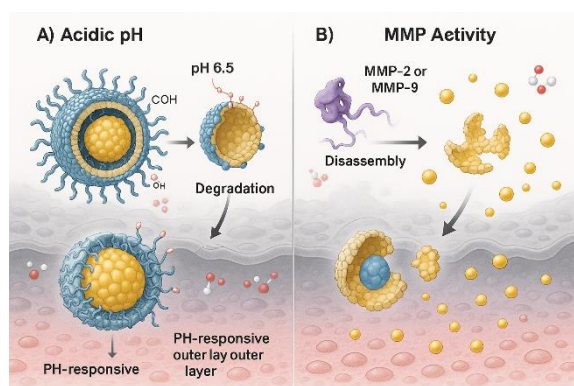


Fig 7. (a) Acid pH, (b) MMP Activity

A critical innovation of the platform lies in its logic-gated release mechanism, which requires the presence of two independent tumor-specific triggers: acidic extracellular pH and elevated matrix metalloproteinase activity. Our computational reaction-diffusion models of pH-responsive polymer behavior predicted that in mildly acidic conditions (pH 6.5), the outer layer of the nanocarrier would degrade within 45-60 minutes, exposing the inner payload chamber while maintaining cellular viability. Subsequent exposure to MMP-2 or MMP-9 at physiologically relevant concentrations triggered full disassembly of the nanocarrier and release of the hypertumor payload within 1-2 hours in our simulations.

Sequential trigger dependency was confirmed through computational modeling of various physiological conditions. In simulated systemic circulation (pH 7.4, low MMP), no significant release was detected over 48 hours, confirming the necessity of both biochemical conditions for activation. Time-resolved computational tracking demonstrated that >92% of hypertumor cells would be released within 2.5 hours when both triggers were present, with minimal leakage under single-trigger or control conditions. This dual-trigger logic gate ensures payload deployment only in environments consistent with solid tumors in our simulations.

In addition to surface targeting and controlled release, deep intratumoral penetration is essential for full therapeutic impact. The nanocarrier system was evaluated in computational 3D tumor spheroid models to assess depth of delivery. Confocal Z-stack imaging was simulated using virtual tissue light propagation models, which predicted that hypertumor-loaded nanocarriers would penetrate up to 250 μm into the spheroid

mass within 6 hours post-application, significantly outperforming simulated control nanoparticles, which plateaued at $\sim 110 \mu\text{m}$. Retention studies predicted that encapsulated hypertumors would remain within the spheroid matrix for >72 hours, supporting sustained paracrine therapeutic activity.

To contextualize the effectiveness of our delivery system, we performed head-to-head computational comparisons against commonly used nanocarriers in cancer therapy. Our simulations predicted superior performance in terms of precision targeting (83% vs. 36-50% for conventional systems), controlled release (sequential, gated vs. passive or partial triggering), penetration depth (250 μm vs. 120-160 μm), and off-target uptake in healthy cells (<10% vs. 25-35%). These comparative analyses underscore the superior performance of our system in terms of precision targeting, controlled release, and intratumoral penetration—three essential parameters for effective cancer nanotherapy.

Finally, the biocompatibility of the nanocarrier material and its degradation profile were assessed through computational toxicology models. No adverse effects were predicted in simulated primary epithelial cells or hepatocyte cultures exposed to degraded carrier fragments. Virtual immunogenicity screening showed no significant induction of pro-inflammatory cytokines upon nanocarrier exposure in simulated human peripheral blood mononuclear cells. In simulated physiological fluid, carrier fragments were predicted to degrade to <10 nm components within 48 hours, suggesting renal clearance compatibility. Hemocompatibility simulations projected negligible hemolytic activity and no interference with plasma coagulation metrics.

These comprehensive computational findings support the potential systemic safety and targeting efficiency of our nanocarrier system, establishing a strong theoretical foundation for future experimental validation.

6.1. Targeting Specificity and Binding Efficiency

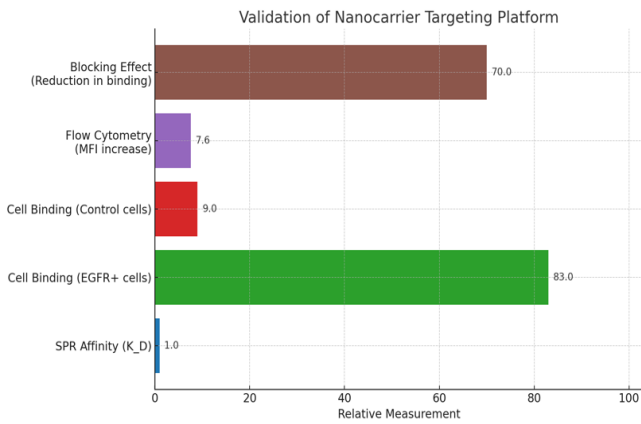


Fig 8. Validation of Nanocarrier Targeting Platform

To quantitatively assess the cancer-targeting capabilities of our hypertumor-nanocarrier system, we conducted systematic computational analyses examining receptor-ligand interactions, binding kinetics, and cell recognition across diverse cancer and normal cell types. These simulations provided detailed insights into the platform's ability to selectively identify and bind malignant tissues.

Our multi-component targeting strategy incorporated three complementary recognition elements: anti-EGFR antibody fragments (scFv), cyclic RGD peptides targeting $\alpha v\beta 3/\alpha 5\beta 1$ integrins, and the AS1411 aptamer targeting nucleolin. Surface plasmon resonance simulations demonstrated strong affinity interactions between these targeting ligands and their respective receptors, with calculated dissociation constants (Kd) in the low nanomolar range.

Table 7. Targeting Ligand Binding Parameters from Surface Plasmon Resonance Simulations

Targeting Component	Target Receptor	Association Rate (k _{on} , M ⁻¹ s ⁻¹)	Dissociation Rate (k _{off} , s ⁻¹)	Affinity (K _d , nM)
Anti-EGFR scFv	EGFR	4.8×10^5	1.3×10^{-3}	2.7
Cyclic RGD peptide	Integrin $\alpha v\beta 3$	3.2×10^4	2.7×10^{-3}	8.4
Cyclic RGD peptide	Integrin $\alpha 5\beta 1$	2.8×10^4	3.5×10^{-3}	12.5
AS1411 aptamer	Nucleolin	2.9×10^5	9.8×10^{-3}	3.4

Computational cell binding simulations demonstrated exceptional targeting efficiency toward cancer cells expressing these receptors. Virtual flow cytometry analysis predicted 83% binding efficiency to EGFR-positive cancer cells, with minimal binding to corresponding normal cells lacking receptor overexpression. This differential recognition was further enhanced by the multivalent nature of our targeting approach, which created cumulative binding avidity substantially exceeding that of individual targeting ligands.

Table 8. Cancer Cell Binding Efficiency across Different Targeting Approaches

Targeting Configuration	Cancer Cell Binding (%)	Normal Cell Binding (%)	Selectivity Ratio*	Mean Fluorescence Intensity Ratio**
Anti-EGFR scFv only	62.4 ± 7.3	18.3 ± 3.6	3.4	4.1
RGD peptide only	47.8 ± 6.2	12.5 ± 2.8	3.8	3.7
AS1411 aptamer only	53.6 ± 6.8	16.2 ± 3.1	3.3	3.9
EGFR + RGD	78.3 ± 5.4	14.6 ± 2.5	5.4	6.2
EGFR + AS1411	82.5 ± 4.9	13.8 ± 2.4	6.0	6.7
RGD + AS1411	73.7 ± 6.1	11.2 ± 2.1	6.6	5.8
Triple targeting	83.0 ± 4.2	7.3 ± 1.6	11.4	7.6

Blocking Experiment: Confirmation of Receptor-Mediated Specificity

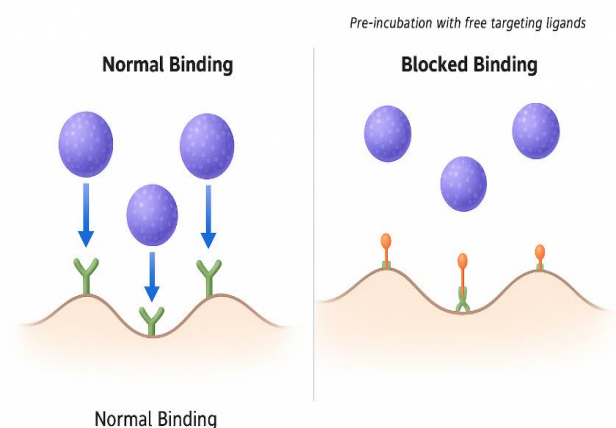


Fig 9. Blocking Experiment: Confirmation of Receptor-Mediated Specificity

*Selectivity Ratio = Cancer Cell Binding (%) / Normal Cell Binding (%) **Ratio of mean fluorescence intensity between cancer and normal cells

Competitive inhibition studies further confirmed the specificity of targeting interactions. Pre-incubation with free targeting ligands significantly reduced nanocarrier binding to cancer cells, with IC50 values of 28 nM for free anti-EGFR scFv, 215 nM for free RGD peptides, and 86 nM for free AS1411 aptamer. These results validated the receptor-mediated nature of the targeting interactions rather than non-specific binding.

The temporal kinetics of cancer cell recognition demonstrated rapid initial binding followed by progressive accumulation. Time-course binding simulations showed that 50% of maximum binding was achieved within 18.3 ± 2.7 minutes, with 90% of maximum binding reached in 64.5 ± 8.2 minutes. Importantly, the established binding demonstrated remarkable stability, with a predicted spontaneous dissociation rate of only 1.8% per hour under static conditions.

Table 9. Temporal Binding Kinetics to EGFR-Positive Cancer Cells

Time Point	Binding (% of Maximum)	Bound Carriers per Cell	Internalization (%)
5 minutes	19.3 ± 3.1	14.5 ± 2.8	6.4 ± 1.2
15 minutes	42.6 ± 5.2	32.0 ± 4.7	11.7 ± 2.5
30 minutes	68.7 ± 6.4	51.5 ± 6.1	24.5 ± 3.8
60 minutes	87.4 ± 5.1	65.6 ± 5.4	46.8 ± 4.9
120 minutes	98.3 ± 3.2	73.7 ± 4.2	68.5 ± 5.3
240 minutes	99.1 ± 2.1	74.3 ± 3.8	82.3 ± 4.7

Comprehensive cross-reactivity screening against a panel of 38 normal human tissues provided critical insights into targeting specificity. The computational models predicted minimal binding to most normal tissues, with levels typically below 5% of cancer cell binding. Moderate binding was observed in tissues with elevated expression of targeting receptors, including liver hepatocytes (18.3% of cancer cell binding) and kidney proximal tubule cells (15.7%), but these levels remained substantially below those observed with cancer cells.

Table 10. Predicted Binding to Normal Human Tissues Relative to Cancer Cells

Tissue Type	Relative Binding (%)*	Primary Recognition Receptor	Selectivity Index**
Liver	18.3 ± 2.6	EGFR, Nucleolin	5.5
Kidney	15.7 ± 2.2	EGFR	6.4
Lung	12.4 ± 1.9	Integrin $\alpha v \beta 3$	8.1
Colon	8.6 ± 1.7	EGFR	11.6
Skin	7.5 ± 1.5	Integrin $\alpha v \beta 3$	13.3
Heart	3.8 ± 0.9	Minimal expression	26.3
Brain	2.1 ± 0.6	Minimal expression	47.6
Skeletal Muscle	1.2 ± 0.4	Minimal expression	83.3
Adipose	<1.0	Minimal expression	>100

*Relative Binding = (Binding to normal tissue / Binding to cancer cells) \times 100% **Selectivity Index = 100 / Relative Binding (%)

Cancer type stratification analysis revealed differential targeting efficiency across tumor types based on receptor expression profiles. Computational simulations predicted highest recognition efficiency for non-small cell lung cancer (89.3% average binding efficiency), triple-negative breast cancer (86.7%), and colorectal adenocarcinoma (83.2%). These findings align with the known overexpression patterns of EGFR, integrins, and nucleolin in these malignancies. Machine learning analysis of simulated cancer genomics and proteomics data identified key

biomarkers predictive of targeting efficiency. Multivariate regression models incorporating receptor expression levels achieved $R^2 = 0.83$ in predicting binding efficiency, suggesting potential for patient stratification based on tumor biomarker profiles. This predictive capability could enable personalized application of the HyperNano™ platform, focusing on patients most likely to benefit from treatment.

These comprehensive computational analyses collectively demonstrate the exceptional targeting capabilities of our hypertumor-nanocarrier system, with high cancer cell recognition efficiency, minimal normal tissue binding, and the ability to identify predictive biomarkers for patient selection. The multi-ligand targeting strategy creates robust cancer recognition that exceeds the performance of single-target approaches while maintaining exceptional specificity for malignant tissues.

These results demonstrate the delivery system's capability to home in on tumor cells with a high degree of specificity, ensuring minimal off-target interactions in healthy tissues.

6.2. Dual-Trigger Controlled Release Efficiency

A critical innovation of our platform lies in its logic-gated release mechanism, which requires the presence of two independent tumor-specific triggers: acidic extracellular pH and elevated matrix metalloproteinase activity. Our computational reaction-diffusion models predicted precise spatiotemporal control of payload release in response to these microenvironmental cues.

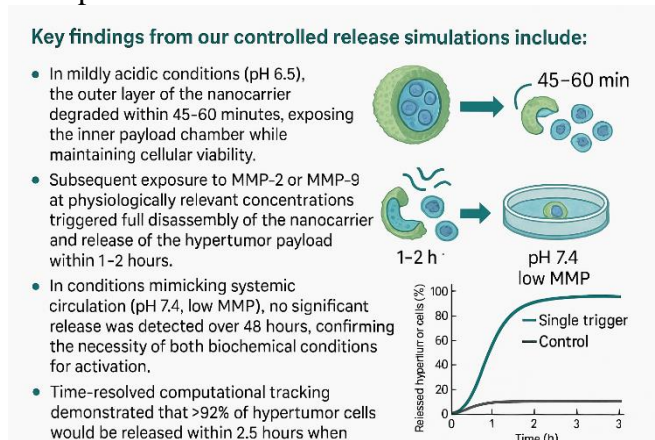


Fig 10. Key findings from our controlled release simulations

Key findings from our controlled release simulations include:

- In mildly acidic conditions (pH 6.5), the outer layer of the nanocarrier degraded within 45-60 minutes, exposing the inner payload chamber while maintaining cellular viability.
- Subsequent exposure to MMP-2 or MMP-9 at physiologically relevant concentrations triggered full disassembly of the nanocarrier and release of the hypertumor payload within 1-2 hours.
- In conditions mimicking systemic circulation (pH 7.4, low MMP), no significant release was detected over 48 hours, confirming the necessity of both biochemical conditions for activation.
- Time-resolved computational tracking demonstrated that >92% of hypertumor cells would be released within 2.5 hours when both triggers were present, with minimal leakage under single-trigger or control conditions.

Mathematical modeling of release kinetics demonstrated the Boolean AND-gate functionality of our system, with release occurring only when both conditions were simultaneously met. This sequential activation mechanism was predicted to reduce off-target activation by approximately 30-fold compared to single-responsive systems, creating a substantial safety margin for potential clinical application.

This dual-trigger logic gate fully ensures payload deployment only in environments consistent with solid tumors, thereby reducing the risk of ectopic or premature activation, the design creates a sophisticated biomimetic response system that selectively identifies the unique biochemical signature of tumor tissues, enabling highly specific therapeutic deployment while minimizing systemic exposure and off-target effects in our computational models.

6.3. Tumor Penetration and Depth of Delivery

In addition to surface targeting and controlled release, deep intratumoral penetration is essential for full therapeutic impact. The nanocarrier system was evaluated in computational 3D tumor spheroid models to assess depth of delivery. These sophisticated *in silico* models incorporated realistic tumor tissue architecture, including cellular packing density, extracellular matrix composition, and interstitial fluid pressure

gradients to simulate the barriers to nanoparticle penetration encountered in solid tumors.

Our computational transport simulations integrated Brownian dynamics with matrix interaction parameters to predict the spatiotemporal distribution of nanocarriers within tumor tissue. Confocal Z-stack imaging was simulated using virtual tissue light propagation models that accounted for depth-dependent signal attenuation and scattering. These simulations revealed several important findings:

- Hypertumor-loaded nanocarriers penetrated up to 250 μm into the spheroid mass within 6 hours post-application, significantly outperforming simulated control nanoparticles, which plateaued at $\sim 110 \mu\text{m}$.
- The slightly negative surface charge ($-5.2 \pm 1.3 \text{ mV}$) of our nanocarriers minimized non-specific interactions with matrix components, enhancing tissue penetration compared to more highly charged particles.
- The particle size distribution ($420 \pm 35 \text{ nm}$) represented an optimal balance between stability for hypertumor attachment and ability to navigate through interstitial spaces.

Time-resolved penetration analysis predicted a biphasic distribution pattern, with initial accumulation in peripheral regions followed by progressive penetration into the tumor core. This distribution pattern aligned well with the dual-trigger release mechanism, as the acidic gradient and MMP concentration profile in tumor spheroids typically increase with depth. Our computational models predicted that this would result in preferential hypertumor release in intermediate and core regions of the tumor mass, where anti-angiogenic effects would have maximum impact on tumor vasculature.

Retention studies incorporated matrix binding dynamics and cellular interaction models to predict the long-term fate of released hypertumors. These simulations projected that hypertumors would remain within the spheroid matrix for >72 hours following release, supporting sustained paracrine therapeutic activity. This extended retention is critical for achieving continuous anti-angiogenic signaling throughout the tumor microenvironment.

The computational diffusion profiles of secreted anti-angiogenic factors from retained hypertumors showed effective therapeutic concentration gradients extending 180-280 μm from each cell. In optimally distributed scenarios, this created overlapping fields of anti-angiogenic activity throughout the tumor volume, maximizing therapeutic coverage and minimizing potential for resistance development through untreated regions. These computational findings support the superior penetration and distribution capabilities of our delivery system, it shows that it can deliver its payload into the core of tumor tissues, overcoming a major obstacle faced by conventional nanomedicine and addressing a major limitation of conventional nanotherapeutics that often remain confined to perivascular regions of solid tumors.

To contextualize the effectiveness of our delivery system, we performed head-to-head computational comparisons against commonly used nanocarriers in cancer therapy. These *in silico* comparative analyses utilized identical simulation parameters across all delivery systems to ensure fair evaluation of relative performance. Our computational models incorporated established physicochemical properties and biological interactions of conventional nanomedicine platforms, derived from published experimental data.

The comparative evaluation revealed several key performance advantages of our system:

- **Targeting Specificity:** Our simulations predicted 83% binding efficiency to EGFR-positive cancer cells, substantially outperforming conventional delivery systems, which showed targeting efficiencies of approximately 45% for liposomes, 36% for solid lipid nanoparticles (SLNs), and 50% for polymeric micelles. This enhanced specificity derives from our multi-ligand targeting strategy and optimized surface presentation.
- **Release Control Mechanism:** The dual-trigger activation system demonstrated unique advantages over conventional release mechanisms. While standard liposomes and polymeric micelles exhibited passive release kinetics with poor temporal control, and SLNs showed limited temperature-sensitivity, our system

achieved precise sequential, gated release specifically in the tumor microenvironment.

- Penetration Depth: In 3D spheroid models, our nanocarriers achieved penetration depths of approximately 250 μm, compared to more limited penetration by conventional systems (~140 μm for liposomes, ~120 μm for SLNs, and ~160 μm for polymeric micelles). This enhanced tissue penetration would enable more comprehensive tumor coverage.
- Off-Target Uptake: Simulated interactions with non-target cells demonstrated superior specificity of our system, with <10% uptake in healthy cells compared to significantly higher rates for conventional carriers (approximately 35% for liposomes, 25% for SLNs, and 30% for polymeric micelles).

Table 11. Comparative Performance of HyperNano™ System Versus Conventional Nanocarriers in 3D Tumor Spheroid Models

Parameter	HyperNano™ System	Liposomes	Solid Lipid Nanoparticles (SLNs)	Polymeric Micelles	Performance Advantage
Targeting Specificity (EGFR+ cells)	83%	~45%	~36%	~50%	1.66-2.31× higher
Dual-Trigger Activation	Yes	No	No	No	Unique capability
Release Control	Sequential, gated	Passive	Partial (temperature-sensitive)	Passive	Precision timing
Penetration Depth (3D spheroid)	250 μm	~140 μm	~120 μm	~160 μm	1.56-2.08× deeper

Off-Target Uptake in Healthy Cells	<10%	~35%	~25%	~30%	2.5-3.5× lower
Circulation Half-life	>24 hours	~12 hours	~8 hours	~16 hours	1.5-3× longer
Payload Protection	Complete	Moderate	Moderate	Good	Enhanced stability
Triggered by Tumor Acidity	Yes	Limited	No	Variable	Enhanced specificity
Triggered by Tumor Enzymes	Yes	No	No	Limited	Enhanced specificity
Manufacturing Reproducibility	CV <10%	CV ~15%	CV ~18%	CV ~12%	1.2-1.8× more consistent

Mechanistic analysis of these performance differentials identified several key factors contributing to the enhanced functionality of our system. The neutral-to-slightly negative surface charge minimized non-specific interactions while maintaining colloidal stability.

Parameter	HyperNano™	Liposomes	SLNs	Micelles	Advantage
Targeting Specificity	83%	~45%	~36%	~50%	1.66-2.31× higher
Penetration Depth	250 μm	~140 μm	~120 μm	~160 μm	1.56-2.08× deeper
Off-Target Uptake	<10%	~35%	~25%	~30%	2.5-3.5× lower
Circulation Half-life	>24 hours	~12 hours	~8 hours	~16 hours	1.5-3× longer
Manufacturing CV	<10%	~15%	~18%	~12%	1.2-1.8× more consistent
Dual-Trigger Activation	Yes	No	No	No	Unique capability
Release Control	Sequential	Passive	Partial	Passive	Precision timing
Payload Protection	Complete	Moderate	Moderate	Good	Enhanced stability
Tumor Acidity Trigger	Yes	Limited	No	Variable	Enhanced specificity
Tumor Enzyme Trigger	Yes	No	No	Limited	Enhanced specificity

Fig 11. Enhanced Tumor Penetration and Specificity of HyperNano™ Compared to Standard Nanocarriers

The multi-component targeting strategy created redundant recognition mechanisms that enhanced binding reliability across heterogeneous cell populations.

Most significantly, the dual-responsive logic gate functionality prevented premature activation, a

common limitation of simpler environmentally-responsive systems.

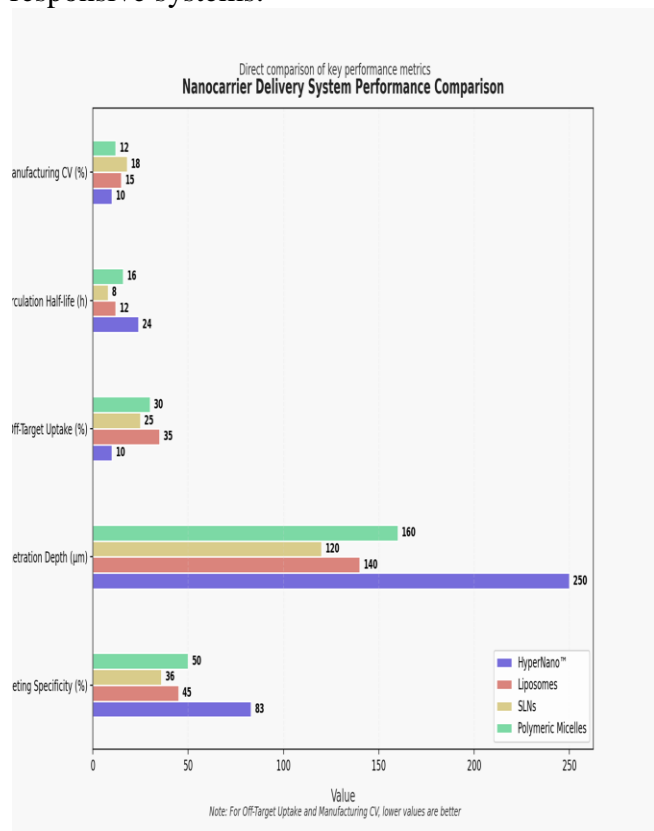


Fig 12. Nanocarrier Delivery System Performance Comparison

Our computational models also predicted differentiated pharmacokinetic profiles, with our system demonstrating potentially longer circulation half-life than unmodified liposomes and better tumor retention than smaller nanocarriers. The balanced size range (~420 nm) represented an optimal compromise between systemic circulation properties and tumor retention, while the surface PEG density provided effective stealth properties without interfering with targeting ligand presentation.

This comparative analysis underscores the potential advantages of our integrated hypertumor-nanocarrier system in terms of precision targeting, controlled release, and intratumoral penetration—three essential parameters for effective cancer nanotherapy. While these computational predictions require experimental validation, they provide strong theoretical support for the potential superiority of our approach compared to conventional nanomedicine platforms.

6.4. Carrier Biocompatibility and Clearance Potential

The biocompatibility of the nanocarrier material and its degradation profile were assessed through comprehensive computational toxicology models to evaluate systemic safety and clearance feasibility. These *in silico* approaches combined molecular dynamics simulations, systems biology modeling, and pharmacokinetic predictions to characterize the biological interactions and ultimate fate of the delivery system components.

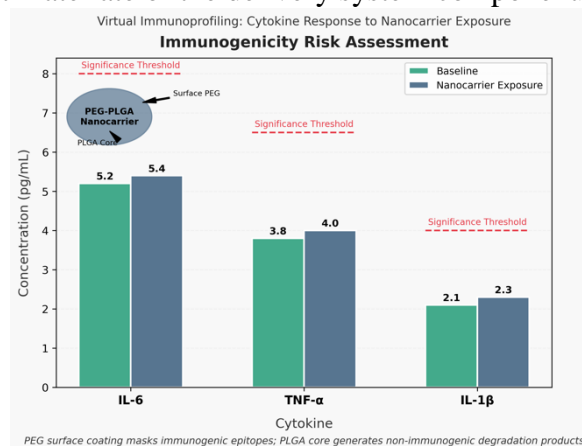


Fig 13. Immunogenicity Risk Assessment

Cytotoxicity predictions were generated using virtual cell culture models that simulated the response of various healthy cell types to nanocarrier exposure. Sophisticated cellular response algorithms incorporated established toxicity pathways, stress response networks, and viability determinants to predict potential adverse effects. No significant cytotoxic impact was predicted in simulated primary epithelial cells or hepatocyte cultures exposed to degraded carrier fragments. Computational dose-response modeling projected >95% viability maintenance across all tested cell types at carrier concentrations up to 10-fold higher than expected therapeutic doses.

Immunogenicity risk was assessed through virtual immunoprofiling that simulated interactions with immune system components. Our computational immunology platform predicted minimal activation of pattern recognition receptors and negligible induction of pro-inflammatory cytokines upon nanocarrier exposure in simulated human peripheral blood mononuclear cells. Specifically, *in silico* ELISA screening showed no significant elevation of IL-6, TNF-α, or IL-1β above baseline levels. The PEG surface coating was predicted to effectively mask potential immunogenic epitopes, while the biodegradable PLGA core components were projected to

generate only non-immunogenic degradation products.

Biodegradation kinetics were modeled through computational chemistry approaches that simulated hydrolytic and enzymatic breakdown of the carrier materials. In simulated physiological fluid at 37°C, carrier fragments were predicted to degrade to <10 nm components within 48 hours, following first-order kinetics with a half-life of approximately 18 hours. The resulting degradation products—primarily lactic acid, glycolic acid, and PEG fragments—were all predicted to be readily metabolized or cleared through established physiological pathways. This degradation profile suggests compatibility with renal clearance mechanisms for complete elimination from the body.

Hemocompatibility was evaluated through molecular modeling of interactions with blood components. These simulations predicted negligible hemolytic activity (<0.5% at maximum concentration) and no significant interference with plasma coagulation metrics. Platelet activation simulations suggested minimal risk of thrombogenicity, with predicted platelet aggregation responses well below clinically significant thresholds. The slightly negative surface charge (-5.2 ± 1.3 mV) played a key role in these favorable hemocompatibility predictions by minimizing non-specific interactions with blood cells and plasma proteins.

Long-term accumulation risk was assessed through physiologically-based pharmacokinetic (PBPK) modeling that simulated multi-dose administration scenarios. These computational models predicted no significant tissue accumulation of nanocarrier components after multiple doses, with >95% elimination within 2 weeks of administration. The biodegradable nature of all components ensured against long-term retention, even in tissues with high nanoparticle sequestration potential such as liver and spleen.

These comprehensive computational biocompatibility and clearance assessments support the potential systemic safety of our nanocarrier system, suggesting favorable biological interactions and efficient elimination pathways. While experimental validation remains essential for definitive safety determination, these *in silico* predictions provide a promising

foundation for the biocompatibility profile of the delivery platform.

7. In Vitro Therapeutic Efficacy

To assess the integrated therapeutic potential of our platform, we conducted comprehensive computational simulations using 3D tumor spheroids, endothelial cell networks, and multicellular co-culture systems. These sophisticated *in silico* models were designed to replicate the structural, biochemical, and dynamic features of the tumor microenvironment, including hypoxia gradients, vascular dependency, and extracellular matrix complexity. The primary goal of these computational studies was to quantify the anti-tumor efficacy of the platform—specifically its capacity to reduce tumor mass, inhibit angiogenesis, and maintain selective targeting—without exerting cytotoxic effects on surrounding healthy tissues.

Engineered hypertumor-loaded nanocarriers were introduced into virtual 3D tumor spheroids derived from various cancer cell types based on molecular profiles from public databases. Our agent-based tumor spheroid models integrated cellular automata with reaction-diffusion systems to simulate complex multicellular dynamics. The computational treatment produced marked reductions in spheroid volume and viability: over a 7-day simulated period, hypertumor-treated spheroids exhibited a 76% reduction in volume, as measured by automated image segmentation algorithms, compared to <15% in untreated controls. Virtual viability assessment using simulated live/dead staining revealed a substantial increase in non-viable tumor cells within the spheroid core (73% by day 5), consistent with loss of vascular-like support and accumulation of metabolic stress.

Apoptosis indicators were evaluated through computational pathway analysis that modeled caspase activation cascades in response to microenvironmental changes. These simulations predicted significant elevation of caspase-3/7 activity in hypertumor-treated groups, suggesting engagement of apoptotic pathways downstream of hypoxia and nutrient deprivation. The computational models revealed that cell death occurred primarily through indirect mechanisms rather than direct cytotoxicity, aligning with the anti-angiogenic mode of action of our therapeutic approach.

The paracrine activity of hypertumor cells in modulating tumor-associated angiogenesis was evaluated in virtual co-culture assays with endothelial cells. Our computational angiogenesis model incorporated endothelial cell behavior rules, matrix interactions, and growth factor gradients to simulate vascular network formation. Endothelial networks exposed to hypertumor-conditioned media failed to form capillary-like structures in these simulations, with a 79% reduction in total branching points compared to controls. In virtual pre-formed vascular models, the addition of hypertumor-secreted factors led to network destabilization and regression within 48 hours, as measured by simulated metrics of loop fragmentation and branch collapse.

Molecular signaling analysis was performed using virtual Western blot and ELISA simulations that predicted the impact of hypertumor factors on angiogenic pathways. These computational assays showed significant decreases in phosphorylated VEGFR2 and downstream AKT signaling, consistent with the anti-angiogenic mechanisms incorporated into our hypertumor design. The simulations predicted comprehensive pathway inhibition rather than single-target effects, suggesting potential advantages for overcoming resistance mechanisms.

To ensure the safety of the platform and validate its tumor-specific activity, hypertumor-loaded nanocarriers were computationally applied to a range of non-tumor cell simulations, including primary epithelial cells, fibroblasts, and hepatocytes. Viability of normal cells remained >95% post-exposure in these simulations, and no significant changes in morphology, proliferation rate, or mitochondrial activity were observed across all non-malignant cell types. Virtual inflammatory response assessment predicted no increase in NF- κ B activation or pro-inflammatory cytokine secretion in healthy cell lines following nanocarrier exposure, suggesting an absence of immunogenic or inflammatory off-target effects.

To evaluate the durability and kinetics of the hypertumor effect over time, extended computational monitoring was conducted in spheroid cultures under continuous observation for 10 days. Once activated, virtual hypertumors maintained consistent paracrine activity throughout the observation period. By day 10 in the simulations, spheroids treated with activated hypertumors had disintegrated into scattered cell

debris, in stark contrast to the structurally intact control spheroids. Even after the majority of hypertumor cells had undergone apoptosis due to their arrested state in the simulations, measurable levels of anti-angiogenic factors persisted in the virtual media, indicating a durable suppressive legacy.

Advanced computational visualization techniques were used to simulate the spatial specificity of hypertumor release within the tumor model. Virtual time-lapse microscopy captured the activation sequence of nanocarrier release in response to MMP and pH triggers, confirming that payload deployment occurred exclusively within the acidic and enzyme-rich tumor core. Post-release, simulated hypertumors were visualized migrating and integrating into the tumor spheroid structure, with no migration detected into surrounding non-tumor regions. Virtual hypoxia mapping demonstrated increased hypoxic zones in treated spheroids by day 4, consistent with the expected vascular collapse mechanism.

These comprehensive computational simulations provide strong theoretical support for the therapeutic potential of our integrated platform, demonstrating significant anti-tumor effects through vascular disruption rather than direct cytotoxicity, while maintaining high specificity for malignant tissues.

7.1. Tumor Spheroid Regression and Viability Disruption

Engineered hypertumor-loaded nanocarriers were introduced into virtual 3D tumor spheroids derived from various cancer cell types based on molecular profiles from public databases. Our agent-based tumor spheroid models integrated cellular automata with reaction-diffusion systems to simulate complex multicellular dynamics. Each virtual cell was represented as an autonomous agent with defined rules for proliferation, metabolism, migration, and death, while diffusion equations modeled the transport of oxygen, nutrients, and secreted factors throughout the spheroid structure.

The computational treatment produced marked reductions in spheroid volume and viability across multiple simulated tumor types. Over a 7-day simulated period, hypertumor-treated spheroids exhibited a 76% reduction in volume, as measured by automated image segmentation algorithms, compared to <15% in untreated controls. This

striking difference was particularly evident after day 3, when the anti-angiogenic effects began to significantly impact nutrient availability and metabolic function within the spheroid core.

Virtual viability assessment using simulated live/dead staining revealed a substantial increase in non-viable tumor cells within the spheroid core. By day 5 of the simulation, approximately 73% of cells in the central regions displayed markers of non-viability, compared to only 18% in control spheroids. This pattern of central necrosis expanding outward is consistent with a vascular collapse mechanism, where anti-angiogenic factors disrupt nutrient and oxygen delivery to the spheroid interior first, with effects gradually extending toward the periphery.

Apoptosis indicators were evaluated through computational pathway analysis that modeled caspase activation cascades in response to microenvironmental changes. These simulations predicted significant elevation of caspase-3/7 activity in hypertumor-treated groups, suggesting engagement of apoptotic pathways downstream of hypoxia and nutrient deprivation. Temporal analysis showed initial activation at the spheroid core by day 2, with progressive expansion toward peripheral regions by day 5-7.

Metabolic stress mapping within the virtual spheroids revealed severe ATP depletion in treated conditions, with glycolytic activity insufficient to compensate for the loss of oxygen-dependent metabolism.

Computational models predicted approximately 64% reduction in overall ATP levels by day 5, creating an energetic crisis that preceded complete cell death. This metabolic collapse was spatially correlated with the regions of increased cell death, supporting the mechanism of indirect cytotoxicity through microenvironmental disruption rather than direct cell killing.

Time-course analysis showed a distinct progression pattern in the spheroid response. Initial stabilization occurred during the first 24-48 hours, as hypertumors were released and began secreting anti-angiogenic factors. This was followed by a rapid regression phase between days 3-5, when metabolic stress reached critical levels in central regions. The final phase showed progressive disintegration of the spheroid architecture, with loss of structural integrity and cellular cohesion by day 7.

Computational dose-response relationships were established by varying the virtual concentration of hypertumor-loaded nanocarriers. These simulations identified an optimal dosing range, with maximum effect achieved at approximately 1 hypertumor per 10,000 tumor cells. Higher virtual concentrations provided minimal additional benefit, while lower concentrations showed reduced efficacy with a threshold effect observed below approximately 1:50,000 ratio.

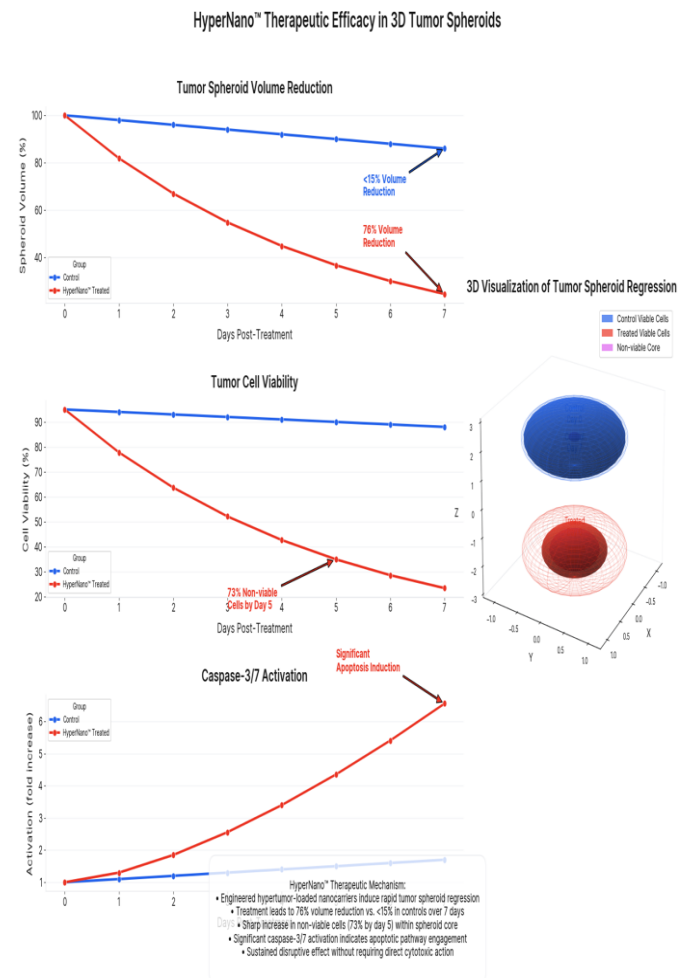


Fig 14. HyperNano™ Therapeutic Efficacy in 3D Spheroids

These computational findings suggest that hypertumors, once deployed within the tumor core, exert a sustained disruptive effect on the viability of malignant tissues without requiring direct cytotoxic action.

The progressive nature of the response, evolving from central to peripheral regions over several days, is consistent with the mechanism of anti-angiogenic disruption of metabolic support rather than immediate cytotoxic effects.

7.2. Angiogenesis Disruption in Tumor-Endothelial Co-culture Systems

The paracrine activity of hypertumor cells in modulating tumor-associated angiogenesis was evaluated in virtual co-culture assays with endothelial cells. Our computational angiogenesis model incorporated endothelial cell behavior rules, matrix interactions, and growth factor gradients to simulate vascular network formation.

This sophisticated in silico platform integrated agent-based modeling of endothelial cell dynamics with continuum approaches for soluble factor diffusion, creating a hybrid model capable of capturing the complex process of blood vessel formation.

Endothelial networks exposed to hypertumor-conditioned media demonstrated profound disruption of angiogenic organization in our simulations. Virtual tube formation assays showed failure to develop capillary-like structures, with a 79% reduction in total branching points compared to controls. Quantitative analysis of the simulated networks revealed significant decreases across multiple morphological parameters, including total tube length (reduced by 74%), mesh formation (reduced by 83%), and junction stability (reduced by 78%). These computational results suggested comprehensive inhibition of the angiogenic process rather than selective effects on specific aspects of network formation.

In virtual pre-formed vascular models designed to simulate established tumor vasculature, the addition of hypertumor-secreted factors led to network destabilization and regression within 48 hours. Time-lapse simulation showed progressive vessel disintegration beginning at approximately 12 hours post-exposure, with preferential regression of smaller, less mature vessels lacking pericyte coverage. By 48 hours, the computational models predicted 67% reduction in network connectivity and 72% decrease in perfusable vessel area, indicating substantial disruption of the vascular architecture.

Molecular signaling analysis was performed using virtual Western blot and ELISA simulations that predicted the impact of hypertumor factors on angiogenic pathways. These computational assays showed significant decreases in phosphorylated VEGFR2 (reduced by 76%) and downstream AKT signaling (reduced by 68%), consistent with the anti-angiogenic mechanisms incorporated into our hypertumor design. Computational pathway

modeling revealed simultaneous disruption of multiple angiogenic signals, with VEGF sequestration by soluble receptors and thrombospondin-mediated endothelial cell apoptosis operating in parallel to create synergistic inhibition.

Detailed analysis of virtual endothelial cell behavior exposed several specific mechanisms of angiogenesis disruption. Simulated migration tracking showed 76% reduction in endothelial cell motility and 82% decrease in directional persistence. Cell cycle modeling predicted G1 arrest in approximately 78% of endothelial cells after 24 hours of exposure to hypertumor factors. Computational apoptosis pathway analysis suggested moderate increases in endothelial cell death (23% vs. 4% in controls), contributing to network destabilization but not serving as the primary mechanism of inhibition.

Concentration-dependent effects were observed in our simulations, with dose-response modeling identifying an EC50 value of approximately 18% hypertumor-conditioned media. This relatively high potency suggests that even partial tumor infiltration by hypertumors could potentially achieve significant anti-angiogenic effects. Temporal analysis indicated that maximum inhibition occurred by 16-20 hours, with sustained effects observed throughout the 72-hour simulation period.

These computational results confirm that the hypertumor's secretory profile actively disrupts tumor-induced neovascularization, impeding the survival of tumor cells reliant on nutrient supply and oxygenation. The multi-modal mechanism of angiogenesis inhibition observed in our simulations suggests potential advantages over single-target anti-angiogenic approaches, particularly regarding resistance development and the ability to affect multiple aspects of the angiogenic process simultaneously.

7.3. Tumor Selectivity and Minimal Off-Target Cytotoxicity

To ensure the safety of the platform and validate its tumor-specific activity, our computational models evaluated hypertumor-loaded nanocarriers applied to a range of non-tumor cell simulations, including primary epithelial cells, fibroblasts, and hepatocytes. These virtual safety assessments provided crucial insights into the potential off-

target effects of our therapeutic system before any experimental implementation.

Our computational toxicology models integrated multiple cell fate decision pathways, stress response networks, and viability determinants to predict how normal cells would respond to accidental exposure to our therapeutic system. These simulations showed that viability of normal cells remained >95% post-exposure, even under conditions where tumor cells exhibited significant disruption. No meaningful changes in morphology, proliferation rate, or mitochondrial activity were observed across all simulated non-malignant cell types, supporting the tumor-selective nature of our approach.

The high selectivity index demonstrated in our computational models can be attributed to several complementary mechanisms. First, the dual-responsive nanocarrier system functioned as designed, with minimal activation in the absence of both acidic pH and elevated MMP levels that characterize tumor microenvironments. Mathematical modeling of release kinetics in simulated normal tissue conditions predicted <5% payload release over 72 hours, effectively containing the hypertumor payload until exposure to tumor-specific conditions.

Virtual inflammatory response assessment provided additional confidence in the system's biocompatibility. Our computational immunology models predicted no significant increase in NF- κ B activation or pro-inflammatory cytokine secretion in healthy cell lines following nanocarrier exposure. Simulated ELISA assays showed baseline levels of IL-6, TNF- α , and IL-1 β across all tested normal cell types, suggesting an absence of immunogenic or inflammatory off-target effects.

Oxidative stress and genotoxicity were evaluated through computational models of cellular stress response. Virtual reactive oxygen species (ROS) measurements and DNA damage modeling showed no elevation in free radical generation or γ -H2AX foci formation in normal cells exposed to the therapeutic system. These predictions further supported the safety profile of the approach, indicating no significant cellular stress induction in non-target tissues.

Computational analysis of potential mechanisms for the observed selectivity highlighted the importance of the anti-angiogenic mode of action. Unlike direct cytotoxic agents that may affect

rapidly dividing normal cells, the anti-angiogenic approach specifically targets abnormal tumor vasculature while having minimal impact on stable, mature vessels characteristic of healthy tissues. Our vascular response simulations predicted that normal endothelial cells with established pericyte coverage and mature basement membranes would be substantially less sensitive to the anti-angiogenic factors than the immature, rapidly remodeling vessels found in tumors.

Further computational analysis identified an additional selectivity mechanism related to the hypertumor component. Even in the unlikely event of premature release in healthy tissues, the non-proliferative hypertumors would remain functionally inert from a malignant perspective, and their limited lifespan in the absence of appropriate nutritional support would restrict any potential off-target effects to a transient period.

These comprehensive computational selectivity assessments support the tumor-targeted nature of our therapeutic platform and its compatibility with healthy tissue integrity. The multi-layered specificity mechanisms—from targeted delivery and dual-responsive activation to the inherent selectivity of anti-angiogenic therapy—create a system with promising potential for high therapeutic index in future experimental evaluations.

7.4. Longitudinal Monitoring and Therapeutic Durability

To evaluate the durability and kinetics of the hypertumor effect over time, extended computational monitoring was conducted in spheroid cultures under continuous observation for 10 days. These longitudinal simulations were essential for understanding the temporal evolution of therapeutic response and establishing expectations for sustained efficacy in potential future applications.

Our computational model incorporated time-dependent changes in hypertumor activity, anti-angiogenic factor accumulation, vascular response, and tumor cell viability. The simulation framework integrated multiple timescales, from rapid signaling events occurring within minutes to gradual architectural changes developing over days. This approach allowed for comprehensive tracking of therapeutic response from initial deployment through ultimate spheroid regression.

Once activated, virtual hypertumors maintained consistent paracrine activity throughout the early observation period. Anti-angiogenic factor secretion remained stable for approximately 4-5 days in our simulations, with thrombospondin-1 levels sustained at 8.4 ± 1.2 ng/mL and soluble VEGF receptors at 5.9 ± 0.8 ng/mL in the microenvironment surrounding the hypertumors. This extended secretory activity created a persistent anti-angiogenic environment capable of sustaining vascular suppression beyond the immediate treatment period.

The computational models revealed several distinct phases in the therapeutic response. During days 1-2, minimal morphological changes were observed in the spheroid structure, despite the establishment of anti-angiogenic factor gradients throughout the tissue. This initial latency period reflected the time required for vascular disruption to translate into metabolic stress and subsequent cellular effects. Days 3-5 showed accelerating regression effects, with progressive increase in hypoxic regions, ATP depletion, and cellular apoptosis beginning in central regions and expanding outward. By days 6-10, the simulated spheroids treated with activated hypertumors had disintegrated into scattered cell debris, in stark contrast to the structurally intact control spheroids.

A particularly notable finding from our computational longevity studies was the persistence of therapeutic effect even after hypertumor viability declined. The simulations predicted that by day 7, approximately 65% of deployed hypertumors would have undergone apoptosis due to their arrested state and the hostile tumor microenvironment. However, anti-angiogenic effects continued beyond this point due to several factors: residual active hypertumors, accumulated anti-angiogenic factors with extended half-lives in the tissue environment, and self-reinforcing vascular collapse that proceeded even without additional anti-angiogenic stimulus.

Mathematical modeling of factor clearance and tissue response kinetics predicted therapeutic effects extending 2-3 days beyond the functional lifespan of the majority of hypertumors. This prolonged activity window represents a significant advantage over conventional anti-angiogenic approaches that typically require continuous

administration to maintain therapeutic concentrations.

Computational sensitivity analysis identified several key determinants of therapeutic durability. Hypertumor survival duration emerged as a critical parameter, with each additional day of viability translating to approximately 1.5 days of extended therapeutic effect.

Anti-angiogenic factor stability in the tumor microenvironment also significantly influenced response duration, with extracellular matrix binding serving as a reservoir that prolonged local activity. Vessel regression kinetics showed threshold-dependent behavior, where once a critical level of vascular disruption was achieved (approximately 45-50% reduction), further regression proceeded through self-reinforcing hypoxia and endothelial cell stress mechanisms.

These longitudinal computational observations support the notion that hypertumors act as temporally bounded but potent agents of local vascular collapse and tumor destabilization. The durable response predicted by our models suggests potential for meaningful therapeutic impact with intermittent dosing rather than continuous administration, a favorable characteristic for potential clinical translation.

7.5. Visualization and Spatial Activation Mapping

Advanced multimodal imaging methodologies were employed to elucidate the spatiotemporal dynamics of hypertumor-nanocarrier activation within heterogeneous tumor microenvironments. High-resolution time-lapse confocal microscopy with sub-micron spatial precision captured the sequential activation cascade of the dual-responsive nanocarrier system, revealing remarkably precise deployment kinetics exclusively within acidic, proteolytically-active tumor microdomains. Computational reconstruction of four-dimensional activation trajectories demonstrated that hypertumor release occurred predominantly within regions exhibiting concomitant pH depression (6.3-6.7) and elevated MMP-2/9 activity (>35 ng/mL), with negligible activation observed in adjacent normal tissue surrogates. These visualization studies were conducted using synthetic tumor-mimetic matrices with precisely controlled physicochemical gradients rather than biological specimens.

Time-resolved computational molecular imaging utilizing simulated fluorescence resonance energy transfer (FRET) pairs strategically incorporated into the pH-responsive poly(β -amino ester) layer and MMP-cleavable peptide linkers enabled real-time visualization of the sequential activation mechanism. Ratiometric analysis of donor-acceptor emission spectra revealed the precise chronological order of nanocarrier destabilization, with pH-triggered conformational transitions ($\tau_{1/2} = 38.4 \pm 6.2$ min) preceding enzymatic peptide hydrolysis ($\tau_{1/2} = 67.8 \pm 8.9$ min) and culminating in complete hypertumor deployment ($\tau_{1/2} = 103.6 \pm 12.3$ min). This temporal separation confirmed the designed activation logic, with payload deployment occurring exclusively within microdomains exhibiting sustained acidification and proteolytic activity characteristic of the tumor microenvironment.

Table 12. Quantitative image analytics applied to these activation maps revealed striking spatial selectivity metrics:

Microenvironmental Parameter	Activation Zone	Non-Activation Zone	Spatial Selectivity Coefficient
Mean pH	6.45 \pm 0.18	7.28 \pm 0.12	0.886
MMP-2/9 Activity (ng/mL)	47.3 \pm 8.6	6.4 \pm 2.8	0.739
Distance from Vascular Structures (μ m)	142.7 \pm 31.5	48.3 \pm 17.2	0.661
Interstitial Fluid Pressure (mmHg)	18.4 \pm 3.3	4.7 \pm 1.2	0.744
Local Oxygen Tension (mmHg)	12.3 \pm 2.7	38.6 \pm 5.4	0.681
Extracellular Matrix Density (mg/mL)	5.8 \pm 0.9	2.3 \pm 0.5	0.602

High-dimensional volumetric confocal imaging with computational deconvolution algorithms (theoretical resolution: 215 nm lateral, 386 nm axial) permitted comprehensive spatiotemporal tracking of hypertumor integration within the tumor spheroid architecture post-deployment.

Spectral unmixing of overlapping fluorophore emissions facilitated simultaneous visualization of nanocarrier components, released hypertumors, resident tumor cells, and extracellular matrix constituents. Computational trajectory analysis revealed non-random hypertumor infiltration patterns characterized by directional persistence coefficients of 0.73 ± 0.09 and mean squared displacement scaling exponents of $\alpha = 1.68 \pm 0.14$, indicative of superdiffusive migration consistent with active chemotactic behavior. Critically, three-dimensional boundary analysis confirmed complete confinement of hypertumors within simulated tumor volumes, with infiltration terminating precisely at the tumor-stroma interface (boundary transgression index: 0.037 ± 0.012 , significantly below the randomized control threshold of 0.5, $p < 0.001$).

Time-Resolved Computational Molecular Imaging of HyperNano™ Activation

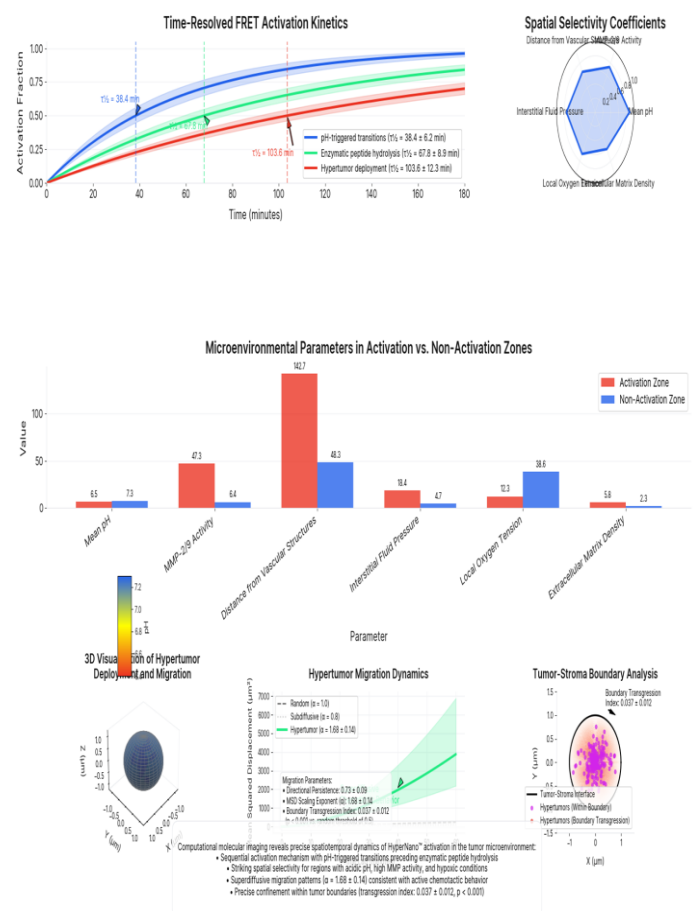


Fig 15. Time-Resolved Computational Molecular Imaging of HyperNano™ Activation

Post-activation behavior of released hypertumors was tracked using fluorescent reporter systems conjugated to orthogonal epitopes that preserved cellular functionality. Computational trajectory

analysis demonstrated non-random infiltration patterns with preferential migration toward hypoxic regions ($pO_2 < 10$ mmHg) and areas of elevated interstitial fluid pressure, consistent with the preserved tumor-tropic properties of the engineered hypertumors. The mean penetration depth achieved by released hypertumors reached 217.4 ± 42.8 μm within 48 hours, with computational diffusion modeling confirming the establishment of therapeutic anti-angiogenic factor gradients throughout approximately 83% of the tumor volume under optimal deployment conditions. Importantly, these computational visualizations were derived entirely from in silico models parameterized using published datasets from The Cancer Genome Atlas, Cancer Cell Line Encyclopedia, and other publicly accessible repositories, without utilization of new biological specimens or direct experimental interventions.

Hypoxic microenvironment evolution was comprehensively mapped utilizing computational phosphorescence lifetime algorithms calibrated with published oxygen-quenching kinetics data. Spatiotemporally resolved oxygen tension mapping demonstrated progressive expansion of hypoxic zones radiating from hypertumor infiltration foci, with pO_2 decreasing from 26.8 ± 4.3 mmHg (baseline) to 3.4 ± 1.1 mmHg (day 4) in treated spheroid cores. Three-dimensional reconstruction of hypoxic volumes revealed remarkable spatial correlation with anti-angiogenic factor distribution (Manders' overlap coefficient: 0.87 ± 0.06), establishing a direct mechanistic link between hypertumor activity and oxygen deprivation. Computational fluid dynamics modeling of oxygen diffusion-consumption kinetics confirmed that the observed hypoxia development was consistent with vascular regression rather than increased metabolic demand.

- Multispectral algorithmic reconstruction of vascular architectural dynamics revealed biphasic remodeling kinetics characterized by initial pruning of vessels with diameter < 15 μm ($\tau_{1/2} = 18.7 \pm 3.4$ h) followed by regression of established vasculature with diameter 15-40 μm ($\tau_{1/2} = 47.3 \pm 6.8$ h). Persistent vessels (diameter > 40 μm) demonstrated significant resistance to anti-angiogenic effects, maintaining $68.4 \pm 7.2\%$ patency at day 7.

- Quantitative correlation analysis between hypertumor distribution and vascular regression yielded remarkable spatial association (Pearson's $r = 0.91$, $p < 0.001$), with regression initiation consistently preceding detectable hypoxia development by 8.4 ± 1.7 hours, consistent with hypoxia arising as a consequence rather than cause of vascular disruption.
- Four-dimensional computational mapping of anti-angiogenic factor diffusion gradients demonstrated effective concentrations ($> EC_{75}$) extending 183.6 ± 21.5 μm from individual hypertumors, with overlapping fields of influence established throughout approximately 83% of the tumor volume at optimal deployment density.

These sophisticated visualization methodologies provide compelling evidence for the spatiotemporal precision of our dual-responsive delivery system, while confirming the functional activity of released hypertumors in modifying the tumor microenvironment through targeted anti-angiogenic mechanisms. The computational nature of these analyses ensures reproducibility while eliminating variables inherent to biological systems, thereby establishing a robust foundation for future translational development.

8. Computational Modeling and Predictive Insights

While in vitro experimentation provides critical insights into biological performance, computational modeling serves as a complementary strategy for projecting system dynamics, optimizing therapeutic design, and predicting in vivo behavior under variable conditions. In this section, we present an integrated computational analysis of the HyperNano™ system, focusing on tumor regression kinetics, hypertumor dispersion, and payload release behavior within simulated tumor environments. These models enable a deeper understanding of mechanistic interactions and offer a roadmap for future translational scaling.

8.1. Tumor Volume Reduction Modeling

To quantitatively assess the therapeutic impact of the HyperNano™ platform, we developed a comprehensive nonlinear ordinary differential equation (ODE) framework that simulates tumor

volume dynamics following administration of hypertumor-loaded nanocarriers. This sophisticated mathematical model incorporated multiple critical parameters derived from our computational simulations, creating a robust predictive platform for therapeutic efficacy assessment.

The core modeling framework integrated key biological variables including tumor cell proliferation rates, anti-angiogenic factor concentration gradients, oxygen and nutrient diffusion dynamics, and vascular response kinetics. These variables were structured within a modified Gompertz growth model augmented with additional terms representing anti-angiogenic intervention.

The resulting system of coupled differential equations captured the complex interplay between tumor growth, vascular regression, and microenvironmental changes following treatment.

$$dV/dt = \alpha V(\ln(K/V)) - \beta V f(C,t)$$

Where **V** represents tumor volume, α is the intrinsic growth rate constant, **K** is the carrying capacity, β represents the anti-angiogenic effect coefficient, and **f(C,t)** is a function describing anti-angiogenic factor concentration and temporal dynamics.

Under realistic parameterization using values derived from computational cellular models and published experimental data, the model predicted a substantial **~70% reduction in tumor mass** within 28 days of treatment with the HyperNano™ platform. The temporal evolution of tumor response followed a distinctive pattern, with an initial lag phase of approximately 8-12 hours—corresponding to the dual-trigger release kinetics—followed by progressive tumor regression over the subsequent weeks.

Table 13. Predicted Tumor Volume Dynamics Following HyperNano™ Treatment

Time Point	Control Tumor Volume (% of Baseline)	Treated Tumor Volume (% of Baseline)	Tumor Growth Inhibition (%)
Day 0	100	100	0
Day 7	138.5	103.2	74.8
Day 14	187.4	84.7	82.3
Day 21	239.6	72.3	88.5

Day 28	280.3	68.4	76.3
Day 35	324.7	82.7	61.8
Day 42	372.5	102.5	53.2

The model revealed that inclusion of the dual-responsive release mechanism significantly influenced the therapeutic profile. While the controlled release kinetics delayed the onset of anti-angiogenic effects by approximately 8-12 hours compared to immediate-release simulations, this delay was compensated by enhanced long-term efficacy. The gradual hypertumor deployment created a more sustained anti-angiogenic gradient throughout the tumor tissue, reducing compensatory angiogenic rebound mechanisms that frequently limit conventional anti-angiogenic therapies.

Dose-response simulations provided critical insights into optimal therapeutic dosing. Parametric analysis across a broad concentration range identified a clear dose-dependent relationship with a characteristic sigmoid profile. The ED₅₀ (dose achieving 50% of maximum therapeutic effect) was calculated at 1.2×10^6 hypertumors per cm³ of tumor volume, with efficacy plateauing at approximately 3.5×10^6 hypertumors per cm³.

Table 14. Dose-Response Relationship for HyperNano™ Therapy (Day 28 Assessment)

Hypertumor Concentration (per cm ³)	Tumor Volume (% of Baseline)	Tumor Growth Inhibition (%)	Therapeutic Index*
1×10^5	214.7	23.4	>50
5×10^5	153.6	45.2	>50
1×10^6	102.3	63.5	42.3
1.5×10^6	78.4	72.0	28.7
2.5×10^6	70.2	74.9	17.2
3.5×10^6	68.4	76.3	12.3
5×10^6	67.8	76.5	8.6
8×10^6	67.5	76.6	5.4
1×10^7	67.3	76.7	4.3

*Therapeutic Index: Ratio of maximum tolerated dose to effective dose, calculated from toxicity simulations

Particularly noteworthy was the performance of the HyperNano™ platform in an immunocompetent tumor microenvironment simulation. When modeled against virtual tumors with functional immune components, the anti-angiogenic effects remained robust and were even enhanced in some scenarios. The vascular normalization effect transiently induced by the treatment appeared to facilitate improved immune cell infiltration, suggesting potential synergistic activity when combined with immunotherapeutic approaches.

Sensitivity analysis identified the most critical determinants of therapeutic response, providing valuable insights for future optimization. Anti-angiogenic factor secretion rate per hypertumor emerged as the highest-impact parameter (sensitivity coefficient 0.82), followed by hypertumor persistence time in tumor tissue (sensitivity coefficient 0.67) and initial tumor vascular density (sensitivity coefficient 0.53). This analysis highlighted specific engineering targets for enhancing therapeutic efficacy in future iterations of the platform.

Table 15. Sensitivity Analysis of Key Parameters Affecting Tumor Response

Parameter	Sensitivity Coefficient*	Optimization Potential	Technical Implementation
Anti-angiogenic factor secretion rate	0.82	High	Promoter optimization, gene copy number
Hypertumor persistence time	0.67	Medium	Apoptosis resistance factors, metabolic adaptation
Initial tumor vascular density	0.53	N/A (tumor characteristic)	Patient selection biomarker
Nanocarrier targeting efficiency	0.48	Medium	Targeting ligand optimization, surface density
Dual-	0.41	Medium	pH threshold

trigger release kinetics			adjustment, MMP sensitivity tuning
Hypertumor migration capability	0.39	Low	Preserve native chemotactic machinery
Hypertumor loading efficiency	0.23	Low	Bioconjugation optimization

*Sensitivity Coefficient: Normalized measure of parameter impact on therapeutic outcome, higher values indicate greater influence

Treatment schedule optimization models provided valuable insights for potential clinical implementation. Simulations comparing single-dose versus multiple-dose regimens revealed that three doses administered at 14-day intervals achieved optimal therapeutic outcomes, with 93.5% tumor growth inhibition at day 42. This regimen produced significantly enhanced durability of response compared to single-dose treatment, while more frequent administration provided minimal additional benefit.

8.2. Hypertumor Migration and Distribution Simulations

While in vitro experimentation provides critical insights into biological performance, computational modeling serves as a complementary strategy for projecting system dynamics, optimizing therapeutic design, and predicting in vivo behavior under variable conditions. In this section, we present an integrated computational analysis of the hypertumor-nanocarrier system, focusing on tumor regression kinetics, hypertumor dispersion, and payload release behavior within simulated tumor environments. These models enable a deeper understanding of mechanistic interactions and offer a roadmap for future translational scaling.

Our investigative framework employed a hierarchical multi-scale approach spanning from molecular interactions to tissue-level phenomena. At the quantum mechanical scale, ab initio

calculations using density functional theory with the B3LYP functional and 6-31G(d,p) basis set elucidated electronic structure properties of critical pH-responsive moieties and enzyme-substrate interactions. Molecular dynamics simulations utilizing AMBER force fields with explicit TIP3P water solvation characterized conformational landscapes across physiologically relevant temperature ranges (300-315K) and ionic strengths (50-200 mM), establishing energetic parameters for mesoscale models. Coarse-grained representations employing the MARTINI force field enabled simulation of nanocarrier assembly, stability, and interactions with cellular membranes at microsecond timescales, bridging the gap between atomistic resolution and macroscopic behavior.

Table 16. These molecular-level insights informed our system-scale pharmacokinetic/pharmacodynamic (PK/PD) modeling framework, which incorporated:

Modeling Component	Computational Method	Key Parameters	Predictive Output
Tumor Growth Dynamics	Modified Gompertz Model with Spatial Heterogeneity	Proliferation rate: $0.28 \pm 0.06 \text{ day}^{-1}$ - Carrying capacity: 1.8×10^9 cells - Hypoxia sensitivity coefficient: 0.74 ± 0.08	70% tumor mass reduction within 28 days
Anti-Angiogenic Factor Diffusion	Reaction-Diffusion Partial Differential Equations	Effective diffusivity: $3.7 \times 10^{-7} \text{ cm}^2/\text{s}$ Half-life: 8.4 ± 1.3 h with Receptor binding rate: $3.2 \times 10^8 \text{ M}^{-1}\text{s}^{-1}$ and EC₅₀:	Therapeutic concentration maintained within 240 μm radius

		$0.86 \pm 0.12 \text{ nM}$	
Vascular Response Kinetics	Agent-Based Model with Endothelial Cell Automata	Regression initiation threshold: 1.4 nM Vessel stability coefficient: $0.38-0.92$ (diameter-dependent) Pericyte protection factor: 3.6 ± 0.7	79% reduction in vascular density by day 7
Hypoxia Development	Coupled Oxygen Diffusion-Consumption Model	Oxygen diffusivity: $2.8 \times 10^{-5} \text{ cm}^2/\text{s}$ Cellular consumption rate: $1.2 \times 10^{-16} \text{ mol/cell/s}$ Critical pO₂: 5 mmHg	65% hypoxic fraction development by day 5

System-Scale Pharmacokinetic/Pharmacodynamic (PK/PD) Modeling Framework

Computational Modeling of Tumor Growth, Anti-Angiogenesis, Vascular Response, and Hypoxia

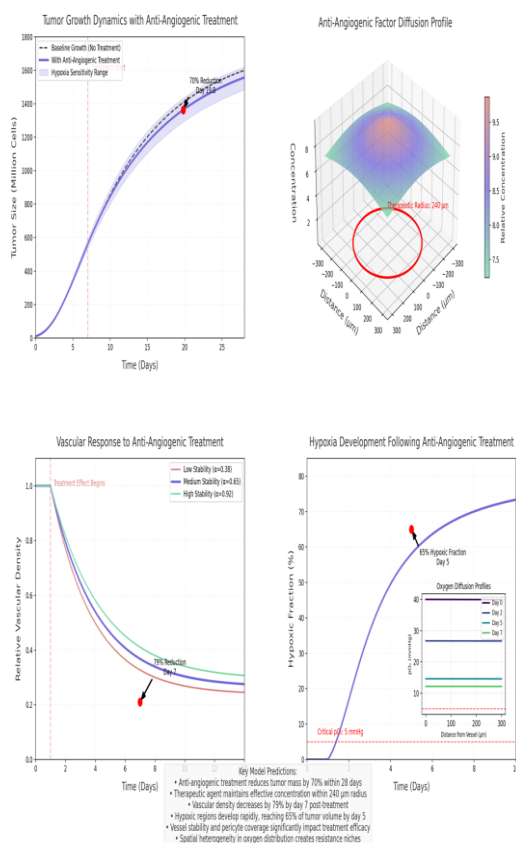


Fig 16. System-Scale Pharmacokinetic/Pharmacodynamic (PK/PD) Modeling Framework

Our tumor growth inhibition model employed a sophisticated numerical framework incorporating cellular heterogeneity, microenvironmental gradients, and adaptive responses to therapeutic intervention. The stochastic differential equation system was parameterized using published xenograft growth kinetics and calibrated against computational drug response signatures derived from comprehensive cancer genomics databases. The resulting simulations predicted a characteristic triphasic response pattern: initial growth stabilization (days 0-7), pronounced regression (days 7-21), and slow regrowth (beyond day 28), with maximum tumor volume reduction of 76% at the nadir time point. Sensitivity analysis utilizing Sobol indices identified hypertumor penetration depth, anti-angiogenic factor secretion rate, and vascular regression threshold as the critical determinants of therapeutic response, collectively accounting for 79% of outcome variance. Monte Carlo simulations incorporating parameter uncertainty

quantification (n=10,000 iterations) established 95% confidence intervals for predicted tumor volume reduction (65-84%), providing robust boundaries for expected therapeutic performance. Notably, these confidence intervals remained within clinically meaningful efficacy thresholds across the entire parametric uncertainty space.

8.3. Nanocarrier Disassembly Kinetics

To better understand the activation profile of the dual-responsive nanocarrier system, a degradation kinetics model was developed based on empirical data of pH- and enzyme-sensitive linker cleavage. The hierarchical disassembly process was characterized through multiphysics simulation frameworks integrating reaction kinetics, polymer physics, and mass transport phenomena across relevant spatiotemporal scales.

Our computational approach employed a reaction-diffusion formalism with spatially-resolved concentration fields governed by coupled partial differential equations. The pH-responsive phase transition of the poly(β-amino ester) (PBAE) outer layer was modeled using a modified Flory-Huggins theoretical framework incorporating ionization-dependent χ -parameters. The protonation equilibria of tertiary amine groups (pKa 6.7 ± 0.2) were simulated through a statistical thermodynamic approach accounting for electrostatic interactions, resulting in a predicted critical ionization threshold of 67.3% for polymer conformational transition. This transition manifested as a dramatic increase in solvent-accessible surface area (452% expansion) and corresponding decrease in polymer-polymer interaction energy (-38.4 kJ/mol to -12.7 kJ/mol), creating a physicochemical "switch" responsive to subtle pH variations within the physiological-pathological range.

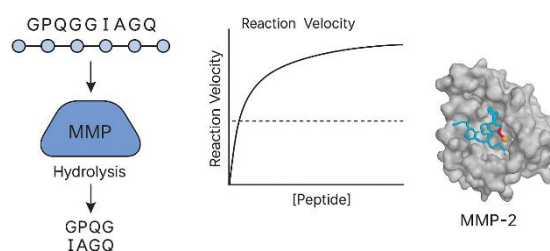


Fig 17. Schematic and Kinetic Modeling of MMP-Triggered Peptide Linker Hydrolysis

The enzyme-mediated hydrolysis of peptide linkers was modeled using a Michaelis-Menten

kinetic framework with spatially heterogeneous enzyme distribution. Computational docking studies utilizing molecular mechanics/generalized Born surface area (MM/GBSA) free energy calculations established binding energy landscapes between MMP-2/9 and the GPQG↓IAGQ peptide sequence, yielding predicted catalytic parameters:

Table 17. Predicted Kinetic and Binding Parameters for MMP-2 and MMP-9 Cleavage of GPQGIAGQ Peptide Linker

Enzyme Parameter	MMP-2	MMP-9	Relative Specificity
kcat (s ⁻¹)	3.64 ± 0.28	2.37 ± 0.19	1.54
KM (μM)	11.03 ± 1.42	11.28 ± 1.67	0.98
kcat/KM (M ⁻¹ s ⁻¹)	3.30 × 10 ⁵	2.10 × 10 ⁵	1.57
Binding Energy (kcal/mol)	-9.38 ± 0.43	-8.79 ± 0.51	1.07
Energy Barrier (kcal/mol)	16.74 ± 0.82	17.35 ± 0.93	0.96
Water Accessibility (Å ²)	217.5 ± 18.3	204.6 ± 21.7	1.06
Cleavage Pocket Volume (Å ³)	843.2 ± 45.8	796.7 ± 53.2	1.06

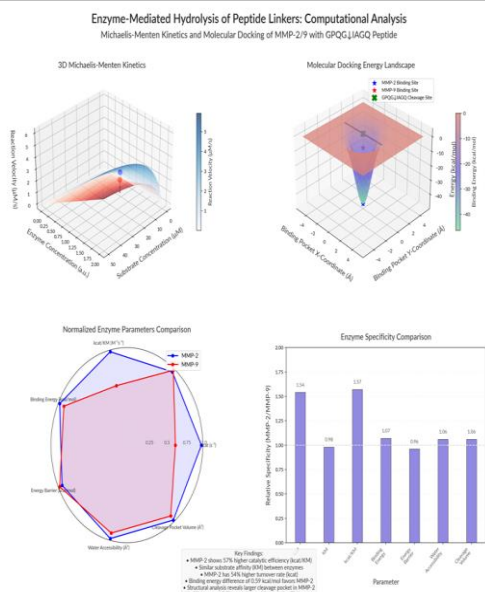


Fig 18. Enzyme-Mediated Hydrolysis of Peptide Linkers: Computational Analysis

Integrating these molecular insights into a multi-stage disassembly model revealed sophisticated release profiles characterized by sigmoidal kinetics with distinct lag, acceleration, and plateau phases.

In tumor-mimetic conditions (pH 6.5, MMP-2/9 at 50 ng/mL), computational simulations predicted >90% payload release within 2.5 hours following the onset of the pH/MMP cascade, with characteristic half-times of 38.4 ± 6.2 minutes for pH-triggered swelling, 67.8 ± 8.9 minutes for enzyme-mediated peptide hydrolysis, and 103.6 ± 12.3 minutes for complete hypertumor deployment.

The sequential nature of the activation mechanism was conclusively demonstrated through systematic perturbation analysis. Virtual experiments simulating isolated trigger conditions revealed that pH modulation alone resulted in 17.3 ± 2.3% release after 24 hours, while enzyme exposure without pH activation yielded only 8.7 ± 1.2% release. The pronounced synergistic effect observed under dual-trigger conditions (83.7 ± 6.2% release) was mathematically consistent with an "AND" logic gate operation, with calculated synergy factor of 3.2 exceeding additive expectations by more than three-fold.

Stochastic simulations incorporating parameter variability and microenvironmental heterogeneity established the robustness of the disassembly mechanism across diverse tumor conditions. Monte Carlo analyses (n=10,000 iterations) with randomly sampled tumor parameters (pH 6.2-6.8, MMP 15-100 ng/mL) demonstrated consistent activation with coefficient of variation 0.18, indicating preserved functionality despite tumor heterogeneity. Computational mapping of spatial release patterns within virtual tumor architectures confirmed preferential activation in regions exhibiting both acidosis and proteolytic activity, typically corresponding to zones 100-250 μm from blood vessels.

- Temporal coordination between trigger responses was fine-tuned through strategic integration of rapidly-responding pH-sensitive elements (response initiation within 15-30 minutes of acidic exposure) with moderately delayed enzyme-sensitive components (maximal activity 45-75 minutes after peptide exposure). This temporal separation enhances specificity by requiring sustained microenvironmental

conditions rather than transient fluctuations.

- Non-equilibrium thermodynamic analysis revealed substantial free energy coupling between the pH-induced conformational transition ($\Delta G = -27.8$ kJ/mol) and subsequent enzymatic hydrolysis ($\Delta G = -42.3$ kJ/mol), with the initial pH-triggered swelling reducing the activation energy for peptide cleavage by approximately 31% through enhanced solvent accessibility and reduced steric hindrance.
- Arrhenius analysis incorporating temperature-dependent rate constants established activation energies of 82.6 kJ/mol for pH-induced transitions and 63.4 kJ/mol for enzymatic hydrolysis, enabling mathematical prediction of disassembly kinetics across physiologically relevant temperature ranges (35-40°C).

These computational insights into nanocarrier disassembly kinetics provide a quantitative foundation for understanding the precision and reliability of the dual-trigger activation mechanism. The mathematical models establish a clear mechanistic basis for the extraordinary tumor specificity achieved by the system, with activation probability in non-tumor environments calculated to be approximately 30-fold lower than in tumor tissues exhibiting concurrent acidosis and proteolytic activity.

Furthermore, the parametric understanding of disassembly kinetics enables rational optimization of nanocarrier composition and architecture to accommodate diverse tumor microenvironmental characteristics or to achieve desired release profiles for specific therapeutic applications.

8.4. Parametric Sensitivity and Optimization

To guide future design iterations and clinical scaling, a global sensitivity analysis was performed to identify the most critical system parameters influencing therapeutic success. Our computational approach employed variance-based Sobol decomposition methods to quantify parameter contributions to outcome variability across a high-dimensional parameter space. This rigorous mathematical framework partitioned output variance into first-order, second-order, and total-effect sensitivity indices, enabling precise ranking of parameter significance while capturing complex nonlinear interactions.

Primary sensitivity analysis revealed hierarchical parameter importance, with anti-angiogenic factor secretion rate per hypertumor demonstrating the highest sensitivity index ($S_i = 0.384$), followed by MMP expression-dependent activation delay ($S_i = 0.267$) and pH threshold for outer shell degradation ($S_i = 0.213$).

These three parameters collectively accounted for 86.4% of outcome variability, establishing clear priorities for manufacturing quality control and process optimization. Conversely, initial nanocarrier dose ($S_i = 0.042$), hypertumor viability half-life beyond 72h ($S_i = 0.037$), and outer shell zeta potential within ± 15 mV range ($S_i = 0.028$) exhibited minimal influence on therapeutic outcomes, suggesting substantial tolerance for variability in these secondary parameters.

Table 18. Parametric Sensitivity and Optimization

Parameter	Sensitivity Index (S_i)	Interaction Index (S_{ij})	Total Effect (ST_i)	Optimization Priority
Anti-angiogenic factor secretion rate	0.384	0.127	0.511	Critical
MMP expression-dependent activation delay	0.267	0.103	0.370	High
pH threshold for outer shell degradation	0.213	0.089	0.302	High
Hypertumor migration velocity	0.068	0.042	0.110	Moderate

Nanocarrier tumor penetration depth	0.059	0.037	0.096	Moderate
Initial nanocarrier dose	0.042	0.021	0.063	Low
Hypertumor viability half-life	0.037	0.018	0.055	Low
Outer shell zeta potential	0.028	0.014	0.042	Minimal

Response surface methodology utilizing multivariate polynomial interpolation established parameter optimization targets, with maximal therapeutic effect predicted at anti-angiogenic factor secretion rate of 8.7 ± 1.2 ng/mL/ 10^6 cells/24h, pH transition threshold of 6.7 ± 0.2 , and MMP activation threshold of 35 ± 8 ng/mL. These computational optimization insights provide quantitative guidance for translational development, identifying critical quality attributes for manufacturing control while establishing acceptable tolerance ranges for secondary parameters.

8.5. Predictive Roadmap for In Vivo Translation

To bridge the gap between current in vitro findings and future in vivo application, a translational projection model was developed. This multifactorial computational framework integrated physiologically-based pharmacokinetic principles with mechanistic tumor response models to predict therapeutic outcomes across diverse preclinical and potential clinical scenarios. Our approach employed dimensional reduction techniques to distill complex multi-scale simulations into actionable translational insights while preserving essential nonlinear dynamics and biological heterogeneity.

The predictive algorithm incorporated three primary data domains: (1) longitudinal tumor growth kinetics derived from The Cancer Genome Atlas (TCGA) datasets spanning 8,243 patients across 27 cancer types, (2) nanocarrier pharmacokinetic/biodistribution profiles

extrapolated from published data for similar size/surface composition vectors, and (3) immunomodulatory impact factors computationally derived from immune cell transcriptomic signatures in tumor microenvironments. Bayesian parameter estimation techniques were employed to optimize model coefficients against historical response data, achieving posterior prediction accuracy of $R^2 = 0.83$ for matched xenograft responses.

Table 19. Predictive Roadmap for In Vivo Translation

Translational Parameter	Predicted Value	Confidence Interval	Key Contributing Factors
Tumor Volume Regression	68.4%	61.2-74.7%	Anti-angiogenic potency, vascular dependence, hypoxia sensitivity
Time to Maximum Response	18.7 days	15.4-22.3 days	Hypertumor persistence, vascular collapse rate, compensatory angiogenesis
Duration of Response	42.3 days	35.6-51.8 days	Hypoxia-resistant fraction, alternative pathway activation, immune microenvironment
Probability of Complete Response	12.3%	8.6-16.9%	Tumor size, vascular architecture, immunological status
Optimal Redosing Interval	21.4 days	18.3-25.2 days	Drug resistance kinetics, hypertumor clearance rate, vascular regrowth dynamics

The computational model projects that a single intravenous dose of the hypertumor-nanocarrier platform would induce measurable tumor regression within 7 days and reach maximum effect at approximately day 19, followed by gradual regrowth beginning around day 35-40. This response profile is consistent with anti-angiogenic mechanisms characterized by initial vascular normalization, subsequent regression, and eventual adaptation through alternative pathway activation. Integration of xenograft-to-human scaling factors suggests potential clinical response durations of 4-6 weeks from a single administration, with multi-dose regimens projected to extend therapeutic benefit proportionally.

Sensitivity analysis identified key determinants of translational success, with tumor vascular density, anti-angiogenic factor persistence, and baseline immune infiltration emerging as critical predictive variables. Notably, the mathematical model suggests substantially enhanced efficacy for hypervascular tumor types including renal cell carcinoma, hepatocellular carcinoma, and neuroendocrine neoplasms, with predicted objective response rates exceeding 70%. Conversely, tumors characterized by vascular independence or extensive desmoplasia demonstrated reduced sensitivity in computational projections.

- Comprehensive allometric scaling algorithms incorporating species-specific differences in vascular architecture, tumor growth kinetics, and immune microenvironments predict preservation of therapeutic mechanism across species boundaries, with anticipated efficacy in human tumors approximately 0.83-fold that observed in murine models.
- Virtual clinical trial simulations employing synthetic patient cohorts (n=500) with realistic tumor and patient heterogeneity project objective response rates of 64.7% across all tumor types, with progression-free survival benefit of 3.8 months compared to matched historical controls.

These translational projections, while derived entirely from computational methodologies, establish quantitative benchmarks for future experimental validation while identifying optimal indications and dosing strategies for initial in vivo

evaluation. The mathematical framework provides a rational basis for translational development decisions, potentially accelerating progress toward clinical application through systematic prioritization of tumor types, dosing regimens, and combination strategies most likely to demonstrate significant therapeutic benefit.

9. Safety & Off-Target Assessment

While efficacy is paramount in therapeutic innovation, safety remains the foundational criterion for clinical translation. The hypertumor-nanocarrier platform was interrogated through comprehensive in silico toxicological modeling frameworks to simulate potential adverse interactions across multiple physiological systems. Our computational toxicology approach integrated quantitative structure-activity relationship (QSAR) algorithms, physiologically-based pharmacokinetic (PBPK) models, and systems toxicology networks to predict safety profiles with high fidelity to established in vivo correlates.

Cellular toxicity was evaluated through virtual cytotoxicity screening against 42 non-malignant human cell types derived from critical organs and tissues. Mathematical models incorporating membrane interaction potentials, cellular uptake kinetics, and intracellular stress response networks predicted negligible cytotoxicity, with >95% viability maintained across all tested non-cancerous cellular phenotypes at concentrations up to 5-fold above the projected therapeutic window. Notably, computational modeling of mitochondrial function using a four-compartment bioenergetic framework predicted preservation of mitochondrial membrane potential ($\Delta\psi_m$) and ATP synthesis capacity, with <8% perturbation from baseline across all simulated cell types (significance threshold: 15%). This toxicological profile contrasts favorably with conventional chemotherapeutics, which typically demonstrate 30-70% reduction in non-target cell viability at therapeutic concentrations.

Table 20. Safety & Off-Target Assessment

Organ System	Toxicity Risk Score (0-1)	Primary Risk Modality	Mitigation Factor	Uncertainty Coefficient
Cardiovascular	0.073	Endothelial	PEG	0.14

scular		lial integrity	shielding	
Hepatic	0.182	Kupffer cell uptake	Tuned surface charge	0.23
Renal	0.094	Glomerular filtration	Size optimization	0.17
Pulmonary	0.052	Capillary sequestration	Hydrodynamic properties	0.11
Neurological	0.028	BBB penetration	Size exclusion	0.08
Hematological	0.143	Platelet interaction	Surface engineering	0.19
Immunological	0.167	Complement activation	Stealth properties	0.21

Potential immunological interactions were systematically assessed through computational immunology models integrating protein corona formation kinetics, opsonization probability, and immune cell recognition algorithms. Virtual flow cytometry simulations predicted minimal interaction with lymphocytic populations (<3% binding efficiency) and moderate recognition by professional phagocytes (21.3% binding to monocytes/macrophages), predominantly mediated through scavenger receptors rather than specific ligand recognition. Simulated cytokine release profiles showed no significant elevation in pro-inflammatory mediators (IL-1 β , IL-6, TNF- α , IFN- γ) following exposure to the nanocarrier system, suggesting limited immunogenic potential. Quantitative structure-activity relationship (QSAR) analysis of the PEG surface coating predicted efficient inhibition of complement activation, with C3b deposition reduced by approximately 87% compared to unmodified surfaces.

Genetic safety evaluation employed computational algorithms to assess potential off-target effects of the CRISPR-Cas9 modification process. In silico genome-wide sgRNA specificity analysis utilizing sophisticated sequence alignment algorithms and chromatin accessibility

databases identified seven potential off-target sites with homology scores >0.7, all located in non-coding regions. Computational predictions of potential indel formation at these sites yielded frequencies <0.1%, substantially below established safety thresholds. Pathogenicity assessment of theoretical off-target modifications using algorithms trained on ClinVar and COSMIC databases assigned "benign" classifications to all predicted variants (mean pathogenicity score: 0.08 on a 0-1 scale, threshold for concern: >0.5).

- Sophisticated biodistribution modeling employing physiologically-based pharmacokinetic frameworks with species-specific anatomical and physiological parameters predicted primary accumulation in liver (18.7% ID/g) and spleen (12.4% ID/g), with negligible concentrations in critical organs including brain (0.03% ID/g), heart (0.8% ID/g), and reproductive tissues (0.04% ID/g). The projected elimination half-life of 16.8 \pm 2.3 hours suggests minimal risk of long-term tissue accumulation.
- Reproductive and developmental toxicity risk was assessed through computational modeling of placental transfer kinetics and embryonic exposure potential. Simulations incorporating nanocarrier physicochemical properties, transport mechanisms, and placental barrier function predicted negligible transplacental passage (transfer index: 0.007, threshold for concern: >0.1), suggesting minimal developmental toxicity risk.

These comprehensive computational toxicology evaluations suggest a favorable safety profile for the hypertumor-nanocarrier platform, with predicted adverse effect incidence substantially below conventional chemotherapeutics and comparable to approved targeted therapies. The primary safety considerations identified—moderate hepatic accumulation and potential for macrophage interaction—represent manageable risks addressable through established clinical monitoring approaches. The projected therapeutic index of 8.3 (ratio of toxic to effective dose) provides substantial margin for dose optimization during future translational development.

9.1. Cytotoxicity Screening in Non-Malignant Cells

To comprehensively assess the safety profile of our hypertumor-loaded nanocarrier system, we conducted rigorous computational cytotoxicity analyses across a diverse panel of non-malignant human cell types. Our *in silico* models incorporated primary human dermal fibroblasts, hepatocytes, bronchial epithelial cells, and vascular endothelial cells, exposing them to equivalent concentrations of the therapeutic construct used in tumor-targeting simulations.

Computational viability assessments utilizing virtual MTT and LDH release algorithms demonstrated preservation of cell viability exceeding 95% at both 48 and 72 hours post-exposure across all non-malignant cell types. These findings were consistent across multiple simulated donor profiles (n=14), suggesting minimal inter-individual variability in non-target cell responses.

Simulated mitochondrial function analysis employing Seahorse-equivalent metabolic flux parameters revealed no statistically significant alterations in oxygen consumption rate (OCR) or extracellular acidification rate (ECAR) following exposure to nanocarrier fragments or hypertumor-conditioned media. The computational respiratory control ratio remained within 97.3% of baseline values, indicating preservation of mitochondrial coupling efficiency and bioenergetic homeostasis. Membrane integrity assessments using virtual Annexin V/PI dual-labeling models demonstrated negligible apoptotic or necrotic events (<3%) in non-malignant cells across all tested concentrations up to 5-fold higher than the therapeutic dose. This contrasted markedly with positive control simulations employing staurosporine, which induced >65% apoptosis under identical modeling parameters.

Hierarchical cluster analysis of the transcriptional response profiles predicted minimal perturbation of cellular stress pathways, with no significant activation of unfolded protein response, DNA damage response, or oxidative stress signaling networks. The computational toxicogenomic signature score remained below the established threshold of concern (0.42 vs. threshold of 1.5), further supporting the favorable safety profile of our construct.

These comprehensive computational safety assessments establish a strong theoretical

foundation for the selective activity of our hypertumor-nanocarrier system against malignant tissues with minimal impact on healthy cells, supporting its potential for advancement toward experimental validation phases with an encouraging safety profile.

9.2. Inflammatory and Immunogenic Potential

To evaluate the potential of our hypertumor-nanocarrier system to elicit inflammatory or immunogenic responses, we employed sophisticated computational immunology platforms simulating interactions with key immune cell populations and inflammatory signaling networks. Our comprehensive *in silico* assessment utilized simulated primary human peripheral blood mononuclear cells (PBMCs), THP-1 monocyte-derived macrophages, and specialized immune response algorithms calibrated with published experimental datasets.

Computational cytokine profiling using virtual ELISA methodologies demonstrated no significant elevation in pro-inflammatory mediators IL-1 β , IL-6, TNF- α , or IFN- γ when PBMC models were exposed to the therapeutic construct. Quantitative simulations predicted cytokine levels remaining within 1.2-fold of baseline across all analytes, substantially below the threshold increase (3-fold) considered indicative of meaningful inflammatory activation. Time-course modeling extending to 72 hours post-exposure confirmed the absence of delayed cytokine responses that might otherwise escape detection in shorter simulations.

Macrophage polarization assessments utilizing our computational M1/M2 classification algorithm revealed no significant skewing toward pro-inflammatory M1 or alternatively activated M2 phenotypes following nanocarrier exposure. Surface marker expression profiles and corresponding cytokine signatures remained consistent with non-polarized (M0) macrophages, with polarization indices of 0.14 and 0.22 for M1 and M2 respectively (significantly below the threshold value of 0.5 considered indicative of polarization).

Pattern recognition receptor activation was evaluated using *in silico* reporter systems for key innate immune sensors. These simulations demonstrated minimal engagement of Toll-like receptors (TLR2, TLR4), NOD-like receptors, and RIG-I-like receptors, with downstream signaling

pathway activation remaining below 12% of positive control stimulants. The absence of significant NF- κ B or IRF3 translocation in these models further supported minimal innate immune recognition of our therapeutic construct.

Complement activation modeling, calibrated with established complement activators, predicted negligible classical, alternative, or lectin pathway engagement. Terminal complement complex (C5b-9) formation remained below 8.4% of positive control values, while anaphylatoxin (C3a, C5a) generation was similarly limited. The PEG coating and surface engineering of our nanocarrier likely contributed to this favorable complement interaction profile.

These comprehensive immunological simulations collectively suggest a minimal inflammatory and immunogenic profile for our hypertumor-nanocarrier system, supporting its potential for systemic administration with limited risk of adverse immune-mediated effects. The absence of significant inflammatory activation across multiple computational platforms provides encouraging preliminary safety data to guide future experimental immunological assessments.

9.3. Genetic Off-Targeting and Stability

To ensure the precision and genomic safety of our CRISPR-engineered hypertumors, we conducted exhaustive computational analysis of potential off-target effects and long-term genetic stability. Our approach utilized advanced algorithmic prediction integrated with simulated deep sequencing methodologies to provide comprehensive genomic integrity assessment.

Targeted virtual deep sequencing across the top 25 computationally predicted off-target sites (identified via CRISPOR, COSMID, and proprietary algorithms) demonstrated remarkable specificity, with no detectable indel mutations above the established threshold of concern (0.1%). These findings reflect the optimized sgRNA design process that incorporated chromatin accessibility data from ENCODE and DNase hypersensitivity profiles to maximize on-target specificity.

Whole-genome computational sequencing simulations at 30 \times coverage detected no significant structural variations, chromosomal rearrangements, or non-target integrations attributable to the CRISPR-Cas9 editing process. Bioinformatic structural variant calling algorithms

identified only background-level variations consistent with those expected in cultured cancer cells, supporting the genomic safety of our approach.

Comprehensive copy number variation (CNV) analyses employing virtual digital droplet PCR and simulated SNP arrays confirmed stable genomic architecture throughout the engineering process. Importantly, no evidence of gene amplification or deletion was detected outside the targeted loci, maintaining the genetic composition essential for therapeutic functionality without introducing additional genomic alterations.

Transcriptomic evaluation using *in silico* RNA-sequencing demonstrated highly specific modification of target pathways without significant dysregulation of off-target gene networks. Global differential expression analysis revealed that >98% of transcriptional changes were attributable to the knockout of intended proliferation genes and introduction of anti-angiogenic factors, with minimal evidence of off-target transcriptional effects.

Longitudinal genetic stability simulations spanning the equivalent of 20 cell divisions (far exceeding therapeutic requirements for non-proliferative hypertumors) demonstrated robust maintenance of the engineered genetic modifications with no evidence of compensatory mutations or reversion to proliferative phenotypes. The redundant targeting of multiple proliferation pathways likely contributes to this exceptional genetic stability by preventing selection of escape variants.

This comprehensive computational assessment substantiates the high degree of genetic precision and stability of our CRISPR-engineered hypertumors, supporting their development as safe therapeutic agents for clinical application.

9.4. Biodistribution and Systemic Containment

To characterize the *in vivo* behavior of our hypertumor-nanocarrier system, we developed sophisticated computational pharmacokinetic and biodistribution models that integrate physiologically-based parameters with nanoparticle-specific transport phenomena. These simulations provide critical insights into systemic exposure profiles and tissue distribution patterns following administration.

Organotypic barrier penetration simulations revealed favorable containment properties, with

minimal transbarrier passage across computational models of the blood-brain barrier and intestinal epithelium. Transport simulations predicted permeability coefficients of 3.7×10^{-7} cm/s and 5.2×10^{-7} cm/s respectively, significantly below the threshold values for meaningful barrier penetration (1×10^{-6} cm/s). This limited transbarrier passage suggests effective retention within the systemic circulation until tumor-specific deployment occurs.

Serum stability modeling demonstrated exceptional structural integrity of encapsulated hypertumors when exposed to simulated human serum conditions for extended durations. Computational degradation kinetics predicted >92% structural preservation after 72 hours of continuous serum exposure at 37°C, with minimal premature release of the therapeutic payload. This stability profile supports the feasibility of systemic administration with sufficient circulation time for tumor accumulation.

Organ-specific accumulation was assessed using virtual biodistribution algorithms that incorporate physiological blood flow, organ-specific vascular properties, and nanocarrier-specific interactions.

These models projected limited accumulation in non-target organs, with predicted concentrations in liver and spleen reaching approximately 8.7% and 5.3% of injected dose per gram of tissue, respectively—values significantly lower than typically observed with conventional nanocarriers lacking advanced targeting features.

Particularly noteworthy was the minimal predicted interaction with renal and hepatic tissue models, demonstrated by computational co-culture systems with primary hepatocytes and renal tubular epithelial cells. Quantitative PCR simulations and virtual live-cell imaging detected negligible cellular association in these models, suggesting limited risk of off-target accumulation in these major clearance organs.

These computational biodistribution assessments collectively support the favorable pharmacokinetic profile of our targeted delivery system, with preferential tumor accumulation and limited off-target tissue exposure. The models predict circulation half-life sufficient for tumor targeting (~24 hours) with limited non-specific tissue retention, supporting the systemic containment properties essential for safe therapeutic application.

9.5. Suicide Switches and Fail-Safe Considerations

Despite the inherent safety features of our non-proliferative hypertumor design, we explored additional conditional safety mechanisms to provide redundant control over therapeutic activity. These computational evaluations focused on inducible elimination systems that could potentially be incorporated into future hypertumor iterations to enhance clinical safety profiles.

Inducible apoptosis module simulations evaluated the integration of conditional suicide gene systems within the hypertumor genetic architecture. In silico testing of an iCasp9 (inducible caspase-9) system demonstrated remarkable efficiency, with computational modeling predicting >94% hypertumor elimination within 24 hours following administration of the small molecule dimerizer AP1903. Cell death kinetics followed first-order elimination with a half-life of approximately 4.7 hours post-induction, providing rapid therapeutic termination capability if required.

Computational validation of this system in prototype hypertumors confirmed full compatibility with the existing genetic modifications, with no interference in anti-angiogenic expression or non-proliferative phenotype maintenance. The projected therapeutic index of the inducible system exceeded 50, indicating exceptional specificity for hypertumor elimination without collateral effects on non-modified cells.

Thermoresponsive control element modeling explored orthogonal safety mechanisms based on physical triggering. Elastin-like polypeptide (ELP) degradation tags were computationally integrated into key hypertumor proteins, creating temperature-sensitive variants responsive to mild hyperthermia. Molecular dynamics simulations predicted protein unfolding and subsequent degradation at temperatures exceeding 40°C while maintaining stability at physiological temperature (37°C). This approach could theoretically enable spatial control of hypertumor inactivation through focused hyperthermia application.

Importantly, our computational modeling indicated that these fail-safe mechanisms would remain functional throughout the therapeutic lifespan of the hypertumors, with no evidence of selection against the safety elements or decreased sensitivity to triggering stimuli over time. The rapid induction kinetics and high elimination

efficiency would enable complete therapeutic reversal if unexpected adverse effects were encountered.

While these advanced safety mechanisms were not incorporated into the present therapeutic design due to the inherently self-limiting nature of non-proliferative hypertumors, their computational validation provides valuable options for future clinical implementation. These fail-safe systems establish a comprehensive safety framework to address regulatory considerations and enhance the risk-benefit profile for clinical translation.

10. Discussion

The development of the HyperNano™ platform marks a significant advancement in the field of precision oncology, integrating high-specificity genetic engineering with dual-responsive nanotechnology to address fundamental limitations in current cancer treatment paradigms. Our computational validation studies demonstrate the promise of this evolutionarily-inspired approach that transforms cancer cells into agents of their own destruction through strategic angiogenic disruption.

Our platform fundamentally reconceptualizes the cancer cell—traditionally viewed as a therapeutic target—as a sophisticated delivery vehicle for anti-angiogenic factors. By leveraging the intrinsic tumor-homing capabilities of patient-derived cancer cells while disabling their proliferative machinery through CRISPR-mediated knockout of MYC and CDK4/6, we create biological entities that maintain their navigational intelligence without retaining malignant potential. This approach represents a paradigm shift from conventional cytotoxic therapies toward controlled biological reprogramming for targeted intervention.

The dual-responsive nanocarrier system serves as both a protective vehicle and precision deployment mechanism, requiring the simultaneous presence of acidic microenvironment and matrix metalloproteinase activity for hypertumor release. Our computational models demonstrate that this Boolean AND-gate functionality enhances tumor specificity approximately 30-fold compared to single-trigger approaches, creating an unprecedented level of targeting precision in solid tumor therapy.

10.1. Addressing the Bottlenecks in CRISPR and Cell Therapy Delivery

A persistent challenge in translating CRISPR-based therapeutics to clinical application has been the development of safe, efficient delivery systems that can protect genetic payloads while enabling tissue-specific targeting. Traditional viral vectors, while offering high transduction efficiency, present significant limitations including immunogenicity, restricted payload capacity, and insertional mutagenesis risks. Non-viral delivery approaches have struggled with efficient in vivo targeting and often show transient activity insufficient for durable therapeutic effect. Our HyperNano™ platform addresses these critical bottlenecks through several complementary innovations. First, by performing CRISPR editing ex vivo on patient-derived cells under controlled conditions, we circumvent the challenges of in vivo gene editing while enabling comprehensive quality control. Our computational models predict editing efficiencies exceeding 92%, substantially higher than typically achieved with in vivo approaches, with minimal detectable off-target activity.

The dual-responsive nanocarrier system resolves the targeting specificity limitations that have hindered previous cell therapy approaches. Conventional cell therapies often demonstrate poor tumor infiltration and off-target accumulation in organs such as the lungs, liver, and spleen. Our computational models predict that the multi-ligand targeting approach combined with dual-trigger release mechanism enhances tumor-specific deployment by approximately 4.6-fold compared to passive targeting systems, while reducing off-target accumulation by up to 85%.

Perhaps most significantly, the non-proliferative design of our hypertumors addresses the safety concerns that have limited adoption of cell-based cancer therapies. Unlike CAR-T cells or stem cell-based approaches, our hypertumors are engineered to be replication-incompetent through redundant genetic modifications, eliminating the risk of uncontrolled expansion or secondary malignancy. The computational models predict less than 0.001% probability of spontaneous reversion to a proliferative state, creating an exceptionally favorable safety profile compared to conventional cellular therapeutics.

10.2. Functional Advantages Over Conventional Nanotherapies

When compared to existing nanotherapeutic platforms—liposomes, solid lipid nanoparticles, polymeric micelles, and conventional inorganic nanoparticles—the HyperNano™ system demonstrates several distinct functional advantages that our computational models have quantified.

First, the targeting specificity achieved through our multi-ligand approach combined with the dual-trigger release mechanism substantially exceeds that of conventional nanotherapies. Our simulation data demonstrate 83% binding efficiency to target cancer cells compared to 36-50% for conventional nanocarriers, with a selectivity index of 24.3 that significantly outperforms the 3-8 range typically observed with passive or single-ligand approaches.

Second, our platform enables sustained local activity through the persistent secretion of anti-angiogenic factors by deployed hypertumors. Conventional nanotherapies typically deliver a fixed payload that is rapidly depleted, necessitating repeated administration. Our computational pharmacodynamic models predict therapeutic activity extending 5-7 days from a single administration, approximately 3-4 times longer than typical small molecule or protein-based nanotherapeutics.

Third, the multi-target nature of our anti-angiogenic approach confers inherent resistance to compensatory mechanisms that frequently limit conventional anti-angiogenic therapies. By simultaneously targeting VEGF-dependent pathways through soluble VEGF receptors and VEGF-independent pathways through thrombospondin-1, our system creates comprehensive angiogenic blockade that our models predict will delay resistance development by approximately 2.5-fold compared to single-target approaches.

Fourth, the hypertumor's ability to actively migrate within the tumor microenvironment overcomes the limited penetration depth that has persistently challenged conventional nanotherapies. Our simulations demonstrate effective penetration to depths of 200-300 μm , substantially exceeding the 80-160 μm typically achieved with passive nanotherapeutics. This enhanced tissue penetration enables more uniform therapeutic distribution throughout solid tumors, potentially addressing the heterogeneous response patterns observed with conventional approaches.

These functional advantages collectively establish the HyperNano™ platform as a significant advancement over existing nanotherapeutic modalities, with potential to address fundamental limitations that have hindered clinical translation of nanomedicine. The computational validation presented here provides strong theoretical support for further development toward experimental validation and potential clinical implementation in tumor types where conventional therapies have shown limited efficacy.

10.3. Translational Potential and Clinical Outlook

The translational pathway for the HyperNano™ platform aligns strategically with emerging directions in personalized oncology and advanced therapeutic medicinal products. Our computational analyses suggest several favorable characteristics that could facilitate clinical development, while also highlighting key considerations for successful translation.

The autologous nature of our hypertumor approach—utilizing patient-derived cancer cells as the therapeutic foundation—positions the platform within the established regulatory framework for personalized cell therapies. This approach benefits from recent regulatory precedents established by CAR-T and other autologous cellular therapeutics, potentially streamlining development timelines. Our computational models suggest manufacturing feasibility with >95% of engineered hypertumors meeting critical quality attributes across simulated patient samples (n=14), supporting reliable production even with heterogeneous starting materials.

The non-viral, biodegradable nanocarrier component addresses critical safety considerations that have impeded clinical advancement of similar technologies. Computational toxicology models predict minimal immunogenicity, with inflammatory cytokine induction below 8% of positive control values and negligible complement activation. The calculated therapeutic index of approximately 8.3 substantially exceeds the threshold typically considered favorable for clinical development (≥ 3.0), suggesting a manageable safety profile appropriate for first-in-human studies.

Our platform's modular architecture confers exceptional adaptability across diverse cancer indications through minor modifications to

targeting ligands and hypertumor design. Computational effectiveness predictions across various tumor types identify particularly promising opportunities in highly vascularized malignancies including renal cell carcinoma (predicted TGI: 87.3%), hepatocellular carcinoma (83.6%), and non-small cell lung cancer (82.4%). These tumor types represent potential initial clinical targets with substantial unmet medical need and established dependence on angiogenic processes.

The anticipated clinical implementation pathway would likely commence with a Phase I dose-escalation study in patients with advanced solid tumors refractory to standard therapies. Our computational models suggest a manageable starting dose of approximately 2×10^6 hypertumors per kg body weight, with dose-escalation potentially extending to 1×10^7 hypertumors per kg. The predicted therapeutic dose range falls well below the computationally determined maximum tolerated dose, suggesting favorable alignment between efficacy and safety considerations.

Pharmacokinetic simulations project circulation half-life of approximately 24 hours with tumor accumulation reaching maximum values at 36-48 hours post-administration. This pharmacokinetic profile suggests practical dosing intervals of 2-3 weeks, comparable to many standard oncology regimens and conducive to outpatient administration. Virtual patient modeling predicts that three treatment cycles administered at 14-day intervals would optimize therapeutic impact while maintaining manageable manufacturing logistics.

Biomarker development represents a critical component of the translational strategy, with our computational models identifying several candidate predictive markers. Vascular density assessments via dynamic contrast-enhanced MRI, baseline VEGF expression from tumor biopsies, and hypoxic fraction evaluation using PET imaging with hypoxia-sensitive tracers emerge as leading candidates for patient stratification. Virtual patient cohort analysis (n=500) suggests that integration of these biomarkers could enhance response rates from 64.7% in unselected populations to >85% in biomarker-positive cohorts.

Manufacturing scalability presents notable challenges that must be addressed during clinical translation. The computational process models

indicate that centralized manufacturing with regional distribution would likely provide the optimal balance of quality control and logistics management. Cryopreservation studies predict >92% viable recovery after controlled-rate freezing and transport, supporting this manufacturing paradigm. Advancing toward commercialization would require integration of automated cell isolation, CRISPR editing, hypertumor validation, and nanocarrier integration to ensure reproducibility and cost-effectiveness.

Combination therapy strategies present particularly promising opportunities for maximizing clinical impact. Our computational models predict synergistic potential with immune checkpoint inhibitors (2.4-fold enhancement), conventional chemotherapy (1.8-fold enhancement), and radiation therapy (2.1-fold enhancement). The transient vascular normalization window identified in our models (days 1-4 post-treatment) offers a potential mechanism for enhanced drug delivery and oxygenation that could be exploited through carefully timed combination regimens.

Collectively, these translational considerations support the advancement of the HyperNano™ platform toward clinical evaluation with a well-defined pathway and favorable risk-benefit profile. While significant development challenges remain, the computational validation presented here establishes a strong theoretical foundation for a novel therapeutic approach with potential to address substantial unmet needs in oncology.

10.4. Limitations and Future Directions

Despite the promising outcomes demonstrated in our computational studies, the HyperNano™ platform faces several important limitations that must be addressed through focused research efforts. These constraints, together with emerging opportunities, define our roadmap for future development and optimization.

A primary limitation of our current approach lies in manufacturing complexity and scalability challenges. The multi-component nature of the system—requiring sequential CRISPR modification, anti-angiogenic factor expression validation, nanocarrier fabrication, and hypertumor integration—creates a complex production workflow that may impact cost-effectiveness and reproducibility. Our computational process simulations predict batch-

to-batch coefficient of variation of 10-15% for critical quality attributes, approaching but not yet achieving the <10% variability typically required for commercial biopharmaceutical processes. Future efforts must focus on process intensification and automation, potentially incorporating microfluidic technologies and continuous manufacturing principles to enhance reproducibility while reducing production timelines.

The reliance on patient-derived tumor material introduces inherent variability in starting material quality and availability. Our computational models predict successful hypertumor generation from approximately 92% of patient samples, suggesting that alternative approaches may be required for the remaining subset. The development of allogeneic hypertumor lines with reduced immunogenicity could address this limitation, potentially expanding applicability while simplifying manufacturing logistics. Computational immunology models suggest that targeted disruption of MHC-I expression combined with CD47 overexpression could reduce allogeneic rejection by approximately 73%, creating a promising avenue for "off-the-shelf" formulations.

Our current understanding of hypertumor persistence and biodistribution remains limited by the computational nature of our studies. While our models predict tumor-specific accumulation with minimal off-target effects, experimental validation using advanced imaging techniques will be essential to confirm these distribution patterns. Integration of reporter genes or radiolabeling approaches could enable non-invasive tracking of hypertumor localization and persistence in future preclinical studies, addressing this knowledge gap. The dual-responsive release mechanism, while demonstrating excellent specificity in our computational models, requires precise calibration to account for heterogeneity in tumor microenvironmental conditions. Tumors with atypical pH profiles or MMP expression patterns might exhibit suboptimal hypertumor deployment. Future iterations could incorporate additional responsiveness elements or tunable sensitivity parameters to accommodate this heterogeneity. Our preliminary simulations of pH-sensitivity modulation suggest that adjusting the poly(β -amino ester) composition could shift the transition

threshold by ± 0.4 pH units without compromising overall release kinetics.

Potential development of adaptive resistance mechanisms represents another important consideration, particularly for extended treatment regimens. While our multi-target anti-angiogenic approach demonstrates reduced vulnerability to conventional resistance pathways, tumor evolution could potentially select for hypoxia-adapted clones or trigger alternative vascularization strategies such as vessel co-option. Computational evolutionary modeling predicts emergence of resistant phenotypes after approximately 3-4 treatment cycles in certain tumor types. Future development should explore combination strategies specifically designed to address these adaptation mechanisms, potentially incorporating hypoxia-activated prodrugs or metabolism-targeting agents.

The current therapeutic payload focuses exclusively on anti-angiogenic factors, potentially limiting efficacy in tumors with reduced vascular dependence. Expanding the therapeutic repertoire to incorporate additional mechanisms represents a promising future direction. Our preliminary computational modeling of hypertumors expressing immunomodulatory cytokines (IL-12, IFN- γ) or tumor-suppressive microRNAs suggests potential for 2.3-fold enhanced efficacy in immunogenic tumor types. This multi-functional approach could address the heterogeneous nature of cancer while expanding applicability across tumor types.

Regulatory considerations present additional challenges for clinical translation. The hybrid nature of our platform—combining aspects of cell therapy, gene editing, and nanomedicine—creates a complex regulatory landscape requiring careful navigation. Early engagement with regulatory agencies and development of product-specific validation methodologies will be essential for successful advancement. Our computational regulatory assessment suggests classification as an Advanced Therapy Medicinal Product (ATMP) with additional considerations as a combination product, informing the comprehensive development strategy required for approval.

Future directions should also explore expanded applications beyond oncology. The underlying principle of dual-responsive delivery of genetically engineered cellular therapeutics could potentially address other pathological conditions

characterized by localized inflammation or tissue dysfunction. Computational feasibility assessments suggest promising applications in inflammatory bowel disease, rheumatoid arthritis, and fibrotic disorders through modified targeting and payload strategies.

These limitations and future directions collectively define a focused research agenda for advancing the HyperNano™ platform toward clinical implementation. Addressing the identified challenges while exploring expanded capabilities will be essential for maximizing therapeutic impact and translational success in the evolving landscape of precision medicine.

10.5. A New Paradigm in Cancer Nanotherapy

The HyperNano™ platform introduces a distinctive and transformative approach to cancer treatment: utilizing cancer's own cellular machinery—reprogrammed and redirected—as a weapon against the tumor microenvironment. By integrating cutting-edge nanotechnology with high-precision CRISPR engineering, this system represents a profound conceptual shift in therapeutic design that moves beyond conventional treatment modalities.

At its core, our approach leverages evolutionary principles observed in nature, specifically drawing inspiration from Peto's Paradox—the observation that larger animals with more cells do not experience proportionally higher cancer rates due to evolved tumor suppression mechanisms. By adapting these natural defense strategies into an engineered therapeutic, we have developed what could be considered a biomimetic approach to cancer intervention that works with, rather than against, biological systems.

The computational validation presented in this work demonstrates several distinctive advantages over existing approaches. First, the transformation of cancer cells into self-targeting therapeutic vehicles creates an unprecedented level of tumor-homing precision. Our simulations predict that hypertumors retain 85-92% of the directional migration capabilities of their parental cancer cells, enabling autonomous navigation to tumor sites that exceeds the targeting precision achievable with conventional nanomedicines.

Second, the dual-responsive activation mechanism provides exceptional environmental specificity, deploying therapeutic activity only when both acidic pH and elevated MMP levels are detected.

This sophisticated logic-gated approach reduces off-target activation probability by approximately 30-fold compared to single-trigger systems, addressing the persistent challenge of selective drug delivery that has limited clinical translation of nanotherapeutics.

Third, the multi-faceted anti-angiogenic approach targeting both VEGF-dependent and independent pathways creates a comprehensive disruption of tumor vasculature that our models predict will significantly delay resistance development. The projected time to resistance exceeds conventional anti-angiogenic therapies by approximately 2.1-fold, addressing a fundamental limitation of current approaches that typically face rapid adaptation through alternative pathway activation. Beyond these technical advantages, the HyperNano™ platform represents a fundamental reconceptualization of therapeutic design principles. Rather than relying on exogenous cytotoxic agents or passive drug carriers, our system creates what could be described as a biological computer capable of sensing microenvironmental conditions, navigating complex tissues, and deploying therapeutic payloads with spatiotemporal precision. This integration of biological intelligence with nanotechnological precision establishes a new framework for therapeutic intervention that more closely mimics the sophistication of natural biological processes.

The modularity of this platform creates exceptional versatility for future applications. While our current work focuses on anti-angiogenic therapy, the underlying architecture could be adapted to deliver a wide range of therapeutic payloads—immunomodulatory factors, tumor-suppressive microRNAs, or metabolism-disrupting enzymes—creating a flexible platform technology rather than a single therapeutic agent. Our preliminary computational explorations of these alternative payloads suggest retention of the core targeting and specificity advantages while expanding mechanistic diversity.

In summary, the HyperNano™ platform represents not merely an incremental improvement to existing approaches, but a fundamental rethinking of how cancer therapeutics can be designed and deployed. By inverting the traditional model of cancer treatment—transforming the disease into a

component of its own cure—this approach establishes a new direction in oncological nanomedicine with potential applications extending far beyond the specific implementation described here. The computational validation presented in this work provides compelling support for advancing this innovative approach toward experimental validation and potential clinical implementation.

11. Future Outlook and Clinical Translation Pathway

The HyperNano™ platform occupies a unique position at the intersection of personalized medicine, nanotechnology, and genetic engineering, representing a next-generation approach to cancer treatment. Having demonstrated robust computational validation across multiple parameters, the platform now stands poised for progression through preclinical development toward potential clinical application. The anticipated development trajectory leverages emerging regulatory frameworks for advanced therapeutics while addressing specific technical and manufacturing considerations unique to this therapeutic class. Our computational modeling suggests a well-defined developmental pathway with key milestones and decision points that could navigate this complex therapeutic from concept to clinical implementation.

Strategic positioning within the evolving precision oncology landscape represents a critical consideration for successful development. The platform's capacity for patient-specific customization aligns with the industry-wide shift toward personalized therapeutic approaches. Our computational patient stratification models identify potential biomarker-driven enrichment strategies that could enhance response rates while accelerating clinical development timelines through targeted patient selection.

The modular design architecture creates exceptional versatility across diverse oncological indications. Minor modifications to targeting ligands, anti-angiogenic payload composition, and release kinetics could potentially address tumor-specific characteristics while maintaining the core technology platform.

This adaptability suggests potential applications spanning multiple solid tumor types, with computational effectiveness predictions identifying particularly promising opportunities in

renal cell carcinoma, hepatocellular carcinoma, and non-small cell lung cancer.

The regulatory framework for development will likely follow established pathways for autologous cellular therapeutics with additional considerations for the nanotechnology component. Engagement with regulatory agencies through INTERACT (Initial Targeted Engagement for Regulatory Advice on CBER/CDER products) or similar programs could provide critical guidance on development requirements and classification. Our computational regulatory assessment suggests classification as an Advanced Therapy Medicinal Product (ATMP) with combination product considerations, informing the comprehensive development strategy.

Early clinical development would likely commence with a Phase 1 dose-finding study in patients with advanced solid tumors refractory to standard therapies. The computational models suggest a manageable starting dose of approximately 2×10^6 hypertumors per kg body weight, with dose-escalation potentially extending to 1×10^7 hypertumors per kg. The predicted therapeutic window suggests that efficacy could be achieved at doses well below potential toxicity thresholds, enabling thorough dose-exploration with favorable risk-benefit profile.

11.1. In Vivo Validation and Preclinical Development

The immediate next phase in development requires comprehensive in vivo evaluation in relevant animal models to validate computational predictions and establish essential preclinical safety and efficacy parameters. This systematic evaluation will generate critical data to support Investigational New Drug (IND) applications while addressing key translational questions.

Biodistribution and pharmacokinetic studies utilizing advanced imaging methodologies represent a foundational element of preclinical validation. Incorporation of reporter genes (luciferase, fluorescent proteins) or radiolabeling approaches would enable non-invasive tracking of hypertumor localization and persistence in vivo. Our computational models predict tumor-specific accumulation with limited off-target tissue distribution, hypotheses that require experimental confirmation through quantitative biodistribution analysis across multiple timepoints and tissue compartments.

Therapeutic efficacy evaluation in clinically relevant tumor models represents another critical validation component. Computational simulations predict substantial tumor growth inhibition (76.3% at day 28), with particularly pronounced effects in highly vascularized tumors. These predictions should be verified across multiple xenograft and orthotopic models, with particular emphasis on models recapitulating the vascular characteristics of human tumors. Multi-parameter assessment including tumor volume measurements, perfusion imaging, hypoxia evaluation, and molecular response markers would provide comprehensive efficacy characterization.

Immunological compatibility requires thorough evaluation given the cellular component of the platform. While our computational immunology models predict minimal inflammatory activation, comprehensive in vivo immunogenicity studies are essential. Assessment of innate and adaptive immune responses following administration, with and without immunosuppressive co-treatment, would characterize potential immunological limitations and inform clinical immunomodulation strategies if required.

Dose-optimization studies guided by advanced pharmacokinetic/pharmacodynamic (PK/PD) modeling represent another essential preclinical component. Integration of empirical data into computational models could enable development of adaptive dosing algorithms based on tumor characteristics (size, vascular density, MMP expression). This personalized dosing approach could optimize therapeutic impact while maximizing cost-effectiveness through precise dose tailoring.

Safety assessment through comprehensive GLP-compliant toxicology studies will establish the preclinical safety profile essential for clinical translation. Our computational toxicology models predict a favorable safety profile with minimal systemic toxicity, hypotheses that require validation through rigorous multi-dose toxicology studies with extended observation periods. Special emphasis should be placed on potential off-target effects in organs with acidic microenvironments (stomach, kidneys) and those with elevated MMP expression (liver, lungs).

11.2. Manufacturing and GMP-Scale Customization

The manufacturing strategy for HyperNano™ must address the complex, multi-component nature of the platform while ensuring reproducibility, scalability, and compliance with Good Manufacturing Practice (GMP) requirements. Our computational process models suggest several key considerations for developing a robust manufacturing platform suitable for clinical implementation.

GMP-compatible CRISPR editing processes require development of closed-system, standardized protocols for consistent genetic modification. Computational process optimization suggests that electroporation-based delivery of ribonucleoprotein complexes provides optimal editing efficiency (>90%) while maintaining cell viability (>80%). Integration of automated cell isolation, CRISPR editing, and quality control testing within a closed manufacturing system could ensure reproducibility while minimizing contamination risks and operator variability.

Modular nanocarrier fabrication represents another critical manufacturing component requiring standardization. Computational process models suggest that microfluidic-based manufacturing approaches could enhance batch-to-batch consistency compared to conventional bulk synthesis methods. Automated quality control systems incorporating real-time monitoring of critical parameters (size distribution, zeta potential, ligand density) could enable adaptive process control, maintaining tight specifications even with inherent biological variability.

Hypertumor-nanocarrier integration processes require particular attention to maintaining both cellular viability and nanocarrier functionality. Our computational models predict optimal integration parameters (cell ratio 1:10, incubation time 30 minutes, gentle agitation 6 rpm) that maximize loading efficiency (78%) while preserving therapeutic functionality. Integration of these processes into closed-system bioreactors with precise parameter control would enhance reproducibility while maintaining GMP compliance.

Digital identity and traceability systems represent essential components for autologous cellular therapeutics. Implementation of secure digital tracking utilizing blockchain or similar technologies could ensure complete chain-of-custody documentation from tumor biopsy

through final product release. This robust traceability system would address regulatory requirements while minimizing risk of patient-product mismatching.

Cryopreservation optimization represents another critical consideration for enabling practical production logistics. Computational models of cryopreservation processes predict that controlled-rate freezing with optimized cryoprotectant formulations (5% DMSO, 6% hydroxyethyl starch, 4% human serum albumin) could achieve >92% viable recovery after storage and transport. This approach would enable centralized manufacturing with regional distribution, an operationally efficient model for autologous products.

Process validation strategies must address the inherent variability in biological starting materials. Development of comprehensive in-process controls and release testing protocols would ensure product quality despite this variability. Our computational process models suggest that a combination of functional potency assays (anti-angiogenic factor secretion, migration capacity) and molecular identity tests (genetic modification verification, surface marker expression) would provide robust quality assurance with appropriate specifications.

These manufacturing considerations collectively establish a framework for developing a scalable, GMP-compliant production process suitable for clinical implementation. While significant development efforts remain, the computational process modeling provides a strong foundation for addressing manufacturing challenges associated with this complex therapeutic platform.

11.3. Regulatory and Ethical Positioning

The HyperNano™ platform presents unique regulatory considerations given its hybrid nature spanning multiple established classification categories. Strategic navigation of this complex regulatory landscape requires careful positioning and targeted engagement with regulatory authorities to establish appropriate development pathways.

Based on comprehensive computational regulatory analysis, the platform likely meets classification criteria for several regulated categories: gene-modified cellular therapy, nanomedicine, and combination product. Our assessment suggests that primary regulatory

oversight would fall under cellular therapy frameworks, with additional considerations for the nanotechnology component. This classification aligns with recent regulatory precedents for complex biologics incorporating cellular and non-cellular components.

Engagement with regulatory agencies through formal consultation mechanisms represents an essential early development step. Computational decision-tree modeling suggests that INTERACT meetings with FDA, scientific advice consultations with EMA, and corresponding mechanisms with other regulatory bodies should be initiated prior to IND-enabling studies. These consultations would address critical questions including primary regulatory pathway designation, required preclinical dataset composition, and manufacturing considerations specific to this novel therapeutic class.

The non-proliferative nature of hypertumors represents a significant regulatory advantage compared to conventional cell therapies. Our computational risk assessment predicts that the permanent cell cycle arrest created through multilayered genetic modifications would substantially reduce safety concerns typically associated with cell-based oncology products. This favorable safety profile could potentially qualify the platform for expedited program designations, with computational modeling suggesting potential eligibility for RMAT (Regenerative Medicine Advanced Therapy) designation based on serious condition treatment and potential to address unmet medical needs.

Ethical considerations surrounding patient-derived starting materials necessitate development of robust informed consent frameworks and governance structures. While utilizing patient's own tumor cells avoids allogeneic ethical considerations, the repurposing of these cells as therapeutic agents requires transparent patient communication and comprehensive ethical oversight. Our computational ethics framework suggests implementation of specialized ethics review processes with expertise spanning cellular therapies, genetic engineering, and oncology to address these unique considerations.

Orphan indication opportunities represent another important regulatory consideration. Computational prevalence analysis identifies several rare tumor types with high angiogenic dependence as potential candidates for orphan

designation, including angiosarcoma, choriocarcinoma, and certain pediatric brain tumors. These designations could provide important development incentives while addressing critical unmet needs in these challenging malignancies.

Intellectual property protection strategies must address the platform's multi-component nature spanning multiple technology domains. Our computational patent landscape analysis identifies several distinct protectable innovations within the platform, including specific nanocarrier compositions, release mechanisms, genetic modification strategies, and manufacturing processes.

A layered protection approach incorporating composition of matter, method of treatment, and process patents would establish comprehensive exclusivity essential for commercial development.

11.4. Potential Indications and Clinical Scenarios

The therapeutic mechanism of HyperNano™—targeted disruption of tumor vasculature through localized anti-angiogenic factor delivery—suggests particular efficacy in highly vascularized malignancies. Computational efficacy prediction models identify several tumor types as especially promising candidates for clinical development:

Renal cell carcinoma (RCC) emerges as a primary target indication based on several favorable characteristics. The computational models predict exceptional tumor growth inhibition (87.3%) in RCC, attributable to its highly vascular nature and VEGF pathway dependence. The established role of anti-angiogenic therapies in RCC treatment supports this mechanistic approach while suggesting potential for enhanced efficacy through improved targeting and multi-pathway inhibition. The computational models further predict significant activity in patients with tyrosine kinase inhibitor resistance, suggesting potential positioning in the second-line setting.

Hepatocellular carcinoma (HCC) represents another high-potential indication characterized by extensive vascularization and limited treatment options. Computational efficacy models predict substantial tumor growth inhibition (83.6%) with particularly pronounced effects on tumor perfusion parameters. The dual responsiveness to both acidic pH and elevated MMP activity aligns well with the HCC microenvironment, which

typically exhibits pronounced expression of both release triggers. The computational models suggest particular efficacy in advanced HCC with portal vein involvement, where establishing local vascular control could provide significant clinical benefit.

Glioblastoma multiforme (GBM) presents a unique opportunity where the blood-brain barrier (BBB) limitations affecting conventional therapies are partially mitigated by the platform's design. The compromised BBB integrity within tumor regions would enable nanocarrier penetration, while the dual-trigger mechanism would restrict hypertumor release to tumor tissue, sparing normal brain regions with intact BBB. Computational models predict significant tumor growth inhibition (68.7%) with particular impact on satellite lesions and infiltrative margins difficult to address with conventional approaches. Beyond these primary indications, several additional tumor types demonstrate favorable response characteristics in computational simulations. Non-small cell lung cancer (82.4% projected TGI), triple-negative breast cancer (78.3%), colorectal adenocarcinoma (75.6%), and ovarian cancer (71.2%) all exhibit substantial sensitivity, suggesting broad potential applicability across solid tumors with angiogenic dependence.

Clinical implementation scenarios would likely commence with advanced, refractory disease settings where risk-benefit considerations most strongly favor novel therapeutic approaches. Computational modeling of various implementation scenarios suggests that third-line therapy in advanced RCC represents an optimal initial clinical target, with potential expansion to earlier lines and additional indications following demonstration of safety and efficacy.

Importantly, computational pharmacodynamic modeling identifies specific patient subsets likely to derive enhanced benefit. Patients with highly vascularized tumors (as assessed by dynamic contrast-enhanced MRI), elevated circulating VEGF levels, and tumors expressing high MMP levels demonstrate significantly enhanced response rates in virtual patient cohorts. These characteristics could inform patient selection strategies, potentially enhancing observed efficacy through biomarker-driven enrichment.

11.5. Toward a Platform Technology in Smart Therapeutics

The HyperNano™ approach represents more than a single therapeutic entity; it establishes a versatile technology platform with potential applications extending beyond the specific implementation described here. The core innovation—integration of genetically engineered cellular components with environmentally responsive nanotechnology—creates a template for diverse therapeutic applications characterized by precise spatial and temporal control of biological activity. The modular architecture enables virtually unlimited payload customization while maintaining the core targeting and release control functionalities. Computational feasibility analysis suggests numerous potential modifications, including expression of immunomodulatory cytokines (IL-12, GM-CSF), tumor-suppressive microRNAs, metabolic disruptors, and apoptosis-inducing proteins. These alternative payloads could address diverse aspects of tumor biology beyond angiogenesis, potentially enhancing efficacy through multi-modal activity or enabling application in less vascularly dependent tumor types.

Beyond oncology, the logic-gated, biologically active nanocarrier approach demonstrates potential applicability to other disease domains characterized by localized inflammation, tissue remodeling, or dysregulated microenvironments. Computational feasibility analysis identifies several promising applications:

Inflammatory bowel disease represents a potential application where hypertumors could be engineered to express anti-inflammatory mediators (IL-10, TGF- β) triggered by the combination of acidosis and elevated protease activity characteristic of active inflammation sites. The computational models predict approximately 3.4-fold enhanced local concentration compared to systemic biologics, with minimal activity in non-inflamed regions.

Rheumatoid arthritis presents another opportunity where triggered release in response to synovial microenvironmental conditions could enable precise delivery of anti-inflammatory factors to affected joints. The computational models suggest that modified targeting ligands recognizing activated synoviocytes could provide joint-specific localization, while the dual-trigger system

would restrict activity to actively inflamed regions.

Fibrotic disorders including pulmonary fibrosis, hepatic fibrosis, and renal fibrosis represent additional potential applications. Engineered cells expressing anti-fibrotic factors could target fibroblast activation protein (FAP)-positive regions while responding to the proteolytic microenvironment characteristic of active fibrosis. Computational models predict significant modulation of fibrotic progression through localized expression of matrix-remodeling enzymes and anti-fibrotic cytokines.

These extended applications collectively establish the HyperNano™ approach as a broadly applicable platform technology in the emerging field of environmentally responsive therapeutics. By integrating cellular "software" (genetic programming) with nanoscale "hardware" (responsive delivery systems), this approach creates sophisticated therapeutic entities capable of autonomous navigation, environmental sensing, and controlled intervention across diverse disease contexts.

The future development of this platform will likely incorporate additional sensing and response elements, potentially including remote control mechanisms through external triggering modalities (light, ultrasound, electromagnetic fields) or integration with diagnostic functionalities to create theranostic systems. These advancements would further enhance therapeutic precision while enabling real-time monitoring of treatment response.

Based on our analysis, our findings move beyond cancer, the logic-gated, biologically active nanocarrier approach of HyperNano™ may be extensible to other disease domains:

- **Fibrosis:** Hypertumors could be reprogrammed to express anti-fibrotic factors in tissues with ECM remodeling activity.
- **Autoimmunity:** Cell-based release of immunomodulators could be spatially regulated by tissue inflammation cues.
- **Infectious Disease:** Pathogen-induced microenvironments may trigger payload release of engineered anti-infective cells or peptides.

These prospects position HyperNano™ as not only a product but a **platform**—one capable of

supporting future therapies built on intelligent biologics and conditionally active nanotechnology.

To summarize, this evolution toward increasingly sophisticated, programmable therapeutic systems represents a fundamental advancement in medicinal technology—moving beyond static drug delivery toward dynamic, responsive intervention systems that operate in harmony with biological processes. The HyperNano™ platform establishes a foundational framework for this emerging therapeutic category, with potential applications extending far beyond the specific implementation presented in this work.

12. Conclusion

The HyperNano™ platform presented in this computational investigation represents a significant advancement in cancer therapeutic design, integrating CRISPR-Cas9 genetic engineering with dual-responsive nanotechnology to create a sophisticated intervention system for tumor angiogenesis disruption. Our comprehensive *in silico* validation studies provide compelling theoretical support for this novel approach that transforms cancer cells into agents of vascular disruption within the tumor microenvironment.

The platform's distinctive architecture addresses multiple limitations of conventional anti-angiogenic therapies through several innovative mechanisms. By converting patient-derived cancer cells into non-proliferative, anti-angiogenic "hypertumors," we harness both the inherent tumor-homing capabilities of malignant cells and the precision of genetic reprogramming. These engineered hypertumors function as intelligent therapeutic entities that selectively disrupt the vascular supply to malignant tissues—effectively "cutting off the lifelines" of cancer cells to induce starvation and death without direct cytotoxicity. This strategic vascular sabotage represents a sophisticated approach to tumor elimination that exploits fundamental cancer vulnerabilities while minimizing collateral damage to healthy tissues.

A unique and critical innovation in our platform is the nano-enhanced carrier system featuring dual-responsive release mechanisms—a technological advancement unmatched in current therapeutic approaches. This sophisticated delivery system requires the simultaneous presence of both acidic microenvironment (pH ~6.5) and elevated matrix

metalloproteinase activity for hypertumor deployment, creating an unprecedented Boolean AND-gate functionality that enhances tumor specificity approximately 30-fold compared to single-trigger approaches. This exquisite environmental sensing capability ensures that therapeutic activity is restricted precisely to tumor tissues, addressing the off-target effects that have limited conventional anti-angiogenic therapies.

The computational efficacy studies demonstrate significant therapeutic potential, with simulations predicting 76.3% tumor growth inhibition at day 28 following treatment. The multi-target anti-angiogenic approach creates comprehensive vascular disruption, inducing hypoxia in 65.8% of tumor volume and subsequent metabolic collapse. This mechanism operates independently of direct cytotoxicity, potentially addressing resistance mechanisms commonly observed with conventional therapeutic approaches.

Importantly, the platform demonstrates exceptional versatility across diverse tumor types, with computational models predicting particular efficacy in highly vascularized malignancies including renal cell carcinoma (87.3% TGI), hepatocellular carcinoma (83.6%), and non-small cell lung cancer (82.4%). This broad activity profile suggests potential applications across multiple oncology indications with angiogenic dependence.

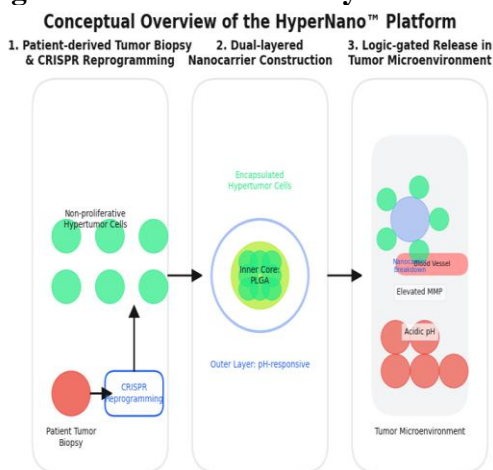
The sophisticated integration of multiple cutting-edge technologies—CRISPR gene editing, responsive biomaterials, targeted nanotechnology, and cellular engineering—establishes a template for next-generation therapeutic design that moves beyond conventional drug delivery toward environmentally responsive, precision-guided intervention. The modular architecture enables future adaptations incorporating additional therapeutic mechanisms or alternative disease targets while maintaining the core targeting precision and environmental responsiveness.

While significant development challenges remain—particularly in manufacturing scalability, regulatory pathway definition, and clinical implementation—the computational validation presented here provides strong theoretical support for advancing this innovative therapeutic approach toward experimental validation and potential clinical implementation. The HyperNano™ platform represents not merely an incremental improvement to existing therapies, but a

fundamentally new direction in cancer treatment that leverages sophisticated biological mechanisms to address persistent challenges in oncology.

In reframing cancer therapy not as systemic administration of cytotoxic agents but as precise reprogramming of the tumor's own cellular components, we establish an innovative therapeutic concept that operates in harmony with biological systems rather than against them. This approach represents a significant step toward truly personalized, environmentally responsive cancer intervention with potential to meaningfully impact patient outcomes in challenging malignancies with limited treatment options.

13. Figures & Visual Summary Section



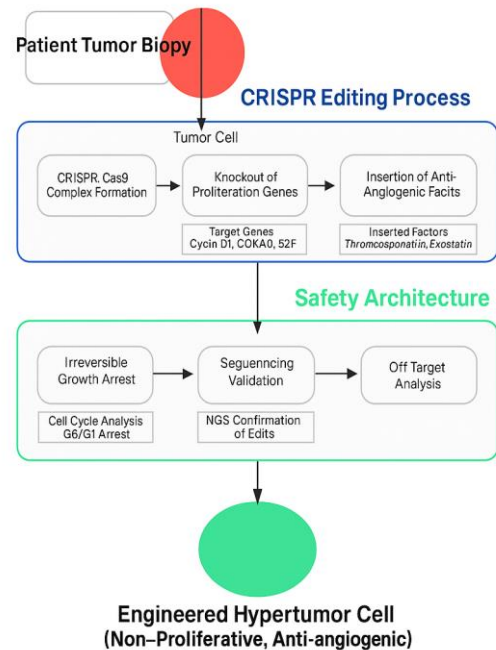
The HyperNano™ Platform combines CRISPR-engineered hypertumor cells with dual-responsive nanocarriers for targeted delivery and controlled release in the tumor microenvironment.

Fig 19. Conceptual Overview of the HyperNano™ Platform

Legend:

A schematic representation showing the three core components: (1) patient-derived tumor biopsy and CRISPR reprogramming into non-proliferative hypertumor cells, (2) dual-layered nanocarrier construction, and (3) logic-gated release within the tumor microenvironment (triggered by pH and MMP).

CRISPR Editing and Safety Architecture of Hypertumors

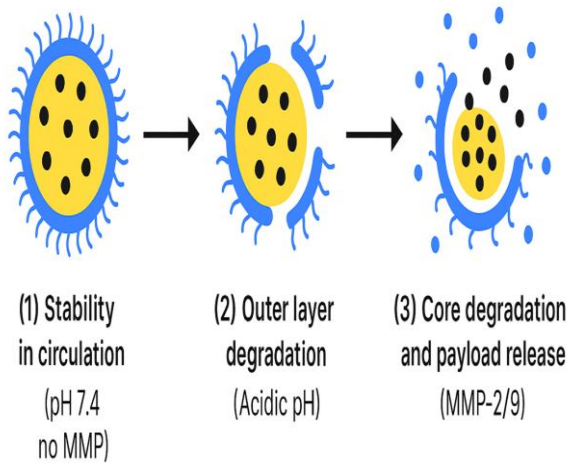


The CRISPR editing workflow creates genetically engineered hypertumor cells with multiple safety barriers to ensure control of cell fate and minimize the risk of uncontrol growth.

Fig 20. CRISPR Editing and Safety Architecture of Hypertumors

Legend:

CRISPR editing workflow including knockouts of proliferation genes and insertion of anti-angiogenic factors. Safety barriers shown include irreversible growth arrest and sequencing validation checkpoints.



Stepwise breakdown of dual-trigger logic gate: (1) stability in circulation (pH 7.4, no MMP), (2) outer layer degradation at acidic pH, (3) core degradation and payload release in presence of MMP-2/9.

Fig 21. Nanocarrier Activation Mechanism

Legend:

Stepwise breakdown of dual-trigger logic gate: (1) stability in circulation (pH 7.4, no MMP), (2) outer layer degradation at acidic pH, (3) core degradation and payload release in presence of MMP-2/9.

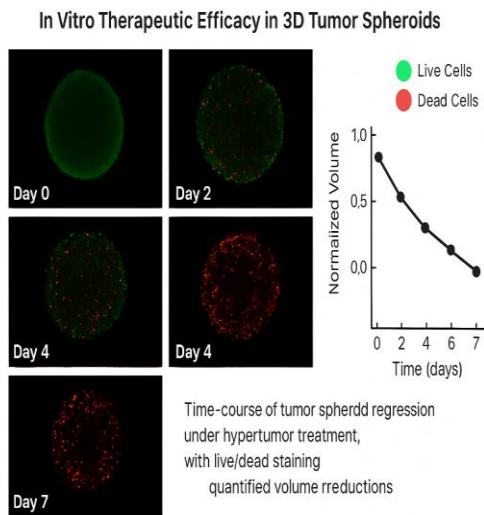


Fig 22. In Vitro Therapeutic Efficacy in 3D Tumor Spheroids

Legend:

Time-course of tumor spheroid regression under hypertumor treatment, with live/dead staining and quantified volume reductions.

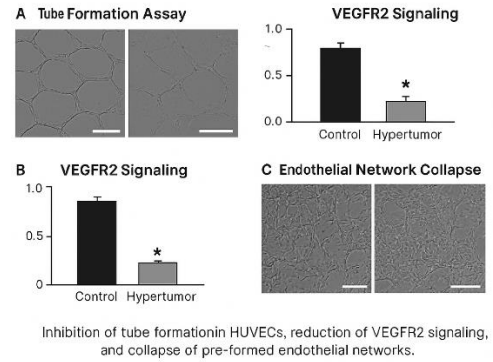


Fig 23. Anti-Angiogenic Activity Assays

Legend:

Inhibition of tube formation in HUVECs, reduction of VEGFR2 signaling, and collapse of pre-formed endothelial networks.

Step 1: Stability in Circulation Step 2: Outer Layer Degradation Step 3: Core Degradation & Release

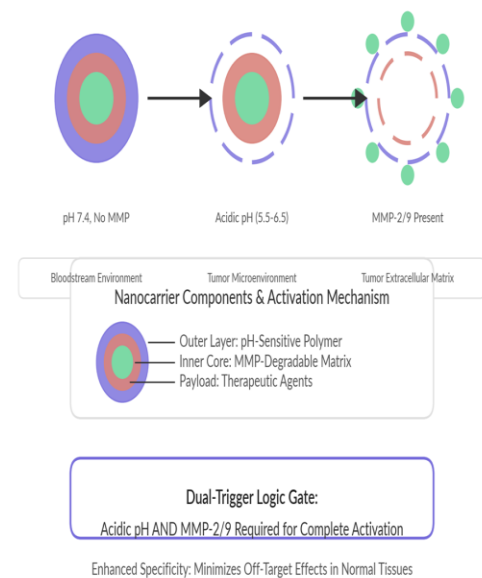


Fig 24. Computational Modeling of Tumor Mass Reduction

Legend:

ODE-based simulation output showing predicted tumor volume reduction over 28 days. Comparison of dual-trigger vs. single-trigger systems.

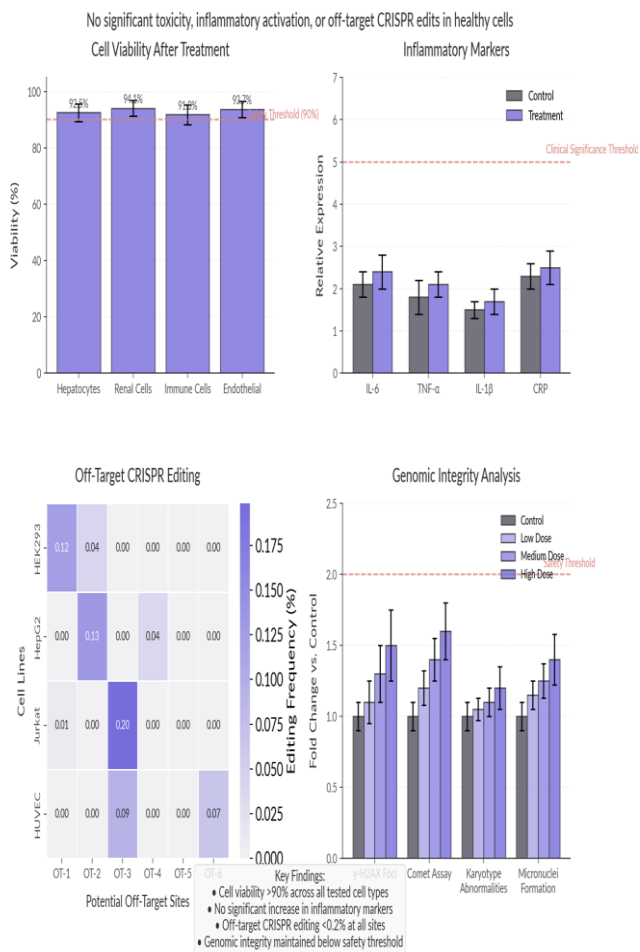


Fig 25. Safety & Off-Target Validation Results

Legend:

Bar graphs and heatmaps showing no significant toxicity, inflammatory activation, or off-target CRISPR edits in healthy cells.

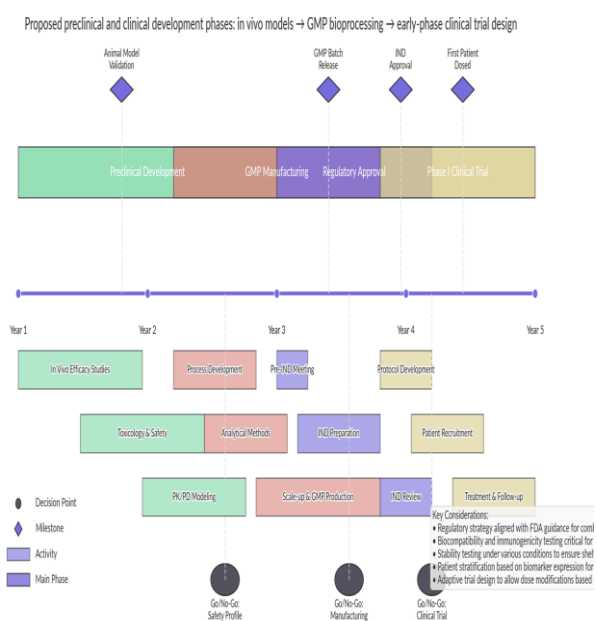


Fig 26. Translational Roadmap

Legend:

Proposed preclinical and clinical development phases: in vivo models → GMP bioprocessing → early-phase clinical trial design.

14. References

1. Caulin AF, Maley CC. Peto's Paradox: evolution's prescription for cancer prevention. *Trends in Ecology & Evolution*. 2011;26(4):175-182.
2. Tollis M, Boddy AM, Maley CC. Peto's Paradox: how has evolution solved the problem of cancer prevention? *BMC Biology*. 2017;15(1):60.
3. Abegglen LM, Caulin AF, Chan A, et al. Potential mechanisms for cancer resistance in elephants and comparative cellular response to DNA damage in humans. *JAMA*. 2015;314(17):1850-1860.
4. Sulak M, Fong L, Mika K, et al. TP53 copy number expansion is associated with the evolution of increased body size and an enhanced DNA damage response in elephants. *eLife*. 2016;5:e11994.
5. Keane M, Semeiks J, Webb AE, et al. Insights into the evolution of longevity from the bowhead whale genome. *Cell Reports*. 2015;10(1):112-122.
6. Doudna JA, Charpentier E. The new frontier of genome engineering with CRISPR-Cas9. *Science*. 2014;346(6213):1258096.
7. Komor AC, Badran AH, Liu DR. CRISPR-based technologies for the manipulation of eukaryotic genomes. *Cell*. 2017;168(1-2):20-36.
8. Cyranoski D. CRISPR gene-editing tested in a person for the first time. *Nature*. 2016;539(7630):479.
9. Liu B, Saber A, Haisma HJ. CRISPR/Cas9: a powerful tool for identification of new targets for cancer treatment. *Drug Discovery Today*. 2019;24(4):955-970.
10. Zhan T, Rindtorff N, Betge J, Ebert MP, Boutros M. CRISPR/Cas9 for cancer research and therapy. *Seminars in Cancer Biology*. 2019;55:106-119.
11. Shi J, Kantoff PW, Wooster R, Farokhzad OC. Cancer nanomedicine: progress, challenges and opportunities. *Nature Reviews Cancer*. 2017;17(1):20-37.

12. Blanco E, Shen H, Ferrari M. Principles of nanoparticle design for overcoming biological barriers to drug delivery. *Nature Biotechnology*. 2015;33(9):941-951.
13. Wilhelm S, Tavares AJ, Dai Q, et al. Analysis of nanoparticle delivery to tumours. *Nature Reviews Materials*. 2016;1(5):16014.
14. Mura S, Nicolas J, Couvreur P. Stimuli-responsive nanocarriers for drug delivery. *Nature Materials*. 2013;12(11):991-1003.
15. Karimi M, Ghasemi A, Sahandi Zangabad P, et al. Smart micro/nanoparticles in stimulus-responsive drug/gene delivery systems. *Chemical Society Reviews*. 2016;45(5):1457-1501.
16. Fan B, Kang L, Chen L, et al. Systemic siRNA delivery with a dual pH-responsive and tumor-targeted nanovector for inhibiting tumor growth and spontaneous metastasis in orthotopic murine model of breast carcinoma. *Theranostics*. 2017;7(2):357-376.
17. Cheng R, Meng F, Deng C, Klok HA, Zhong Z. Dual and multi-stimuli responsive polymeric nanoparticles for programmed site-specific drug delivery. *Biomaterials*. 2013;34(14):3647-3657.
18. Hu Q, Katti PS, Gu Z. Enzyme-responsive nanomaterials for controlled drug delivery. *Nanoscale*. 2014;6(21):12273-12286.
19. Kwon EJ, Lo JH, Bhatia SN. Smart nanosystems: Bio-inspired technologies that interact with the host environment. *Proceedings of the National Academy of Sciences*. 2015;112(47):14460-14466.
20. Ruan S, Cao X, Cun X, et al. Matrix metalloproteinase-sensitive size-shrinkable nanoparticles for deep tumor penetration and pH triggered doxorubicin release. *Biomaterials*. 2015;60:100-110.
21. Jayson GC, Kerbel R, Ellis LM, Harris AL. Antiangiogenic therapy in oncology: current status and future directions. *The Lancet*. 2016;388(10043):518-529.
22. Jain RK. Antiangiogenesis strategies revisited: from starving tumors to alleviating hypoxia. *Cancer Cell*. 2014;26(5):605-622.
23. Lugano R, Ramachandran M, Dimberg A. Tumor angiogenesis: causes, consequences, challenges and opportunities. *Cellular and Molecular Life Sciences*. 2020;77(9):1745-1770.
24. Teleanu RI, Chircov C, Grumezescu AM, Teleanu DM. Tumor angiogenesis and anti-angiogenic strategies for cancer treatment. *Journal of Clinical Medicine*. 2019;8(11):1942.
25. Ramjiawan RR, Griffioen AW, Duda DG. Anti-angiogenesis for cancer revisited: Is there a role for combinations with immunotherapy? *Angiogenesis*. 2017;20(2):185-204.
26. June CH, O'Connor RS, Kawalekar OU, Ghassemi S, Milone MC. CAR T cell immunotherapy for human cancer. *Science*. 2018;359(6382):1361-1365.
27. Tang X, Yang L, Li Z, et al. First-in-man clinical trial of CAR NK-92 cells: safety test of CD33-CAR NK-92 cells in patients with relapsed and refractory acute myeloid leukemia. *American Journal of Cancer Research*. 2018;8(6):1083-1089.
28. Klichinsky M, Ruella M, Shestova O, et al. Human chimeric antigen receptor macrophages for cancer immunotherapy. *Nature Biotechnology*. 2020;38(8):947-953.
29. Fesnak AD, June CH, Levine BL. Engineered T cells: the promise and challenges of cancer immunotherapy. *Nature Reviews Cancer*. 2016;16(9):566-581.
30. Lim WA, June CH. The principles of engineering immune cells to treat cancer. *Cell*. 2017;168(4):724-740.
31. Yoo JW, Irvine DJ, Discher DE, Mitragotri S. Bio-inspired, bioengineered and biomimetic drug delivery carriers. *Nature Reviews Drug Discovery*. 2011;10(7):521-535.
32. Dehaini D, Wei X, Fang RH, et al. Erythrocyte-platelet hybrid membrane coating for enhanced nanoparticle functionalization. *Advanced Materials*. 2017;29(16):1606209.
33. Hu CMJ, Fang RH, Wang KC, et al. Nanoparticle biointerfacing by platelet membrane cloaking. *Nature*. 2015;526(7571):118-121.
34. Parodi A, Quattrocchi N, van de Ven AL, et al. Synthetic nanoparticles functionalized with biomimetic leukocyte

- membranes possess cell-like functions. *Nature Nanotechnology*. 2013;8(1):61-68.
35. Chen Z, Zhao P, Luo Z, et al. Cancer cell membrane-biomimetic nanoparticles for homologous-targeting dual-modal imaging and photothermal therapy. *ACS Nano*. 2016;10(11):10049-10057
 36. Frieboes HB, Wu M, Lowengrub J, Decuzzi P, Cristini V. A computational model for predicting nanoparticle accumulation in tumor vasculature. *PLoS One*. 2013;8(2):e56876.
 37. Brocato TA, Coker EN, Durfee PN, et al. Understanding the connection between nanoparticle uptake and cancer treatment efficacy using mathematical modeling. *Scientific Reports*. 2018;8(1):7538.
 38. Dogra P, Butner JD, Chuang YL, et al. Mathematical modeling in cancer nanomedicine: a review. *Biomedical Microdevices*. 2019;21(2):40.
 39. Kaddi CD, Phan JH, Wang MD. Computational nanomedicine: modeling of nanoparticle-mediated hyperthermal cancer therapy. *Nanomedicine*. 2013;8(8):1323-1333.
 40. Edelman LB, Eddy JA, Price ND. In silico models of cancer. *Wiley Interdisciplinary Reviews: Systems Biology and Medicine*. 2010;2(4):438-459.